

TiO₂-based ceramics, from basic science to applications

Présentée le 10 septembre 2020

à la Faculté des sciences de base
Laboratoire de physique de la matière complexe
Programme doctoral en physique

pour l'obtention du grade de Docteur ès Sciences

par

Lidia ROSSI

Acceptée sur proposition du jury

Prof. P. Ricci, président du jury
Prof. L. Forró, E. Horvath, directeurs de thèse
Prof. V. Srdić, rapporteur
Dr L. Boilet, rapporteur
Prof. D. Damjanovic, rapporteur

*To my family,
my husband, Geoffroy
and my daughter Elena*

“La couleur est par excellence la partie de l’art qui détient le don magique”

Eugène Delacroix

Abstract

Nanomaterials and nanoparticles are nowadays used in a wide range of applications; from sunscreens, paint and food industry to catalytic processes, lighting, TV's and displays, their presence is percolating in our daily life. New applications rise every day, pushing forward the technology limits with increasing efforts and funding for nanomaterial science and applications. Among different nanomaterials, titanium dioxide (TiO_2) continues to attract considerable theoretical and experimental attention because of its technological relevance in applications such as environmental purification, solar energy harvesting, memristors, catalysis, advanced ceramic materials and more. Different allotropes and morphologies of the compound are being examined, in particular nanoparticles and nanofilaments (nanowires and nanotubes) in titanate ($\text{H}_2\text{Ti}_3\text{O}_7$), anatase or rutile phase.

In this dissertation, we have deeply investigated the behavior of titanium-oxide based nanowires (TiO_2 NWs), which, thanks to their larger specific surface area than bulk or polycrystalline counterparts, are very promising for photocatalysis. The TiO_2 NWs are very suitable for such nanofilamentary applications since they have an ideal form for assembling themselves into nanoporous aerogel membranes. Our nanowires can be used directly in both 2D and 3D architecture, and they can serve as ideal support (reducing Ostwald ripening and coarsening in general) for various metal nanoparticles.

$\text{H}_2\text{Ti}_3\text{O}_7$ NWs are equally important, indeed, both as active components, for example in case of very sensitive humidity sensors and efficient catalysts and as reinforcement fibers in composites or as metal nanoparticles support for advanced CO oxidation catalysis.

The NW behavior in titanate, anatase and rutile phase has been studied and the phase transition temperature determined, finding out that the strong surface effects, in the 2D system, result in unexpected stabilization of the metastable anatase phase and the absence of rutile phase above 900 °C. However, the classical Ostwald ripening particle coarsening is observed in sintered pellets, accompanied by a typical anatase to rutile phase transition at 900 °C.

Mechanical measurements and nanoscopic observations both on bulk and on individual nanowire have allowed determining the mechanical moduli and the hardness. In particular, for the first time, the shear modulus of individual nanowire in titanate phase has been directly measured and its relatively low value of 1.5 ± 0.8 GPa confirms the layered structure with a relatively weak bond between layers. The elastic modulus is within the expected range of about 70 GPa for titanate and above 100 GPa for anatase. Another discovery is that 3D pellets of sintered anatase nanowires show considerably higher microhardness values when compared to sintered bodies composed of

nearly spherical nanoparticles, with microhardness measurements of about 940 HV after 900 °C sintering (1.6% porosity).

As previously mentioned, our titania nanowire 2D systems, have shown superior characteristics as support for gold nanoparticles. Particles sizes as small as 3-5 nm can be preserved for gold, even after 400 °C treatment in air and after 800 °C in a hydrogen atmosphere, probably thanks to a very effective edge stabilization and Ti^{3+} defects enhanced electronic strong metal support interaction effect. This opens the way for possible use for environmental and sustainable energy catalytical applications. The interaction of gold nanoparticles with our TiO_2 nanowires in bulk form was also addressed, specifically driven by applications in watch industry or jewellery, with interesting results. Composites pellets of various carats have been sintered during this work and thoroughly investigated: the possibility to widely tune the color (due to a strong plasmonic effect), as well as the very good mechanical properties, of our gold/titania pellets was demonstrated.

Functionality and potential impact of TiO_2 NWs for a few specific catalytical applications have been explored. The photocatalytic effectiveness of titania nanowires for destroying DNA chains after a suitable exposition to UV light (elimination of pollutants) was established. Also photocatalytical effectiveness of TiO_2 pellets with gold nanoparticles for degrading methyl orange was proved. It turned out that 18-carat pellets (i.e 75wt% Au) are not only very effective but also easy to regenerate, with a positive impact on cost and environment. These novel cermet formulations are ideal candidates for a novel, easily sterilisable medical devices but even jewelry and watches. Development of this kind of easily sterilisable future products may be desirable after the recent Covid-19 coronavirus outbreak.

Finally, I investigated the application of our TiO_2 NWs in the form of paper filters for viruses and bacteria, like the current SARS-CoV-2. I demonstrated the concept of novel personal protective equipment (PPE), that TiO_2 NWs based-facial mask is may be very effective stopping the virus or bacteria, but also that it is easily regenerated with simple UV exposition, cutting down the economical and environmental cost of a future product.

More work is necessary to assess the technical and economical sustainability in operative conditions for each of the above-mentioned applications. However, I am very glad say that my thesis work serves as a basis to exploit the industrial potential of elongated titanates. Based on the breakthrough application of our TiO_2 NWs tech-transfer efforts are being envisaged right now for producing effective, low cost, recyclable and environmentally sustainable filtering masks for the present Covid-19 needs and, in perspective, for many other medical uses.

Keywords

Titanate, nanowires, sintering, ceramic oxide, Ostwald ripening, particle coarsening, gold nanoparticles, hardness, shear modulus, elastic modulus, photocatalysis, Covid-19.

Résumé

Les nanomatériaux et les nanoparticules sont aujourd'hui utilisés dans un large éventail d'applications; dans les crèmes solaires, dans la peinture, dans l'industrie alimentaire jusqu'aux procédés catalytiques, en passant par l'éclairage, les téléviseurs et les écrans, leur présence s'infiltré dans notre vie quotidienne. De nouvelles applications apparaissent chaque jour, repoussant les limites de la technologie grâce aux efforts et aux financements croissants en faveur de la science des nanomatériaux et ses applications. Parmi les différents types de nanomatériaux, le dioxyde de titane (TiO_2) continue à prendre une place considérable dans les études théoriques comme dans le domaine expérimental, en raison de son importance technologique pour les applications telles que la purification de l'environnement, la collecte de l'énergie solaire, les mémoires, la catalyse, les matériaux céramiques avancés. Différentes allotropes et morphologies du composé sont examinées, en particulier les nanoparticules et les nanofilaments (nanofils et nanotubes) en phase titanate ($\text{H}_2\text{Ti}_3\text{O}_7$), anatase ou rutile.

Dans cette thèse, nous avons étudié en profondeur le comportement des nanofils à base d'oxyde de titane, qui, grâce à leur plus grande surface spécifique que leurs homologues massifs ou polycristallins, sont très prometteurs pour la photocatalyse. Les nanofils de TiO_2 sont très adaptés à ces applications nanofilamentaires car ils ont une forme idéale pour s'assembler en membranes d'aérogel nanoporeuses. Nos nanofils peuvent être utilisés directement dans une architecture 2D et 3D et ils peuvent servir de support idéal (réduisant le mûrissement d'Ostwald et le grossissement en général) pour d'autres nanoparticules métalliques.

Les nanofils de titanate sont tout aussi importants, en effet, à la fois comme composants actifs, par exemple dans le cas de capteurs d'humidité très sensibles et de catalyseurs efficaces, et comme fibres pour le renforcement dans les composites ou comme support de nanoparticules métalliques pour la catalyse d'oxydation avancée du CO.

Le comportement des nanofils dans la phase titanate, anatase et rutile a été étudié et la température de transition de phase a été déterminée. On a découvert des effets de surface importants, dans le système 2D, entraînent une stabilisation surprenante de la phase anatase métastable et l'absence de phase rutile même au-dessus de 900 °C. D'autre part, le grossissement classique des particules du au mûrissement Ostwald est observé dans le cas de poudre frittée et il est accompagné d'une transition typique de la phase anatase à la phase rutile à 900 °C.

Des mesures mécaniques et des observations nanoscopiques, tant sur échantillons massifs que sur des nanofils individuels, ont permis de déterminer les modules mécaniques et la dureté. En particu-

lier et pour la première fois, le module de cisaillement de nanofil individuel en phase titanate a été directement mesuré et sa valeur relativement faible de $1.5 \pm 0,8$ GPa a confirmé la structure en couches de nos nanofils avec une liaison relativement faible entre les différentes couches. Le module d'élasticité se situe dans la plage attendue d'environ 70 GPa pour le titanate et de plus de 100 GPa pour l'anatase. Un autre résultat est que les pastilles 3D de nanofils d'anatase frittées présentent des valeurs de microdureté nettement plus élevées que les pastilles frittées composées de nanoparticules presque sphériques, avec des mesures de microdureté aussi haute que 940 HV après frittage à 900 °C (avec une porosité de 1,6 %).

Comme mentionné précédemment, notre système 2D de nanofils de titane a montré des caractéristiques supérieures en tant que support pour les nanoparticules d'or : des tailles aussi petites tel que 3-5 nm peuvent être préservées pour l'or, même après un traitement à 400 °C dans l'air et 800 °C dans une atmosphère d'hydrogène, probablement grâce à une stabilisation des bords très efficace et aux défauts liés aux Ti^{3+} qui améliorent l'effet d'interaction forte entre le métal et le support dû aux électrons. Cela ouvre la voie à une utilisation possible pour des applications catalytiques environnementales et énergétiques durables. L'interaction des nanoparticules d'or avec nos nanofils de TiO_2 en forme de pastilles 3D a également été étudiée, en particulier pour des applications dans l'industrie horlogère ou la joaillerie, avec des résultats très intéressants. Des pastilles composites de différents carats ont été frittées au cours de ce travail et ont fait l'objet d'une étude approfondie : la possibilité d'accorder les couleurs dans un spectre très large (grâce à un effet plasmonique très marqué), ainsi que les très bonnes propriétés mécaniques, de nos pastilles d'or/titane ont été démontrées.

La fonctionnalité et l'impact potentiel de nos nanofils de TiO_2 pour quelques spécifiques applications catalytiques ont enfin été explorés. L'efficacité de nos nanofils de titane pour la destruction des chaînes d'ADN après une exposition appropriée aux UV (pour l'élimination des polluants biologiques) a été établie. L'efficacité catalytique des pastilles de TiO_2 avec des nanoparticules d'or pour la dégradation du méthyl orange a également été prouvée : les pastilles de 18 carats (soit 75 % en poids d'or) sont non seulement très efficaces mais aussi faciles à régénérer, ce qui a un impact positif sur le coût et l'environnement.

Enfin, j'ai étudié l'application de nos nanofils de TiO_2 sous forme de filtres en papier pour combattre les bactéries et les virus, comme l'actuel SARS-CoV-2. J'ai démontré non seulement que le masque facial à base de nanofils de TiO_2 est très efficace pour arrêter le virus ou la bactérie, mais aussi qu'il est facilement régénérable par une simple exposition aux UV, ce qui réduit le coût économique et environnemental d'un dispositif basé sur ce matériau.

Des travaux supplémentaires sont nécessaires pour évaluer la viabilité technique et économique dans des conditions opérationnelles pour chacune des applications susmentionnées. Cependant, je suis très heureuse de conclure mon travail de thèse en annonçant qu'une percée pour l'application de nos nanofils de TiO_2 se profile : sous forme de tissu ou papier ils seront la base pour produire des masques filtrants efficaces, peu coûteux, recyclables et écologiquement durables pour les besoins actuels de Covid-19 et, en perspective, pour de nombreuses autres utilisations médicales.

Mots-clés

Titanate, nanofils, frittage, céramique à base d'oxide, murissement Ostwald, grossissement des particules, nanoparticules d'or, dureté, module de cisaillement, module élastique, photocatalyse, Covid-19.

Contents

Abstract	vii
Keywords	viii
Résumé	ix
Mots-clés.....	xi
List of acronyms	xvi
Introduction	17
Chapter 1 Experimental procedures	21
1.1 Characterizations.....	21
1.1.1 Atomic force microscope.....	21
1.1.2 Electron microscopy.....	25
1.1.3 X-ray diffraction.....	30
1.2 Sintering procedures and tooling.....	32
1.2.1 Hot Uniaxial Pressing.....	33
1.2.2 Spark Plasma Sintering.....	33
Chapter 2 Structure characteristics of titanate nanowires	35
2.1 Introduction	35
2.2 Crystal properties of titanium dioxide	36
2.2.1 A brief history, applications and economical importance of TiO ₂	36
2.2.2 Titanium dioxide structure and properties	39
2.2.3 Titanate nanowires.....	41
2.2.4 Oxygen vacancies role in TiO ₂	43
2.3 Thermal coarsening of individual and assemblies H ₂ Ti ₃ O ₇ nanowires	45
2.3.1 Experimental.....	45

2.3.2 Results and discussion	46
2.4 Conclusion.....	53
Chapter 3 Mechanical response of individual layered titanate nanowires	55
3.1 Motivations	55
3.2 Overview of experimental results on nanowires.....	56
3.2.1 Mechanical resonance excitation inside a TEM	56
3.2.2 Lateral deflexion by AFM	57
3.2.3 Normal deflexion by AFM.....	58
3.2.4 Literature survey on nanofilaments Young's modulus.....	60
3.3 Mechanical properties of titanate nanowires	61
3.3.1 Description of the method.....	61
3.3.2 Results: shear and Young's moduli of titanate.....	65
3.3.3 Transformation of titanate into anatase	68
3.4 Mechanical properties of titanate nanowires of $H_{2-x}Cu_xTi_3O_7$	69
3.4.1 Ion-exchange process	69
3.4.2 Results.....	71
3.5 Conclusions.....	71
Chapter 4 Metal nanoparticles interaction with TiO_2 nanowires	73
4.1 Introduction	73
4.2 Supported metal nanoparticles as catalyst	74
4.3 Sintering process.....	76
4.3.1 Forces inducing the sintering mechanism.....	77
4.3.2 Ostwald ripening vs. migration coalescence	78
4.4 Strategies for the fabrication of a sinter-resistant metal-NPs-based catalysts	79
4.5 Titania as Au NP support.....	81
4.6 Investigation on 2D systems	81
4.6.1 Experimental methods	81
4.6.2 Heat treatment in air	81
4.6.3 Heat treatment in hydrogen atmosphere.....	84
4.6.4 Stabilization mechanism	85

4.7	Investigation of 3D pellets.....	88
4.7.1	Plasmonic effect and color tuning	88
4.7.2	Experimental.....	90
4.7.3	18-carats	93
4.7.4	12-carat	97
4.7.5	1-carat	99
4.7.6	Electrical resistivity as a function of carats.....	101
4.8	Conclusions	102
Chapter 5	Photocatalysis applications	103
5.1	Photocatalysis.....	103
5.2	DNA decomposition	104
5.2.1	Experiment preparation for DNA decomposition.....	104
5.2.2	Results.....	105
5.2.3	Conclusion	107
5.3	Reusable protective masks.....	107
5.4	Photocatalytic activity on 3D composites pellets.....	109
5.4.1	Experiment preparation	109
5.4.2	Results.....	110
5.4.3	Conclusion	112
	Conclusions and outlook	113
	Appendix A.....	117
	Archimede's method	117
	Acknowledgements	119
	Bibliography	121
	Curriculum Vitae	137

List of acronyms

RT Room temperature (20 °C)

Characterization techniques

SEM Scanning electron microscope
TEM Transmission electron microscope
STEM Scanning transmission electron microscope
FIB Focused ion beam
XRD X-ray diffraction
EDX Energy-dispersive X-ray spectroscopy
AFM Atomic force microscope
TGA Thermal gravimetric analysis
EPR Electron paramagnetic resonance

Material

NW Nanowire
NP Nanoparticle

Sintering techniques

SPS Spark plasma sintering
IP Isostatic pressing
HUP Hot uniaxial pressing

Introduction

First, the title of my dissertation “TiO₂-based ceramics, from basic science to applications” sounds a bit too specialized and needs some explanation. The central material is titanium dioxide, a very abundant and very popular material in applications. It is present in sunscreens, (this is what absorbs the UV light and protects our skin), and in paints it is responsible for the white color, it is used in some types of solar cells, and it is also considered in a new generation of memory devices, the so-called memristors. In my doctoral study I was interested more in another aspect of this material, that with a very smart chemical approach, one can make filaments, out of the TiO₂ ceramic, which have a diameter in the nanometer scale.

One can ask the question, why to make nanowires of TiO₂? Because by changing the quantity, and the size, a material can attain different properties. There is a famous phrase of P.W. Anderson (Nobel laureate in physics), that “More is different”. This was meant to summarize that the electronic properties of a material are different with lot of electrons than with a fewer ones. One can paraphrase this sentence with “Less is different” which is exactly our case. The same material behaves differently at nanoscales than in macroscopic size. For example, the mechanical property is very much different. In Figure 1 is shown a crystal of TiO₂ and its nanowire form. The crystal is very brittle, it breaks easily if one tries to bend it, while the nanowire is highly elastic, it can follow the form of a hole cut out in a plate.

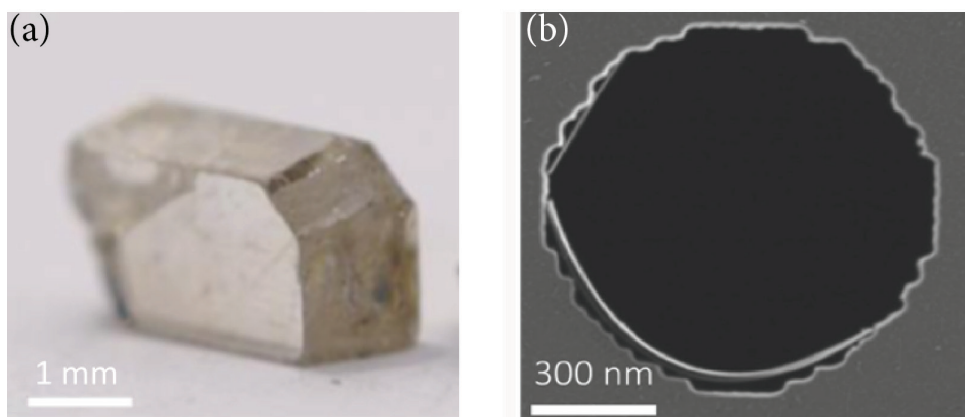


Figure 1 a) Photo of a macroscopic crystal of the anatase phase of TiO₂; b) Scanning Electron Microscopy image of a nanowire of the same material, showing its highly elastic behavior as it follows the arc made in Si₃N₄ material.

The fact that the surface to volume ratio of a nanowire is much bigger gives a special advantage to it in respect to the big crystals. The material possesses a further attractive property, namely that ultra-violet illumination generates free electrons inside the structure, which by diffusion to the surface, can create free radicals, chemically very active molecules in the surrounding water, which could kill bacteria and viruses, or disintegrate other organic species. The investigation of all these properties at nanometer dimensions still fall in the domain of the range of basic science: and only once these properties are better understood, we can use this material very efficiently in applications.

Speaking about applications, one needs to push further the paraphrasing of Anderson's idiom: "More of less makes a big difference". It means that synthesizing lot of these nanostructures is important for applications, because if one can make only milligrams quantities of them, then it falls into the category of "non-applicable applications". In my dissertation, I demonstrate a good counter-example of it. Thanks to an outstanding chemist in our laboratory, who could scale up the synthesis of these nanowires to kilograms, one could think of real applications. In Figure 2 a photo is shown with a bucket full of nanowires and next to it a filter paper made of it, which could be used in water purification, personal masks or air conditioners as a very efficient antiviral, antibacterial structure that if illuminated with UV light can be easily regenerated, with clear cost and environmental advantage. It is very relevant in our times, and can realistically make a positive impact on people's lives.

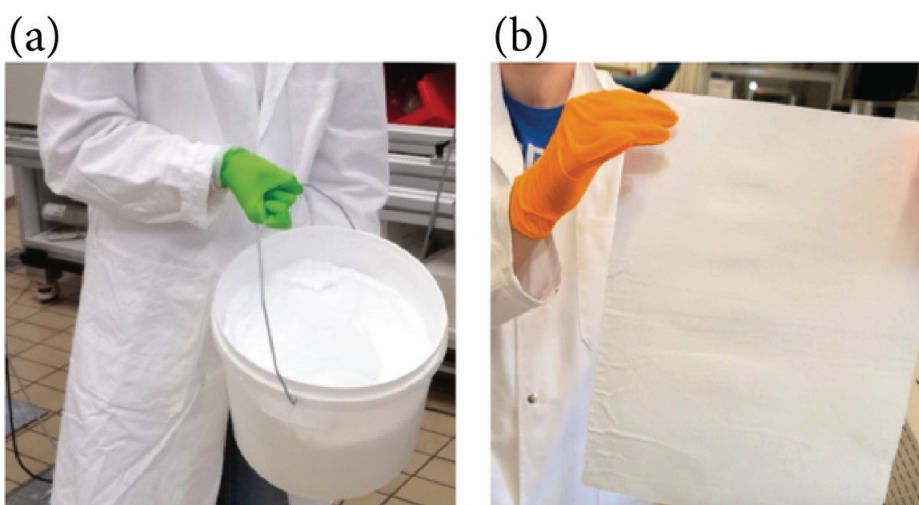


Figure 2 a) Showing a kilogram-scale production of TiO_2 nanowires with a bucket full of these structures; b) an antibacterial/antiviral filter paper processed from these nanowires.

These nanostructures offer also the possibility to invent new materials and shapes, like in pottery with clay (actually this is the meaning of "ceramics" in Greek) creating new wonderful objects. This falls more in the range of esthetics and it needs, beyond the TiO_2 , also metallic nanoparticles, like gold, silver or else. These small particles change the color of the object thanks to an effect which is called "plasmonic resonance". This term sounds very much technical, what does it mean? With the visible white light (resulting from the mixture of all the colors), one can shake the electrons on the

small metallic particles. This shaking needs a well-defined energy, depending on the size (and shape) of the particles, which is absorbed. From the reflected or transmitted light this energy (color) will be missing, and the object will shine with the complementary color. In practice this means that changing the size of the metallic particles, one can tune the color of the objects.

One of the known examples of the use of this phenomenon in the history is the famous Lycurgus cup, a roman masterpiece dating from IV century A.D. Without knowing the physical background, just by experience, they managed to tune the color of the cup. The dichroic glass of this cup is embedded with gold and silver nanoparticles; thanks to the plasmonic resonance the cup appears red in transmission and green in reflection, see Figure 3.

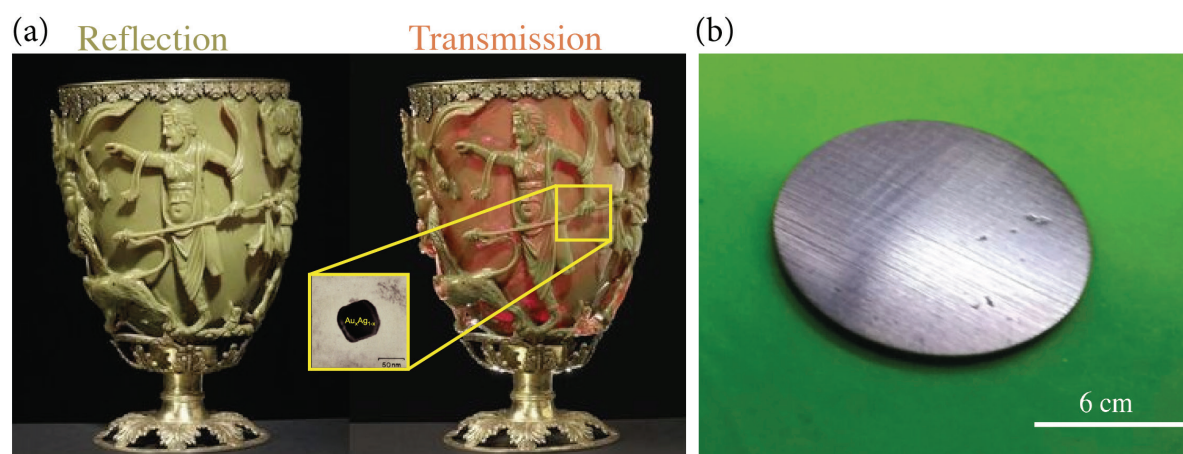


Figure 3 a) The famous Lycurgus cup, roman glassmaking, British Museum, dated from the fourth century A.D., is made of glass with gold and silver alloy nanoparticles of about 70 nm. The presence of $\text{Au}_x\text{Ag}_{1-x}$ nanoparticles (where $x \sim 0.3$), has been confirmed by X-ray diffraction, see at the right. It results in green color in reflectivity and red color in transmission. Figure is taken from Ref. (1); b) a disc of 18-carat gold TiO_2 ceramic of a greenish hue.

The very same effect I was also exploring during these 4 years of the doctoral studies. Precipitating gold nanoparticles onto a large assembly of TiO_2 nanowires, and after compacting it and heating, called by sintering, I could make 18-carat gold which has a greenish hue, dramatically different from the yellow gold (see Figure 3b). As far as I know, this is the first fabrication of such a composite material from nanostructured ceramics. We see an immediate application of it in jewelry industry but other branches, when a special substrate is needed could be highly interested by this composite.

Outline

Based on these topics exposed above for a broad audience, my dissertation is structured as follows:

Following this section, introducing the work and the dissertation outline, in the **first chapter**, I will introduce experimental procedures, and the instruments that have been the most critical for our investigation. Then I will focus on the sintering techniques and tooling used in this study.

In **chapter two**, after a review of the literature about titanium dioxide, I focus on titanates nanowires properties, and in particular, I expose the investigation of thermal coarsening of $\text{H}_2\text{Ti}_3\text{O}_7$ NWs as a function of the temperature from room temperature up to 1000 °C. Phase transformation kinetics and the external morphology are studied in two configurations: i) as individual and suspended titanate NWs on SiO_2 surface and ii) as large assembly, or bulk, in form of sintered pellets.

Our knowledge about TiO_2 NWs mechanical properties is still very sparse and very often theory and experiments do not match; this subject is the content of **chapter three**. I report a detailed study of the mechanical response of titanate nanowires to external stress/strain: their elastic and shear moduli, their flexibility, fatigue behavior and the rupture force have been all measured. We have also characterized the change of Young's modulus due to the thermal transformation of titanate into anatase NWs.

In **chapter four**, we investigate the behavior of our NWs when used as support of metal nanoparticles. We studied in particular gold nanoparticles, laying on single titanate NWs (2D systems) as a function of heat treatment conditions. Different diffusion mechanisms like coalescence-migration and Ostwald ripening effect occur, depending on the temperature treatment and experimental conditions. We investigate also 3D systems, i.e. pellets made of titania/gold nanoparticles under sintering. Besides discussing the mechanical and electrical properties as a function of the gold content (carats), we have characterized also the color changes (due to plasmonic effect), a very important issue for jewelry and watch applications.

Three applications of titania NWs, all related to their use as photocatalyst, are illustrated in **chapter five**, assessing their functionality, efficiency, and potential impact of our TiO_2 NWs, including a very timely use for anti-virus filter for facial masks.

In the last section, we report the conclusions, with a general analysis and discussion of the results.

At the end, I have to say, that I immensely enjoyed these for years. They have shown me what is an exciting scientific research about. It is never just physics, it is never just chemistry, but it has lot of material science, lot of engineering, dealing sometimes with living matter, and always with the goal of making something useful.

Chapter 1 Experimental procedures

In this section I will present an overview of main characterizations techniques for samples studied in this work.

1.1 Characterizations

1.1.1 Atomic force microscope

In 1986 Gerd Binnig and Heinrich Rohrer received the Nobel Prize in Physics (2) in recognition of their contribution to the development of a new microscopic technique based on the so-called "Tunnel effect" (3), a technique that would later inspire atomic force microscopy (AFM).

In its most generic form, an AFM is composed of (Figure 1:1):

- A **piezoelectric-scanner** allowing movements with sub-nanometric precision and providing the measurement of the force exerted by the cantilever tip onto the sample;
- A **tip** located at the end of a flexible and reflective cantilever;
- A **laser** and a **four-quadrant photodetector** sensible to the laser position;
- Electronic system for acquisition.

The laser beam is sent to the cantilever and reflected on the photodetector. Interactions between the tip and the sample twist the elastic cantilever, changing the position of the laser on the detector. The sample is placed on the piezoelectric column, which allows the sample to be moved in all 3 directions of space with subnanometric precision and to scan the sample under the tip.

Depending on the distance between the sample and the tip, the tip will be subjected to different forces. At large distances (of the order of mm), the interactions will be negligible. Then when the tip starts to interact with the surface of the sample, attractive forces tip-sample known as van der Waals forces appear, while for relatively smaller distances Coulomb interactions, called ionic repulsion interaction dominates.

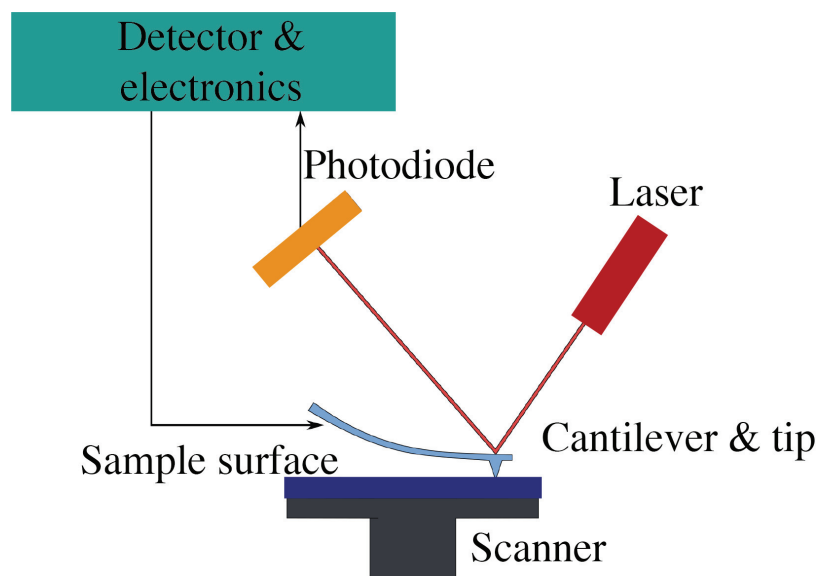


Figure 1:1 Schematic representation of an AFM. A sample is mounted on a piezo-electric scanner providing position and force measurement. A tip positioned at the end of the cantilever interacts with the sample surface and their interaction distorts the cantilever and the signal is reflected by the incoming laser onto a photodiode and the electronic information provides the sample topography.

AFM operates in different configurations depending on the required applications.

Contact mode: the tip is in contact with the sample. Between the tip and the surface of the sample, various forces act and produces the deflection of the cantilever following Hooke's law. In contact mode, AFM can take images in two ways: constant-height or constant-force. In constant-force mode (operating mode in this study) the scanner moves up and down in z-axis direction, according to topological changes, to keep constant, the interaction force between the tip-sample. Typical forces usually are in the order of 10 nN - 10 pN. The sample topography is obtained by conversion of the voltage signal needed to elongate or contract the piezo-scanner into the topography.

Intermittent contact (tapping) mode: the cantilever is oscillating close to the surface of the sample, the van der Waals forces modify the amplitude of the oscillation. This modification is used as a surface measurement, from which the profile of the sample is obtained at the point, where the cantilever is located.

Non-contact mode: the tip does not touch the sample and oscillates near the surface. The tip-sample distance is controlled by changing the frequency and the oscillating amplitude (4)-(6). Forces involved in this mode are in general on the order of 10 pN. Furthermore, this mode requires to use stiffer cantilevers in order to avoid snap-in, when the AFM tip is randomly attracted by surface adhesion forces so much that the tip is getting in contact with the surface.

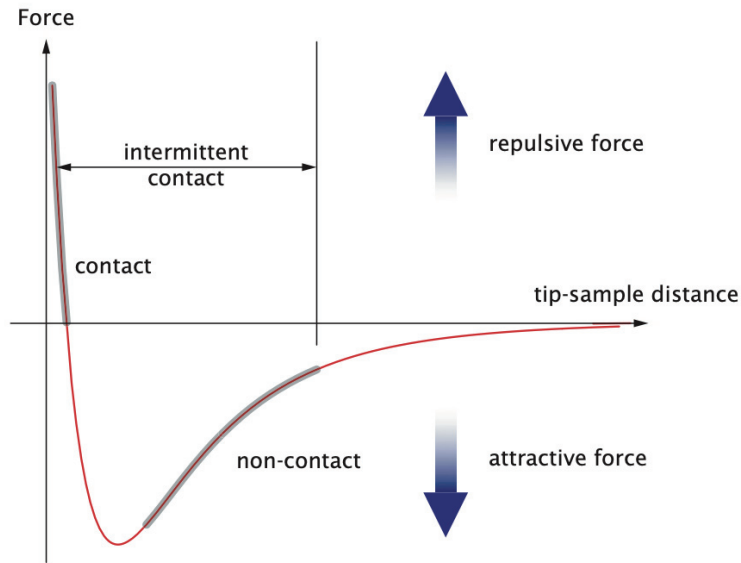


Figure 1:2 Interatomic potential as a function of tip-sample distance. Fig. taken from Ref. (7).

1.1.1.1 Force measurement curve

In this dissertation, AFM data collected in force measurement mode is used for studying mechanical properties of titanate nanowires.

The force curve is a curve that describes the force exerted on the cantilever tip, as it approaches and moves away from the sample surface, as a function of the cantilever tip displacement along the vertical axis. Examining a force curve, see Figure 1:3, we can see that it is divided into two parts: a curve that describes the approach, and one that describes the moving away from the surface. Initially, when the AFM tip is far away from the sample/surface to be examined, it can be seen that the deflection of the cantilever is constant and therefore, it is assumed as a zero-deflection point. When approaching the sample, the tip of the probe will be suddenly attracted to the sample (snap-in), due to the attractive van der Waals. Continuing the approach, the deflection changes sign, the probe comes into contact with the surface and is rejected by the sample. At this point the cantilever retracts and one would expect the force curve to "retrace" following the same path as the forward path. However, a slightly higher negative force is measured in the retracting path, due to the adhesion forces that hold the tip of the probe to the sample for a short moment of time. These adhesion forces are created by the water molecules present on the surface since AFM measurements take place under common environmental conditions. This difference in path between the trace and retrace in the force curves causes a hysteresis, and, in addition to the atmospheric conditions of the environment in which it is carried out, the measured curve also depends on the characteristics of the probe itself and its tip (8).

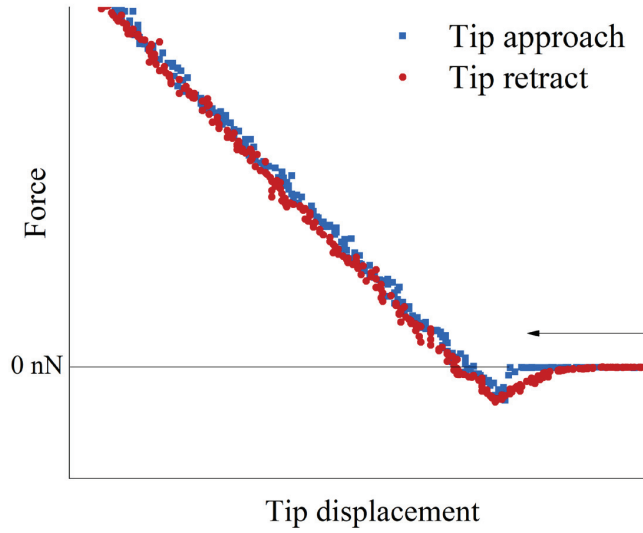


Figure 1:3 Typical force curve when the tip is approaching the sample (in red) and when the tip is retracting from the sample (in blue). Negative force value means an attractive force between tip and sample.

1.1.1.2 AFM probe and calibration

To provide accurate nanomechanical property measurements, both, cantilever spring constant and deflection sensitivity is required. Conventional spring constant calibration techniques rely on multiple cantilever probe tips in contact with the surface with the consequences of damaging the tip. Therefore, we preferred to use commercially available cantilevers, laser Doppler vibrometry (LDV) calibrated, RTESPA-300-30 from Bruker. We have chosen a cantilever type with a high nominal 40 N/m spring constant and 30 nm tip end radius, specifically calibrated for our experiments. The results shown in Section 3.3 were obtained with a 47.038 N/m spring constant and 30.1 nm tip end radius cantilever. An SEM image of the tip used for the measurements is shown in Figure 1:4.

The AFM (XE-100 PSIA) makes use of a 2-dimensional flexure stage to scan the sample in the XY direction, and a stacked piezoelectric actuator to scan the probe in the Z direction. In this way, the accurate position of the probe was ensured, while eliminating the crosstalk issues commonly faced in such measurements. The deflection sensitivity is determined from a force *versus* piezo extension curve on a stiff substrate in the linear region of both stacked piezoelectric actuator and deflection detector.

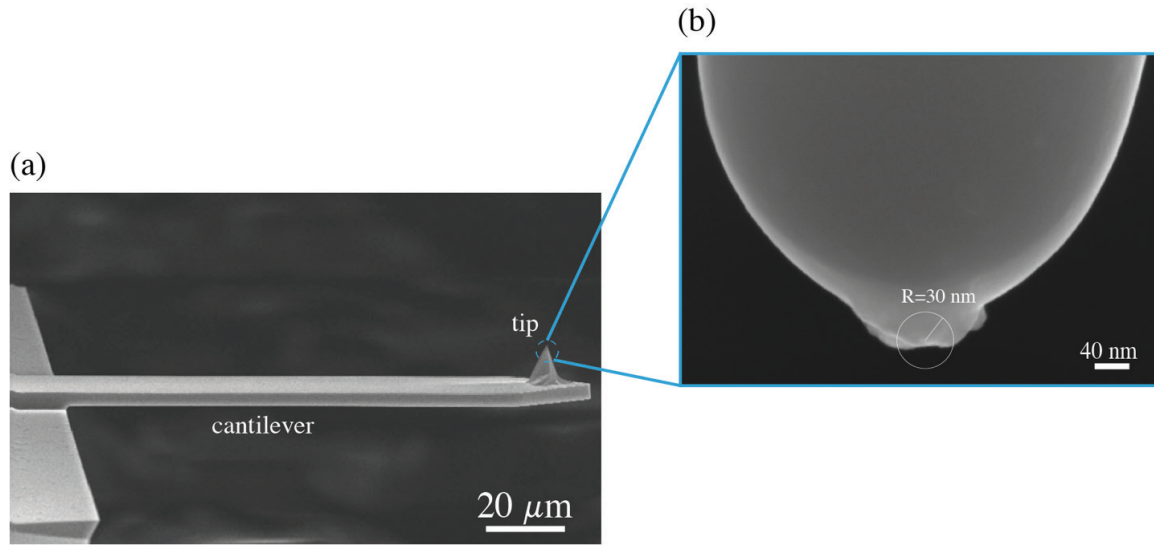


Figure 1:4 a) Cantilever used during experiments. SEM picture adapted from (9); b) SEM image of the AFM tip used during the three-point bending tests. At the end of the experiment, the AFM tip was found broken as well visible in the picture.

1.1.2 Electron microscopy

During my investigation to study the material microstructure and composition, electron microscopy techniques have been extensively used in particular transmission electron microscopy (TEM) and scanning electron microscopy (SEM).

At EPFL we have the opportunity for using various electron microscopy equipments: both TEM and SEM are available at center facility and research center, Interdisciplinary Center for Electron Microscopy (CIME).

1.1.2.1 Transmission electron microscope

The work of physicists of the early 20th century such as Henri Poincaré, Louis de Broglie or Hans Busch on electrons and electromagnetic lenses were the beginnings of what became in the early 1930s the electron microscope. Max Knoll and his student Ernst Ruska in 1931 presented images taken with the first two-lens electron microscope. The images already showed details of the order of ten nanometers (Berlin Technische Hochschule). Ernst Ruska received the Nobel Prize in Physics in 1986 for “*his fundamental work in electron optics, and for the design of the first electron microscope*”(2). Subsequently, the development of the electron microscopy was pushed, particularly after the Second World War, with great refinement of the resolution and image sharpness in the last decades.

Electron microscopy is a direct consequence of discovery by Nobel Prize winner de Broglie of the wave nature of the electron. Higher the energy of the electron, smaller is the associated wavelength $\lambda = h/p$ (p being the particle momentum), and better is the resolution, d , given by the Abbe's diffraction limit. An electron at an energy of 10 keV has a de Broglie wavelength of 0.01 nm. That's why the electron microscopes can achieve the highest resolution images, and literally allow, especially the TEM, to see the atoms! To go beyond this limit one has to use large particle accelerators. Just to compare, the extreme microscope is the CERN's Large Hadron collider: its 7 TeV protons allow to explore the matter with resolution (given by their quantum wavelength), of better than 10^{-18} m (attometer), however with a unique "equipment" which is 27 km long, full of a powerful superconducting magnet and very large "eyes" like ATLAS and CMS detector!

1.1.2.1.1 Principle

A TEM works essentially like an optical microscope, with the role of photons in the latter being taken over by electrons thanks to their wave behavior mentioned in the above section. It exists conceptually in two forms: TEM, where the incident beam on the sample is a plane wave, and STEM (Scanning Transmission Electron Microscope), which is closer to confocal optical microscopes. Modern microscopes operate in both modes.

Figure 1:5 schematizes the main components of a TEM. An electron gun is used to produce a beam. This beam then passes through a series of condenser lenses, whose role is to be able to adjust the size and angle of incidence of the beam. The beam then reaches the specimen, of which a first image is produced by the objective lens. It should be noted that the objective lens is the most important element because its quality strongly affects the resolution of the image. In addition, notice that the objective lens does not contribute significantly to the magnification (only by $\approx \times 10$), this role is carried out by projector lenses. It is worth noticing that lens in electron microscopy means coils generating a magnetic field, which focalizes an electron beam, very much as a glass lens focalize an optical beam.

After passing through the objective lens, the intermediate lens either form a second image, if its object plane coincides with the image plane of the objective lens, or form an image of the diffraction pattern, if its object plane coincides with the focal plane of the objective lens. By changing the value of the focal length of the intermediate lens (done in practice, by changing the current in the intermediate coils), the diffraction pattern of the image is easily obtained from the same area. Finally, the projecting lenses enlarge the image or diffraction pattern formed and the project onto the detector, which may be a fluorescent screen, or more commonly a scintillator coupled with a CCD camera.

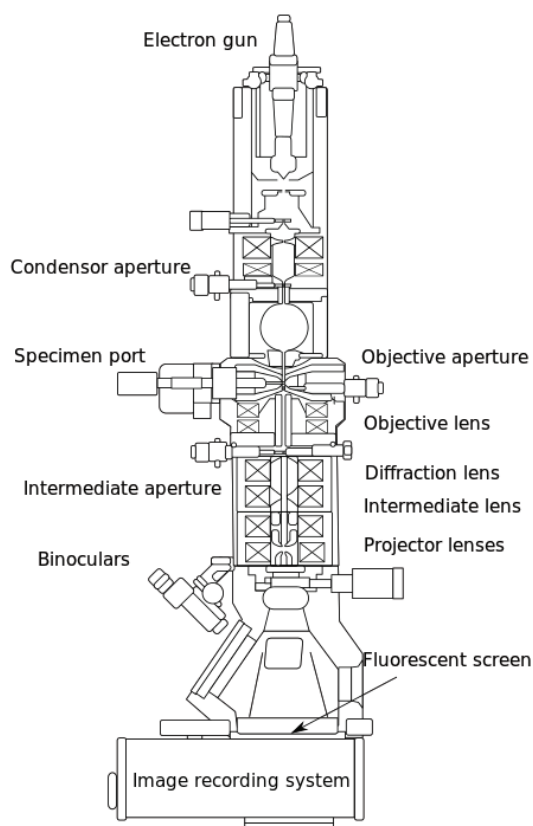


Figure 1:5 A simplified schematic drawing of the main components of a TEM. Fig. taken from Ref. (10).

In TEM only thin specimens can be observed because electrons have to be transmitted through the sample; the possible interactions between the specimen and the electron beam are shown in see Figure 1:6.

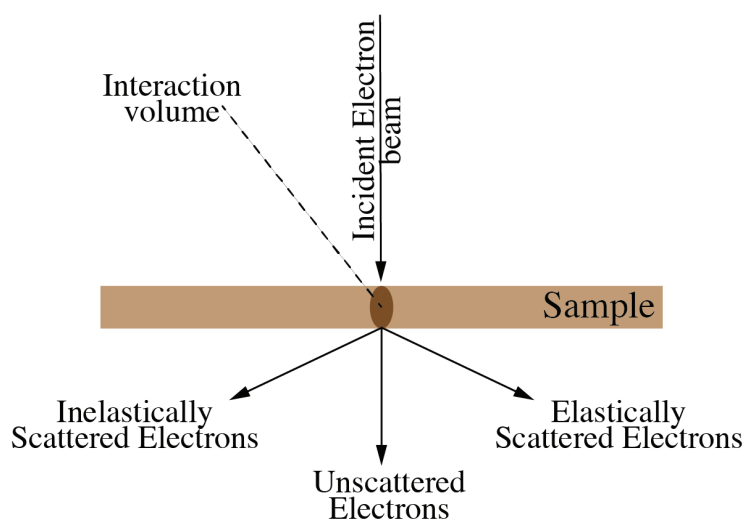


Figure 1:6 Draw of interactions between the sample and the incident electron beam.

Unscattered electrons: are the electrons not interacting with the thin sample and continuing straight. The bright-field image (BF) is composed of those electrons that have been selected by the objective aperture, positioned in the back focal plane of the specimen.

The transmission of unscattered electrons is inversely proportional to the sample thickness. In fact, in regions where the sample is thicker, the number of unscattered electrons will be less and the respective image will appear darker. Inversely thinner regions will have more transmitted electrons and will appear brighter.

TEM analysis is carried out using a FEI Talos microscope operated at 200 kV.

1.1.2.1.2 Sample preparation

The samples shall be thin enough (<100 nm) to be crossed by the electron beam. In our case, since we are dealing with nanoparticles or nanowires, the sample can be deposited directly on a grid, and then observed under TEM. Usually, the material is deposited on the grid in the following way:

- A drop of the nanomaterial from a suspension solution in ethanol/isopropanol
- Via a stamping method. The nanomaterial suspension is first filtered on a Teflon membrane with pores sizes $0.45\text{ }\mu\text{m}$ and subsequently stamped against the TEM grid for 1 min.

We used regular grids made with a thin film of pure carbon deposited on one side and also special heatable grids with a 15 nm SiN membrane.

1.1.2.2 Scanning electron microscope

In the scanning electron microscopy, an electron probe beam whose energy can vary from a few hundred eV to 40 keV is focused by the objective lens on the sample, various detectors surrounding sample collect the signals, i.e. electrons scattered all around the sample as well X-rays emitted in all directions and the image is formed step by step by sequential scanning of the sample with the electron probe. A schematic drawing of an SEM is shown in Figure 1:7. Under the impact of this electron beam, various types of electron-matter interactions result in the emission of different signals. These signals are collected to form an image of the surface of the object to be observed or to make a chemical analysis of the same surface. Unlike TEM, the SEM technique is used for imaging and analyze bulk specimens.

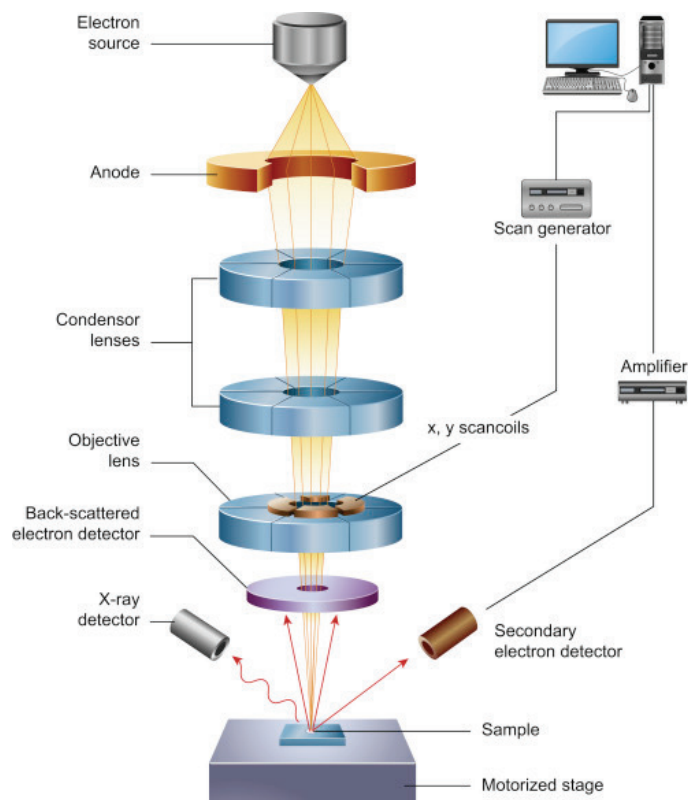


Figure 1:7 Scheme of an SEM microscope. Fig. taken from Ref. (11).

The main signals emitted in SEM are shown in Figure 1:8 with their area of origin in the electron-matter interaction volume. The main signals generally collected are the secondary electrons (SE) which have an energy of 0 to 50 eV (essentially topographic contrast), the backscattered electrons (BSE) which have high energy close to the energy of the incident beam (essentially for chemical Z contrast and crystallographic information) and the X-photons characteristic of the chemistry of the sample (chemical analysis). Auger electrons are not used in the characterization of our nanomaterial, but they are the ejected electrons with an energy characteristic typical of the target atoms.

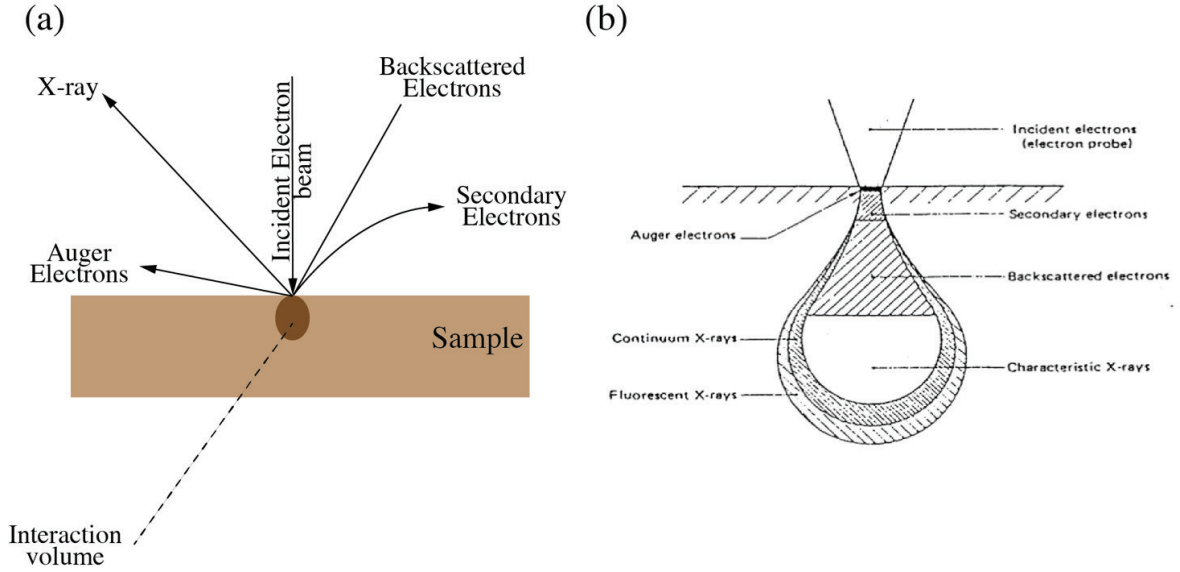


Figure 1:8 a) Interaction between the sample and the incident electron beam; b) Interaction volume and signal emission. Fig. taken from Ref. (12).

In this work, all SEM images are collected with a Zeiss Merlin (Gemini II column) electron microscope.

1.1.3 X-ray diffraction

X-ray diffraction (XRD) is a non-destructive analytical technique widely used in the characterization of crystalline materials. This is mainly used to identify the crystalline phases present in a material and to determine its crystallographic characteristics through the calculation of cell parameters.

In 1913 the English physicist Sir W. H. Bragg and his son Sir W. L. Bragg gave a simple explanation for X-ray diffraction by a crystal assuming that the incident X-rays were specularly reflected (i.e. the angle of incidence θ was equal to the angle of reflection) by parallel planes of atoms Figure 1:9, so that the diffraction condition is given by the equation (13):

$$2d_{hkl}\sin\theta = n\lambda \quad \text{Equation 1:1}$$

Where d_{hkl} is the atomic distance between parallel planes, λ is the X-ray wavelength, (in our experiments we used a Cu K_α radiation: $\lambda = 0.15406$ nm). The XRD diffractograms are acquired with a PANanalytical EMPYREAN diffractometer (θ - θ , 240 mm) equipped with a PIXcel-1D detector, at the Material Characterization Platform in our Institute.

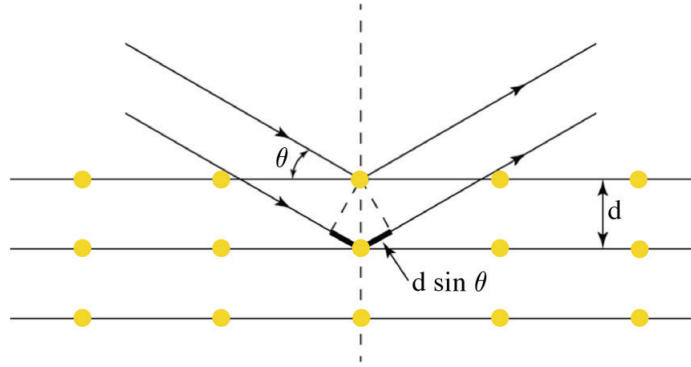


Figure 1:9 Schematic representation of the XRD mechanism.

XRD can be used on single crystals or powders; in our study, we make an XRD analysis of powder only. A wealth of information may be obtained out of a diffractogram. Here a non-exhausting list:

- From the positions of the various peaks and their intensity, we can identify the analyzed material by comparing these informations with the built-in databases. In this way, it is possible to identify the compounds present in the powder under examination and their crystalline form.
- From the angular position of the diffracted peaks, through Bragg's law, it is possible to evaluate the interplanar distance d_{hkl} of the planes of the atoms responsible for the diffraction effect; once known the Miller's indexes of these planes, it is possible to deduce the crystallographic constants of the compound under examination.
- From the full-width at half-maximum of the diffraction peak it is possible to determine the average size of crystallites composing the powder: the width at half-height $\beta_{1/2}^{hkl}$ is inversely proportional to the average crystallites size $\langle d \rangle$, through the Scherrer equation (14):

$$\langle d \rangle = \frac{K_s \lambda}{\beta_{1/2}^{hkl} \cos \theta_{hkl}} \quad \text{Equation 1:2}$$

Where, K_s is the Scherrer constant depending on the unit cell geometry (typically between 0.85 and 0.99) and θ_{hkl} is the Bragg angle. This formula is valid for crystallites with dimensions smaller than 100 nm, above which the formula diverges.

- From the intensity of the diffraction peaks, it is possible to trace the crystal structure and the position of the atoms or ions in the crystalline cell.
- From the intensity of the characteristic diffraction peaks of two or more crystalline forms present in the mixture in the sample, it is possible to determine the percentage in weight of these components in the examined powder.

1.2 Sintering procedures and tooling

The manufacture of sintered pieces takes place in two steps:

1. Powder compaction at cold (“green body” preparation)
2. Sintering process

The first step, shown in Figure 1:10, is intended to give to the sintered sample the desired shape. Powder compaction brings the particles into intimate contact, eliminating voids and increasing density. Once the sample is compacted, it can then be handled, even if its mechanical properties are very weak, and it is quite brittle. This cold forming of the sample is called “green body”.

The second step, the actual sintering is performed at high-temperature. The powder particles remain solid and heat diffuses through the contact points among particles. A solid-state diffusion bonding, usually enhanced at higher temperatures, is established and the joining surfaces grow.

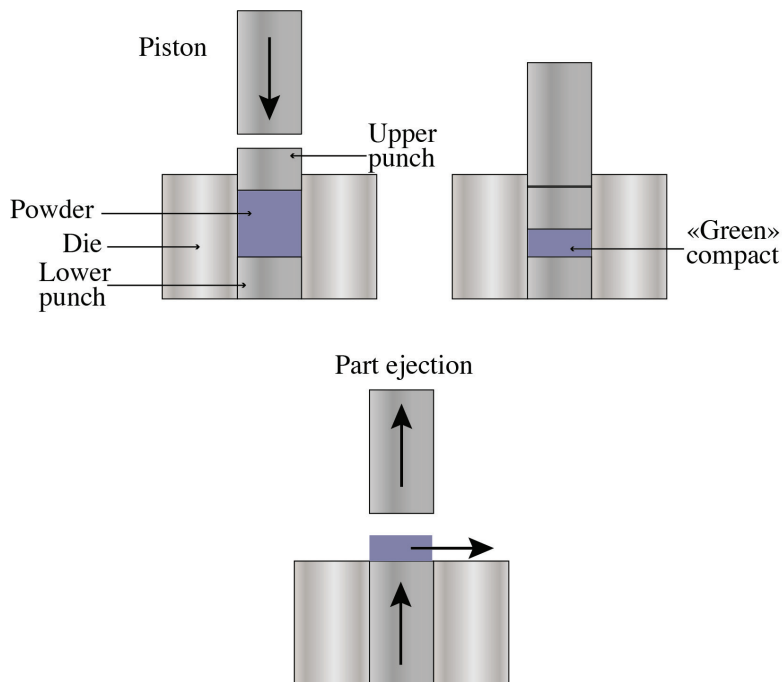


Figure 1:10 Schematic representation of a pressing in a closed-die.

However, between sintered particles remain empty pores, or voids, of various sizes and numbers according to the sintering parameters (time, temperature and pressure). It is possible to obtain sintered products that are almost pore-free, especially if the sintering is carried out under high pressure, which accelerates the diffusion mechanisms and enhances the growth of the bonding surfaces.

To deal with these issues, i.e. good mechanical properties and low porosity, in this work 3D pellets were made mainly via hot uniaxial pressing and spark plasma sintering technique (SPS) was used, too.

1.2.1 Hot Uniaxial Pressing

The hot uniaxial pressing (HUP) consists in pressing while the sintering process at high temperature takes place, at the same time. One needs a high-pressure containment vessel, where the pressure, though the force is applied usually from one direction (typically the top, see Figure 1:10) is then distributed almost uniformly in all directions. In our system, the powder was inserted in a closed-die of a diameter of 12 mm, and pressed with a piston at 65 kN. Once the pressure reached, it was maintained constant while the temperature was increased by switching on the electrical heater (the maximal reachable temperature in the system was 300°C) and kept for 15 min.

1.2.2 Spark Plasma Sintering

The other sintering technique used was spark plasma sintering (SPS). These experiments were conducted in collaboration at the Belgium Ceramic Research Center (BCRC). The SPS equipment of BCRC is HPD10 from FCT (Germany).

The powder is placed in between two graphite punches and inside a 20 mm diameter graphite diameter die (R7710 grade from SGL society), see Figure 1:11. The mass powder should be calibrated in advance to obtain the desired sample thickness at the end of the experiment.

A graphite foil, 0.35 mm in thickness, is placed between the sample and the die to assure a good electrical and thermal contact. Also, in order to avoid heat losses and minimize the temperature gradient on the sample, the die is surrounded by thermal isolating graphite felt.

Once the SPS chamber closed, it is evaluated to reach a rough vacuum of 10 Pa and then is kept under constant pressure using pistons while an electrical current is passed through the graphite and the powder to be sintered. In this way, the Joule heating is generated directly inside the sample. The SPS temperature is monitoring above 450 °C by a pyrometer passing through the drilled cylindrical pistons; below 450 °C, the temperature is controlled by the provided power. Experiments are made under direct current (DC) of 600 A and 5 V. During the experiment is it possible to record the shrinkage data by recording the initial and final distances between punches.

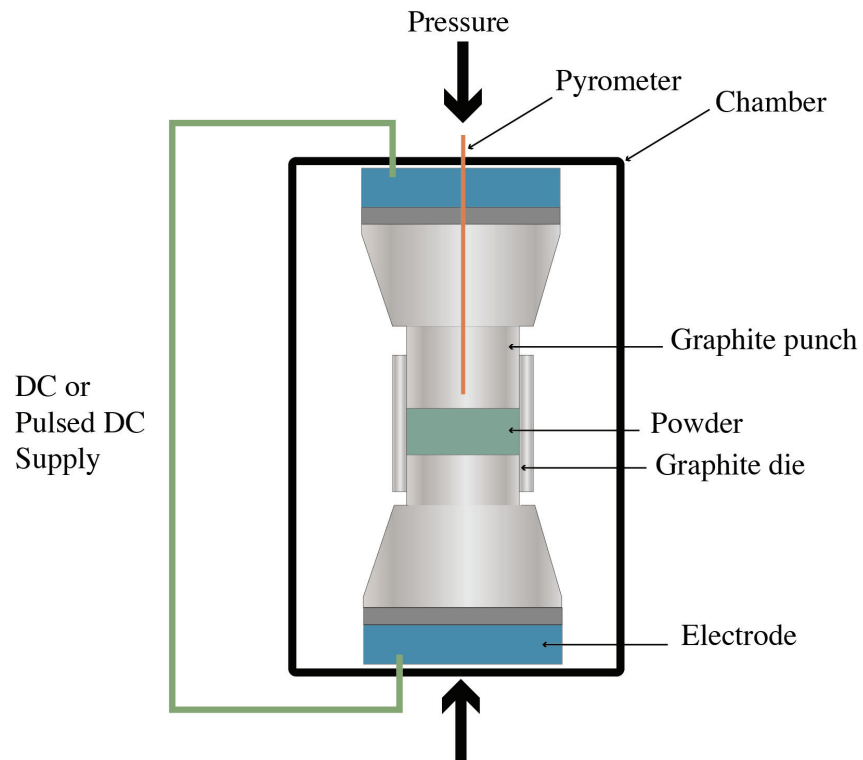


Figure 1:11 Schematic of SPS design.

Chapter 2 Structure characteristics of titanate nanowires

2.1 Introduction

Among different semiconductor oxides, titanium dioxide continues to attract considerable theoretical and experimental attention because of its technological relevance in applications such as environmental purification (15)(16), solar energy harvesting (17), memristors (18), catalysis (19), advanced ceramic materials and more. Different allotropes and morphologies of the compound are being examined: millimeter-sized single crystals (20), polycrystalline sintered ceramics (21), thin films as well as isotropic and anisotropic micron and nano-sized particles (22)(23). In most of the applications, titania is used as a nanoparticle-based coating, deposited by blading, spin coating, spraying or sol-gel techniques (24). Subsequent heat treatment is often required to increase the crystallinity and integrity of these functional coatings. During the thermal treatment, the differences in the thermal expansion of the support materials may cause additional stresses that can lead to the detaching or overall failure of the mesoporous film. Much has been learnt from recent studies of the coarsening behavior of TiO_2 nanostructures of nearly spherical, isotropic nanoparticles. Indeed, the degree of the particle anisotropy can induce important shape-dependent variation in properties of the material, which raises the question of how the coarsening of anisotropic particles proceeds at the interfaces and in the bulk (≥ 100 nm from the interface).

For these reasons, studying the kinetics of the thermal coarsening of the elongated titanates is fundamentally important to control its structural, electronic and mechanical properties. Controlling these properties is essential for special applications as thermal super insulators (25), magnetism (26)(27), photocatalysis (28), and self-cleaning surfaces (29), photodetectors (30), fiber polymer reinforcement (31), biofunctionalized nanocarriers (32)-(34), humidity (35) and pH (36) sensors and mesoscopic solar cells (21).

In this chapter, a general description and state of the art of titanium dioxide will be presented, then we will focus on titanate NWs and in particular, I will discuss on the temperature-dependent structural and geometrical evolution of suspended individual titanate NWs or individual NWs deposited on a substrate, called 2D geometry, and of assembly of nanowires, called 3D geometry.

2.2 Crystal properties of titanium dioxide

2.2.1 A brief history, applications and economical importance of TiO_2

Titanium is the ninth most abundant element in the earth's crust ahead of hydrogen and behind magnesium.

Titanium dioxide (TiO_2) was discovered in 1791 by the British reverend William Gregor in its “ilmenite” form under the name of “menaccanite” (with the formula FeTiO_3). It was only 4 years later that Martin H. Klaproth, a German chemist, named it Titanium, after the myth of the Titans. He was mistaken, what he identified as titanium was in reality TiO_2 under rutile form, a correction made a few years later (37).

It is used as a whitening agent and white pigment; the discovery of this pigmentary property dates back to 1821 and was first used for artistic purposes in composite form. The growth in the use of white TiO_2 pigment occurred in the 20th century:

- In 1910 the American M. A. Hunter developed a method for the production of pure TiO_2 , which allowed mass production.
- In 1916 it was first used as a white pigment in the building industry.
- In 1940 Kroll develops a process for the economical production of titanium. Start of the industrial development of titanium.
- Its use then extended to various industry: textile, food, cosmetics... (38)

We can see on the graph below (Figure 2:1) the evolution of the production of this pigment in the last century:

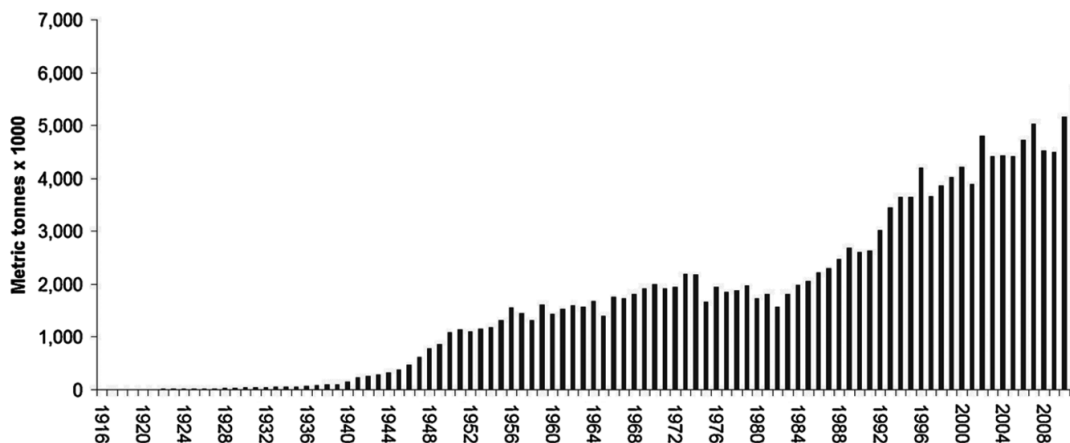


Figure 2:1 TiO_2 production by years in all countries of the world. Fig. taken from Ref. (39).

Although known as a pigment, TiO_2 was also used at the end of the 19th century as an agent opacifier and additive, on varnishes and glass products to increase resistance to acids. It was in 1929 that the photocatalytic property of TiO_2 was discovered, following long exposure to the sun, wall discol-

oration has been observed on the surface of buildings covered with TiO_2 pigments. However, it was not until 1932-1934 that a document describing this property was published and 1938 for the information to be considered reliable by the scientific community.

In 1969, a major breakthrough took place, the photolysis of water. A semiconductor electrode composed of TiO_2 in its rutile crystalline form is developed and used.

Since this date, studies on the photochemical properties of TiO_2 have experienced significant growth, between 1970 and 1990. From 2000, and still at present, nano-engineering and nanotechnology based on TiO_2 show huge development.

Since 2010, more than 10,000 papers on TiO_2 have been published every year worldwide, see Figure 2:2.

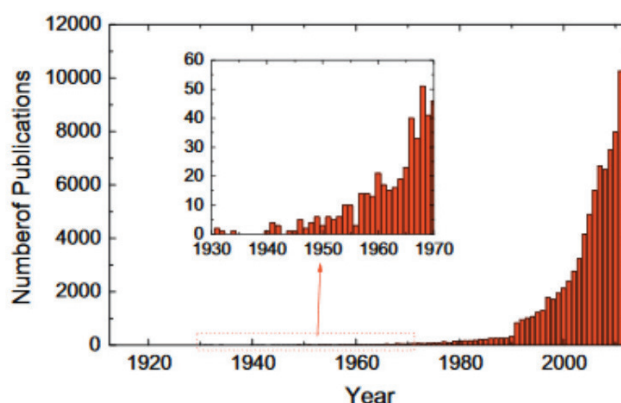


Figure 2:2 Number of research papers published between 1913 and 2013 containing the term TiO_2 . Fig. taken from Ref. (40).

TiO_2 nanoparticles have many applications in various industries, such as construction, cosmetics, textiles, and renewable energies which are the most important, but they are also found in the food, automotive, air treatment industries and medical sectors (Figure 2:3).

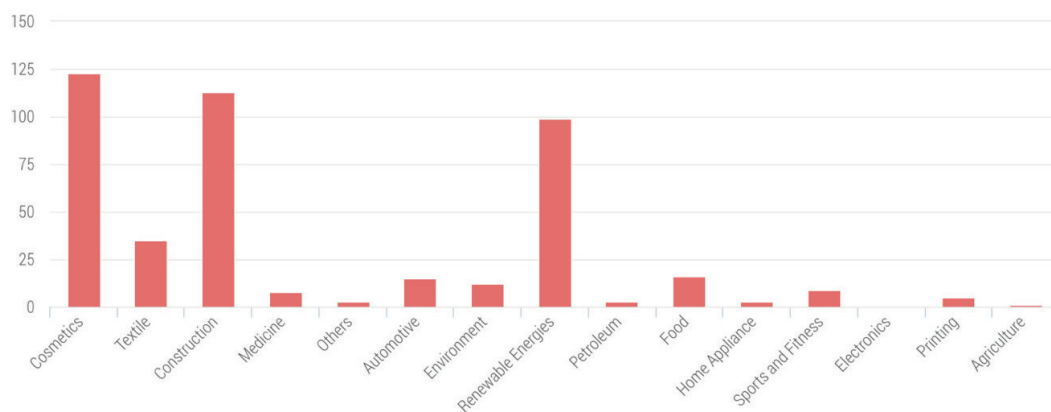


Figure 2:3 Number of TiO_2 nanomaterials used in products by industrial division. Fig. taken from Ref. (41).

Titanium dioxide has an expanding market: according to a study published in December 2014 in the Statnano website (42), 180 products contain nanostructures based on TiO_2 . These products are marketed by 32 companies, the vast majority of them from North America, Asia and Europe. China and the United States are leaders in this field with 53% and 25% of the products respectively based on TiO_2 , see Figure 2:4.

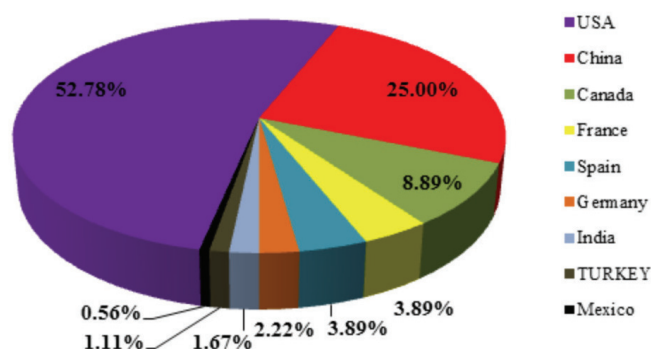


Figure 2:4 Top countries in the production of TiO_2 nanoproducts. Fig. taken from Ref. (42).

According to market estimates, in 2005 the production of nanoparticles of TiO_2 was close to 2000 tons per year, representing a turnover of \$70 million (€51 million). With the increase in demand in Asia, this figure will increase significantly in the coming years due to the growing demand for cosmetics, construction or the increasing use of medical nanoparticles (43).

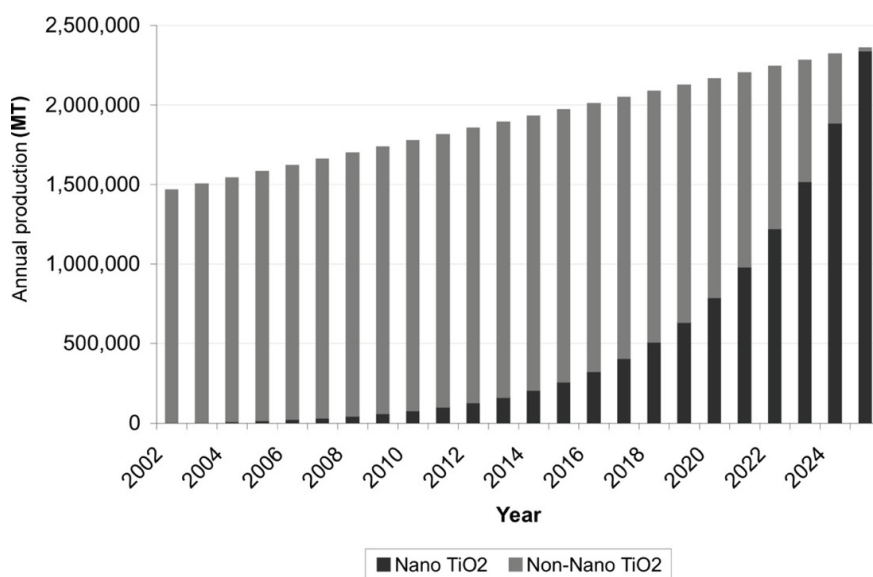


Figure 2:5 Projected global production of TiO_2 nanoparticles from 2002 to 2024 relative to non-nanoscale TiO_2 . Fig. taken from Ref. (44).

Figure 2:5 shows the projected evolution of the production of TiO_2 NPs from 2002 to 2024 compared to non-nanoscale TiO_2 . The study predicts an explosion of nanometric TiO_2 production in the coming years to expect 100% production in a decade, i.e. nearly 2 million tons.

2.2.2 Titanium dioxide structure and properties

TiO_2 exists in three different polymorphs:

- rutile (discovered in 1803)
- anatase (discovered in 1801)
- brookite (discovered in 1825).

Rutile is the most common phase, while brookite is the rarest. The other 8 phases exist, too, of which three are stable: monoclinic system TiO_2 (B), tetragonal system TiO_2 (H) and orthorhombic system TiO_2 (R). The remaining five phases exist under extreme conditions; namely applying pressure to rutile and anatase more exotic phases start to appear. However, only rutile and anatase are the allotropes widely used for numerous TiO_2 applications. Anatase is a metastable form and turns irreversibly into rutile phase at high temperature, around 600 °C. We can find examples in the literature that by doping TiO_2 the anatase to rutile transformation can be accelerated (45)(46).

Both anatase and rutile phases, are composed by Ti^{4+} titanium ions at the center of octahedra of six O^{2-} ions; each oxygen has three titanium ions neighbors.

Anatase has a tetragonal crystal structure with $I4_1/amd$ space group and with lattice parameters: $a=3.782 \text{ \AA}$, $c=9.502 \text{ \AA}$ (47); also rutile has a tetragonal crystal structure with $P4_2/mmm$ space group but different lattices parameters: $a=4.593 \text{ \AA}$, $c=2.958 \text{ \AA}$ (47). Their respective crystal structures are represented in Figure 2:6.

Anatase is transparent in the visible spectrum (2.48-2.56 refractive index, 96% of the light is reflected (48)) and insulating with a band gap of 3.4 eV (49), while rutile has a band gap of 3.0 eV (50)(51).

TiO_2 can be synthesized with various shapes at the nanoscale, as it is shown in Figure 2:7. A great variety of morphologies can be achieved as:

- Nanoparticles: spheroidal shape (Figure 2:7a)
- Nanofiber: long parallelepiped-shape (Figure 2:7b)
- Nanosheet: planar 2D structure (Figure 2:7c)
- Nanotube: cylindrical with a circular hole along their length (Figure 2:7d)

- Nanorod: solid cylindrical with a circular base

Nanowires, nanobelts, nanoribbons can be generally classified as nanofibers. In this thesis I will use these terms describing the same particle shape depicted on Figure 2:7b and Figure 4:5b as synonyms.

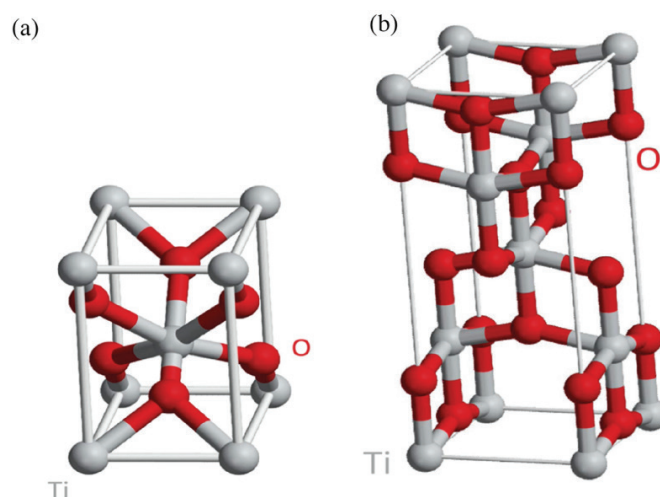


Figure 2:6 a) Rutile crystal structure; b) Anatase crystal structure. Oxygen atoms are colored in red and Ti atoms are in grey. Image source: Wikipedia.

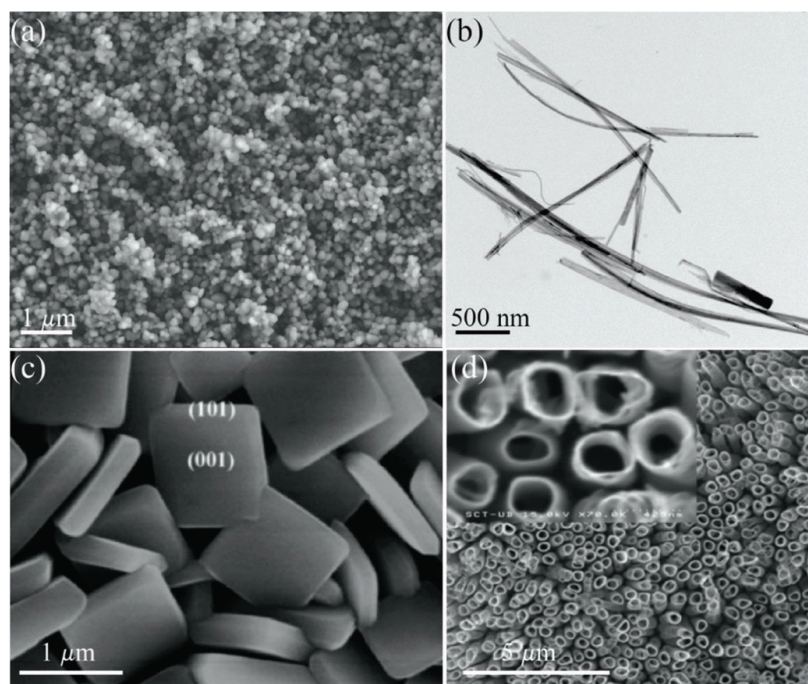


Figure 2:7 a) SEM picture of TiO_2 nanoparticles; b) TEM image of titanate nanowires; c) TiO_2 nanosheets (52); d) TiO_2 nanotubes (53).

Anatase nanowires precursor, from which they are obtained by thermal treatment, are titanates nanowires $\text{H}_2\text{Ti}_n\text{O}_{2n+1}$. Their synthesis and properties are exposed in the next section 2.2.3. I would like to put an emphasize on and illustrate the wide variety of structural, thermal, chemical and mechanical transformations that a TiO_2 nanoparticle can experience in Figure 2:8.

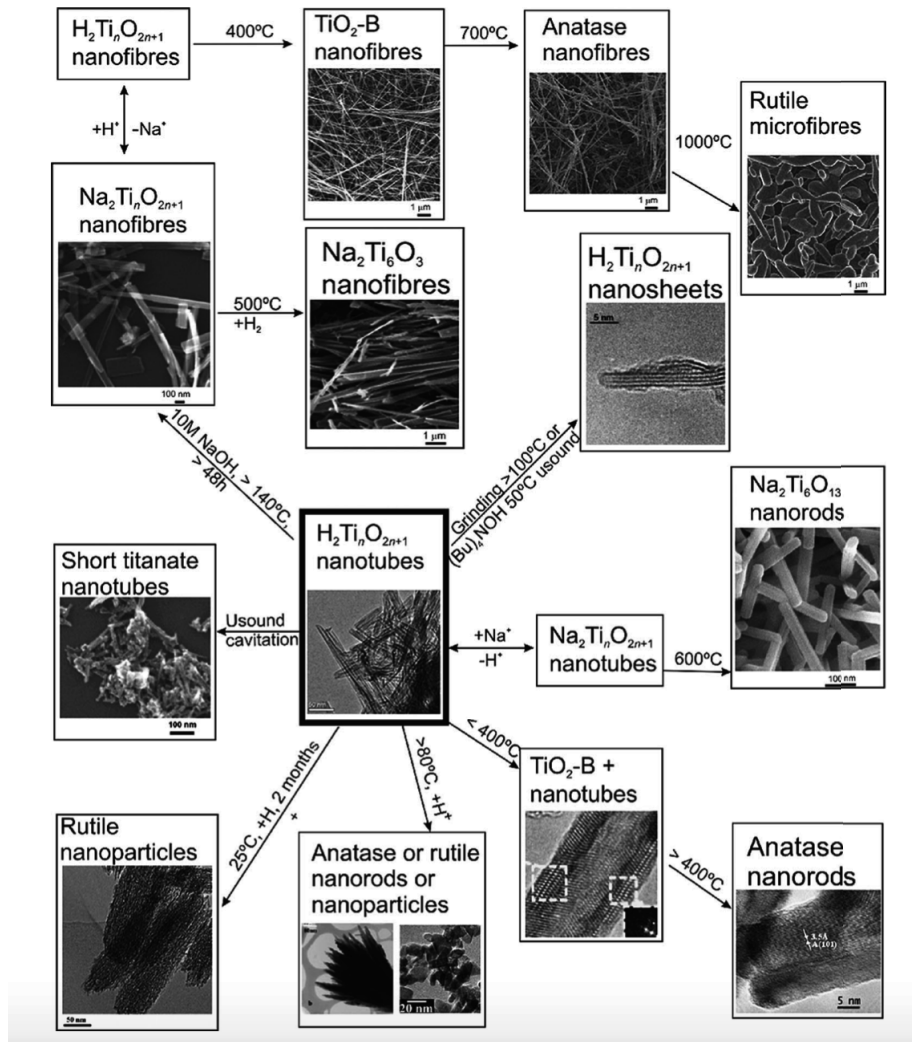


Figure 2:8 Transformations of TiO_2 nanowires. Fig. taken from Ref. (54).

2.2.3 Titanate nanowires

2.2.3.1 Synthesis

Protonated titanate nanowires ($\text{H}_2\text{Ti}_3\text{O}_7$) are prepared by a two-step hydrothermal process; the typical synthesis procedure is described in (21). A mixture of anatase and NaOH solution is treated at 130°C for 36h. The resulting white powder underwent a second hydrothermal treatment at 200°C

while mixed with KOH. The obtained nanowires are subsequently collected, washed and dried at 250 °C.

2.2.3.2 Characterization and phase transformation

An assembly of nanowires is shown on the TEM image in Figure 2:7b. They have belt-like shape and their width ranges from 10 to 100 nm and their length can go up to tens of μm . On the TEM image and the corresponding selected area electron diffraction (SAED) pattern in Figure 2:9a, one can clearly notice the crystalline layered structure of the NWs with a gallery spacing of 0.7 nm. This observation of the gallery spacing is feasible when the belt-like nanowire is laying in a tilted position, with its thinner sides on the substrate. The crystalline structure of titanate NWs is also visible on the XRD diffractogram, Figure 2:9c, showing reflections belonging to the trititanate phase (at $2\theta = 9$, 24.5 and 28°).

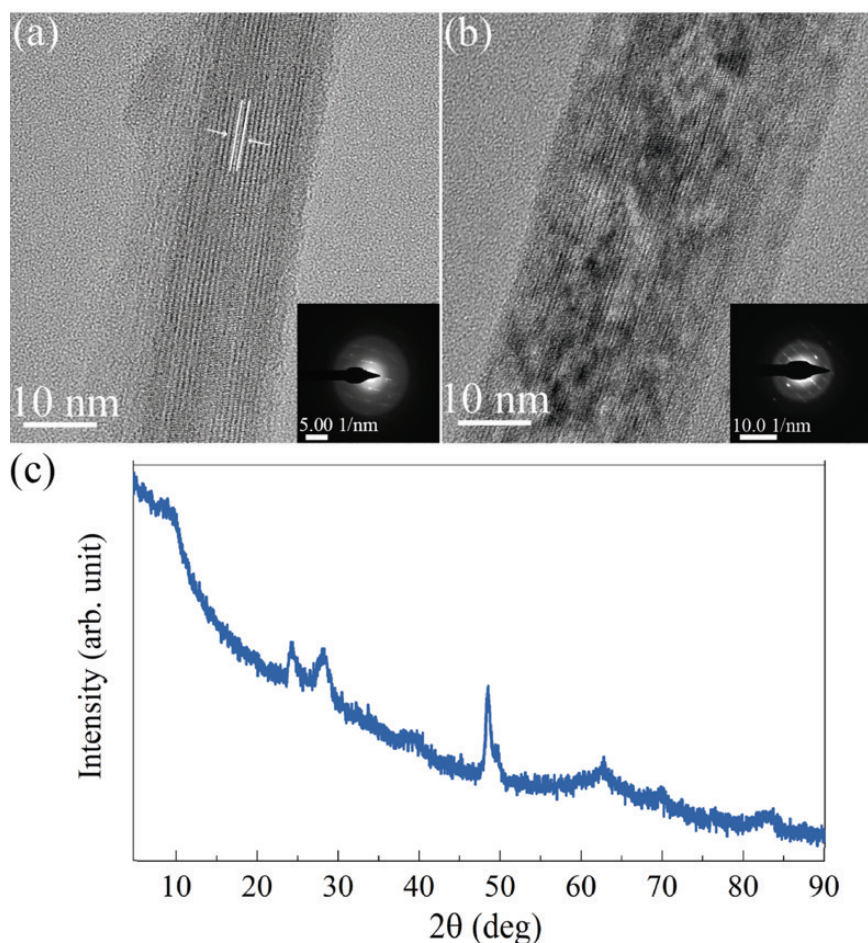


Figure 2:9 a) TEM image showing the layered nature of the NW in titanate phase, inset: corresponding diffraction pattern; b) TEM image showing the NW in anatase phase, inset: corresponding diffraction pattern; c) XRD profile titanate powder.

Titanate NWs after heat treatment at 600 °C recrystallize to anatase, Figure 2:9b and Figure 2:10a, according to the following equation:



This recrystallization is evidenced in Figure 2:10b via TGA measurement of few mg of titanate nanopowder in an inert gas (Argon). The weight loss of adsorbed water on the surface and the gallery spacing of the layered titanates is not visible on the graph. That fraction was evaporated during the temperature stabilization phase prior to the TGA measurement start. Only a minor 0.3 wt% weight loss is shown on the graph, which is clearly lower than the adsorption capacity of this layered oxide.

Between 200 and 600 °C, a weight loss of 5.5 wt% was detected. This is due to the disappearance of highly bound crystalline water and the transformation of the titanate phase to anatase (Figure 2:10a).

Furthermore, between 600 and 900 °C, only minor weight loss 0.1wt% was detected. This weight loss is probably, due to the loss of oxygen atoms (non-stoichiometric TiO_2 phase) while the appearance of the TiO_2 (B) minority phase, with the same molar mass, should not affect this point.

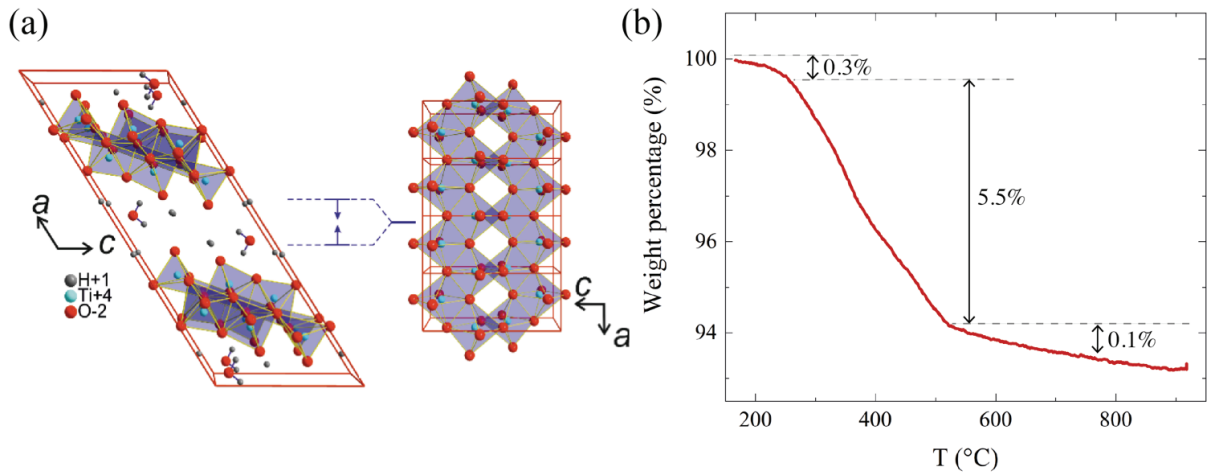


Figure 2:10 a) Titanate to anatase crystallization; b) Weight loss versus temperature evaluated via TGA measurements on $H_2Ti_3O_7$ powder. Dashed lines separate the three phases as a function of temperature.

2.2.4 Oxygen vacancies role in TiO_2

A typical defect in TiO_2 is the presence of oxygen vacancies in the crystallographic structure. By removing an oxygen atom from the structure, implies a strong influence on the optical and electronic properties of the material. The typical process to create defects is simply submitting a TiO_2 sample

to a heat treatment in a reductive atmosphere above 300 °C. The required energy to extract an oxygen atom from its surface is the following (Ref. in the literature (55)):

$$E_{vac} = \left(E(Ti_N O_{2N-1}) + \frac{1}{2} E(O_2) \right) - E(Ti_N O_{2N}) \quad \text{Equation 2:2}$$

At high-temperature sintering, TiO_2 loses oxygen and these shallow states created by oxygen vacancies decrease the electrical resistivity. Resistivity versus temperature has been measured for two samples sintered at 1100 and 1300 °C via spark plasma sintering method, their trend is illustrated in Figure 2:11.

For the sample sintered at 1100°C, for a temperature $T > 240$ K we obtained activation energy of $E_0 = 19$ meV and for $50 \text{ K} < T < 80 \text{ K}$ we obtained $E_0 = 23$ meV. The sample treated at 1300°C, for $T > 240$ K we obtain an activation energy of $E_0 = 46$ meV and for $40 \text{ K} < T < 70 \text{ K}$ we obtain $E_0 = 22$ meV. We can conclude that the activation energy extracted at low temperatures is comparable for these two samples.

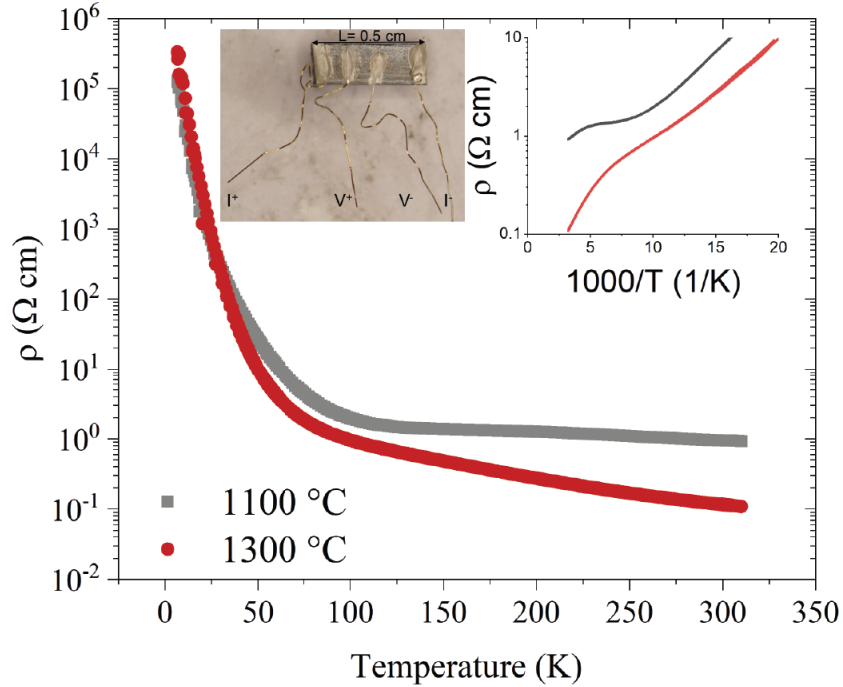


Figure 2:11 Resistivity measurements versus temperature of titania pellets sintered at 1100 and 1300 °C; in the inset the measured sample in the four-point configuration contacted with gold wires and silver paint. The color of the sample is black, due to the oxygen vacancies which act as color centers.

Due to the oxygen vacancies in TiO_{2-x} , distorted octahedral Ti^{3+} appear connected by corner and edge, causing various interconnection. Ti^{3+} is a spin -1/2 paramagnetic species with electron configuration $[\text{Ar}]3d^1$. The degenerate orbital of the free Ti^{3+} ion is split in crystals due to the effect of the crystal field. We used electron paramagnetic resonance (EPR) to provide a precise determination of the concentration of paramagnetic centers in ppm of the samples sintered at high temperature via SPS and whose resistivity is measured above.

Table 2:1 Spins concentrations in three samples sintered via SPS.

<i>Sintering temperature</i> (°C)	<i>Spins concentrations</i> (ppm)
900 °C	421
1100 °C	485
1300 °C	865

It is visible from Table 2:1 that all three samples contain a significant number of Ti^{3+} defects and follow an increase of spin concentrations with increasing sintering temperatures.

2.3 Thermal coarsening of individual and assemblies $\text{H}_2\text{Ti}_3\text{O}_7$ nanowires

This study aims to shed light on the temperature-dependent structural and geometrical evolution of suspended individual titanate nanowires or individual nanowires deposited on a substrate, called 2D geometry, and of assembly of nanowires, called 3D geometry. We have identified some unexpected differences in the phase stabilization and surface diffusion behavior of the 2D and 3D assemblies.

2.3.1 Experimental

2.3.1.1 Preparation of 2D system

Individual titanate nanowires are deposited from an ultrasonicated suspension via a stamping method. The nanowire suspension was first filtered through a Teflon membrane with pores sizes 0.45 μm and subsequently stamped against the silicon substrate for 1 min. Subsequently, the Teflon membrane was removed, and the well-separated titanate nanowires remain on the silicon substrate due to much higher surface adhesion on silicon than on Teflon.

2.3.1.2 Preparation of 3D pellets

Titanate powder was loaded into a graphite die (diameter 20 mm) and sintered via spark plasma sintering (SPS) under 50 MPa pressure. Sintering is performed with a heating rate of 50°C/min with a 2 min dwell at the target temperature. For the Vickers hardness test, a commercial Sigma Aldrich anatase TiO₂ white powder was used; sintering procedure is described elsewhere in (25).

2.3.2 Results and discussion

Thin films of titanate nanowires were prepared by the wet-chemical method. H₂Ti₃O₇ based porous films with thicknesses of 10 and 70 µm were fabricated on a technologically relevant conductive glass substrate coated with F-doped (FTO) by doctor blading method. In order to promote the phase transformation from titanate into TiO₂ anatase phase, whose crystalline structures are shown in Figure 2:10a, the resulting porous coatings were annealed at 500 °C in air. Figure 2:12a shows the representative photographs and the corresponding top-view surface morphologies imaged by SEM. Despite the fact that the same deposition technique and annealing process was used for both layers, failures such as peeling can be observed in the case of the thicker, 70 µm thick, film. Top-view SEM micrographs confirm that the adhesion quality of the films to the FTO substrate was dissimilar after the sintering. Plenty of cracks 50-200 µm in length formed on the surface of the thicker layer, while uniform and flat surface with no observable cracks was characteristic for the 10 µm thick layer.

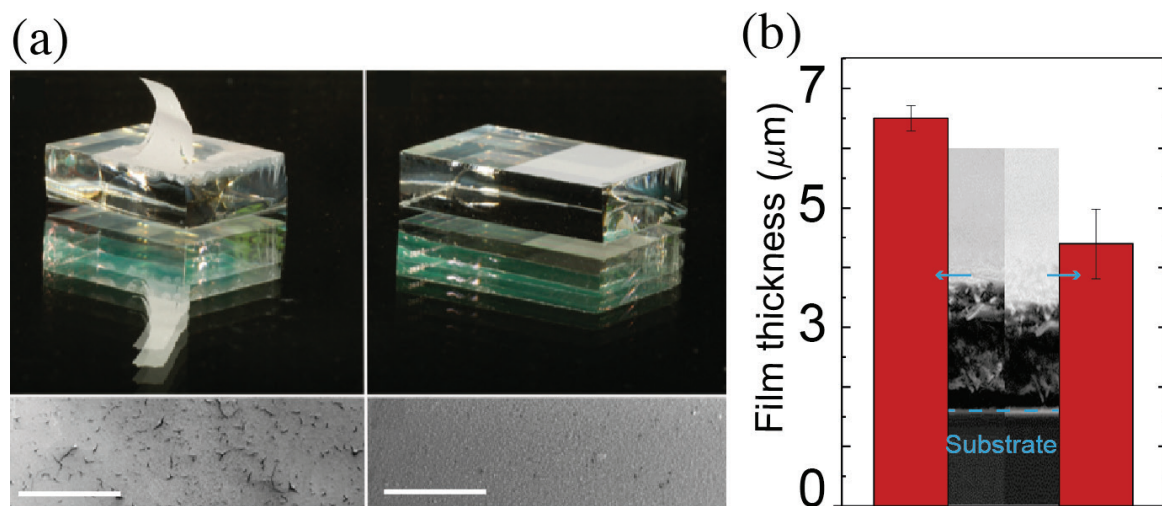


Figure 2:12 a) Titanate films of 70 and 10 µm (from left to right) and the respectively SEM morphology, the scale bars correspond to 1 mm; b) Film thickness before and after the sintering and the corresponding profile (inset).

The top-view SEM graphs (Figure 2:12a) taken before and after the sintering process confirm that the, 10 µm thick film (the thinner one) was well attached to the FTO glass. It is noteworthy, that the

titanate to anatase recrystallization induced about 30% shrinkage in the film thickness (Figure 2:12c, inset). This observation was further confirmed by a series of alpha step measurements (Figure 2:12c). These findings precisely portray that the sharp interface between the two dissimilar materials might be the weakest point in the system. As mentioned before, these stresses may result from the different thermomechanical properties of the two materials being combined and processed. If the relative deformations between the layers occur before the material fracture toughness increases to a level sufficient to withstand the stresses, the composite will not be able to undergo a crack-free process. However, the susceptibility of the interfaces to these types of failures is influenced by more than just the differences in the thermomechanical properties of the combined materials. Geometrical effects such as sharp corners, heating and cooling rate, particle size and shape, particle size distribution, orientation of the particles, porosity, degree of crystallinity and crystal phase change could have a significant role on possible crack formation and propagation between the adjacent layers. Many studies have been reported that, during the thermal annealing of elongated titanates, the material can undergo transitions to several crystalline phases such as TiO_2 (B), $\text{Na}_2\text{Ti}_3\text{O}_7$, anatase, rutile (54)(56)(57) depending on the annealing temperature and phase purity of the starting material.

In order to understand the sintering behavior of elongated titanate-based 3D coatings, we decided to study the temperature-dependent structural and geometrical evolution of its building “bricks”, the individual titanate nanowires, and compared it to the behavior of the sintered films.

2.3.2.1 Analysis of 2D system

We have measured the dimensional change of 21 individual nanowires under repetitive annealing in air, increasing temperature by 200 °C at each step, going from room temperature up to 1000 °C.

The changes in height were measured by means of AFM, while SEM images allowed us to quantify length and width variations. The dimensional variations such as, the cross-section and contact surface area and total volume after each annealing step are summarized in Figure 2:13.

SEM and AFM images of two nanowires close to each other taken as-deposited (RT), and after heat treatments at 600 °C and 800 °C in Figure 2:13a.

During the heat treatment from RT to 200 °C, the average nanowire height is reduced by 18.7%, while negligible change in the length and width was observed. At the annealing temperatures of 400 °C and 600 °C, the average height reduction was 20.9% and 23.7% respectively. Again, no change in the width and length has been observed as compared to the original room temperature values. At higher temperatures (above 600 °C), drastic changes in all the dimensions of the nanowire occurred. Annealing temperature of 800 °C caused significant nanowire enlargement in the plane of the substrate (Figure 2:13c). The average height was drastically reduced down to 20% of the RT value, accompanied by a pronounced change observed in the average nanowire width, which became four times larger as compared to the original value. However, the length slightly increased by 4%. The total volume of nanowires remained roughly constant, see Figure 2:13c.

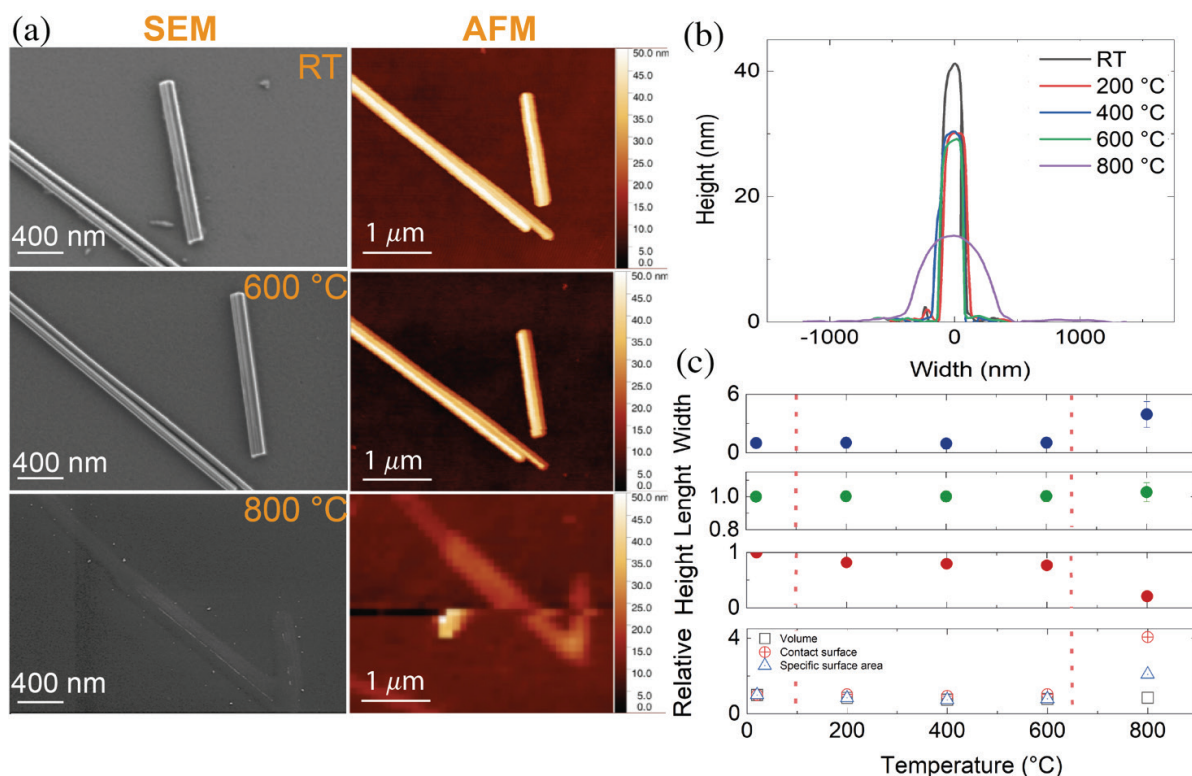


Figure 2:13 a) SEM and AFM of two nanowires close to each other, just after deposition at room temperature, after 600 °C and after 800 °C heat treatment. Statistics of geometrical parameters of individual nanobelts on a SiO₂ substrate after different heat treatment; b) Nanobelt cross-section; c) Relative change from the initial value of all three dimensions and the total volume, the contact surface area and the specific surface areas: the vertical dashed lines separate the three-particle coarsening regimes.

These results allow us to identify two annealing temperature-dependent geometrical phase transformations of nanowires, hereafter called phase-change 1 (TTA-Titanate to Anatase recrystallization from RT to 600 °C) and phase change 2, which are indicated by the dashed vertical line in Figure 2:13c. The size change in phase change 2 is driven by diffusion mechanism typical of our nanowires.

In phase-change 1, significant shrinking of the height occurred, while the length and width remained constant indicating minimal to no surface diffusion during the phase transformation.

The as-deposited nanowires possess a layered structure composed of titanium centered octahedra, indeed, and it can be indexed as monoclinic H₂Ti₃O₇. Here, various positively charged cations stabilize the structure, depending on the applied synthesis and post-synthesis procedure (ion-exchange). The physisorbed and chemisorbed water, (e.g. the hydrate shell of the balancing cations as well as the titanium centered octahedra build host layer) accounts for a significant H₂O content of the material. As a consequence, the one-dimensional shrinkage at 200 °C can be simply explained by the loss of loosely bound water adsorbed on the surface and in between the gallery spacing of the titanate layers. Further annealing leads to loss of strongly bound structural crystalline water followed by

the titanate to anatase recrystallization. For ascertaining the experimental results we compared the volumetric parameters of the unit cells of the monoclinic protonated titanate $\text{H}_2\text{Ti}_3\text{O}_7$ and the resulting TiO_2 anatase phase (see Figure 2:10a) for the crystallographic representation of the two phases). In our calculation, the number of Ti atoms in the two compounds was kept constant. The theoretical volumetric reduction in the trititanate-anatase transformation was found to be 20%. Hence, this theoretical value is in good agreement with the experimental observations.

Following phase change 2, a thermally activated anomalous particle coarsening was observed. The nanowire height decreased drastically. In parallel, the width and length increased significantly, resulting in about a factor of 4 increase in the nanowire-support contact area. Since the annealing temperature was far below the melting point of titania (1843 °C) the substantial change in the shape of the elongated particles is ascribed to a surface diffusion process. Taking the geometrical parameters measured by AFM and SEM the surface area change of individual nano-objects has been determined from Figure 2:13b and c.

Based on the classical Ostwald ripening model, it was expected, that upon elevating the annealing temperature the surface area of the nanoparticles would systematically decrease. This was actually verified for phase transition 1, where the surface area decreased by a few percents, driven by the 20% reduction of the height while keeping the other dimensions almost constant. However, we found out that following phase change 2, passing from 600 °C to 800 °C annealing temperature, the surface area of the nanowires increased by 300%. This unexpected behavior of the surface area appreciably differs from the classical Ostwald ripening surface diffusion model, where the system tries to reduce its surface area to reach a thermodynamically more stable configuration. The direction of the titanium oxide migration was found to be independent of the orientation of the SiO_2 surface, hence the measured diffusion path lengths were identical in all the directions.

We have further investigated this phenomenon via Raman spectroscopy. The spectral lines versus Raman shift measured on samples submitted to different annealing temperatures, 600, 800 and 1000 °C are plotted in Figure 2:14a.

The perfect overlapping of the spectra taken at low and high temperatures clearly indicates that the elongated fibers remain in the metastable anatase phase without transformation to the thermodynamically expected rutile phase. This means that in these individual wires, the anatase phase can remain stable up to 1000 °C and the increase of the width, with an increase of the surface area is driven by titanium oxide diffusion mechanism at the contact surface with the surface. Surface wettability and topotactic effects, such as epitaxial strain (58)(59), may have important roles in the metastable phase stabilization.

The surface diffusion mechanism is clearly recognizable and visualized in SEM images of Figure 2:14b and c. In Figure 2:14b, the SEM micrograph depicts nanowires on SiO_2 surface and one nanowire suspended over a microfabricated hole.

Figure 2:14c shows the same zone on the chip after a heat treatment at 800 °C in air. The fibers in contact with the surface show a substantial increase in width and the contact area due to a surface diffusion mechanism. Interestingly, in the case of the suspended nanowire, the area in contact with

the surface grew, however, the suspended part maintained its dimensions, and actually experienced a 10% reduction in width. This indicates that the coarsening and diffusion of anatase in nanowire form is substantially inhibited in the absence of a substrate.

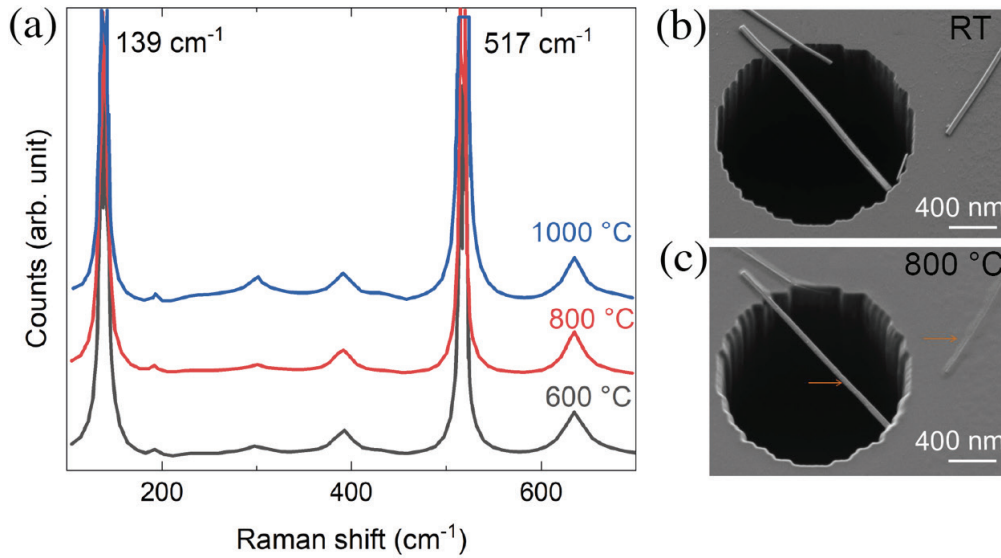


Figure 2:14 a) Raman spectroscopy of an individual nanowire at 600, 800 and 1000 °C heat treatment; b) SEM of a nanowire suspended over a microfabricated hole at room temperature; c) SEM of the same nanowire after heat treatment at 800 °C in air.

2.3.2.2 Analysis of 3D system

In this section we report the investigation on titanate nanowire coarsening in the absence of surface effects. We prepared various 3D assemblies, for instance porous pellets having 1.5-2 mm thickness, via SPS method. Based on the XRD and SEM data, coarsening effects in these pellets similar to the ones observed in nanowires can be identified. In the phase change 1 (TTA-Titanate to Anatase recrystallization from RT to 600 °C, sample in Figure 2:15a, the loss of crystalline water followed by the titanate to anatase recrystallization was taking place, as inferred by the disappearance of the $2\theta = 10^\circ$ peak, originated from the gallery spacing in the layered titanate. The characteristic anatase diffraction peaks appeared after sintering at 500 °C (Figure 2:15c) with the most intense peak at $2\theta = 25.2^\circ$ (101). Further sintering to 600 and 700 °C resulted in an increase and narrowing of the intensities of this at 2θ , indicating the grain growth and crystallinity increase of anatase crystallites. Most important the elongated particle shape was well preserved, as it can be seen in the SEM picture of Figure 2:15a. These combined results of XRD and SEM measurements suggest “surface-assisted” and “bulk” titanate nanowire coarsening in the anatase phase, similar to what happens for single nanowires. Roughly, the suggested scenario is as follows: significant shrinking in the direction perpendicular to the titanate (200) crystallographic plane occurs; at the contact points merging of aligned particles occurs via recrystallization. This titanate to anatase transformation we observed is

good agreement with previous literature (60)-(62). Increasing the heat treatment temperature to 900 °C the loss of the elongated fibers morphology was observed (Figure 2:15b). In addition, above 900 °C the newly formed rutile phase $2\theta = 27.5^\circ$ (110) appeared, coexisting with a low amount of anatase and TiO_2 (B) phase. This was also confirmed by the Raman spectroscopy measurements reported in Figure 2:15d.

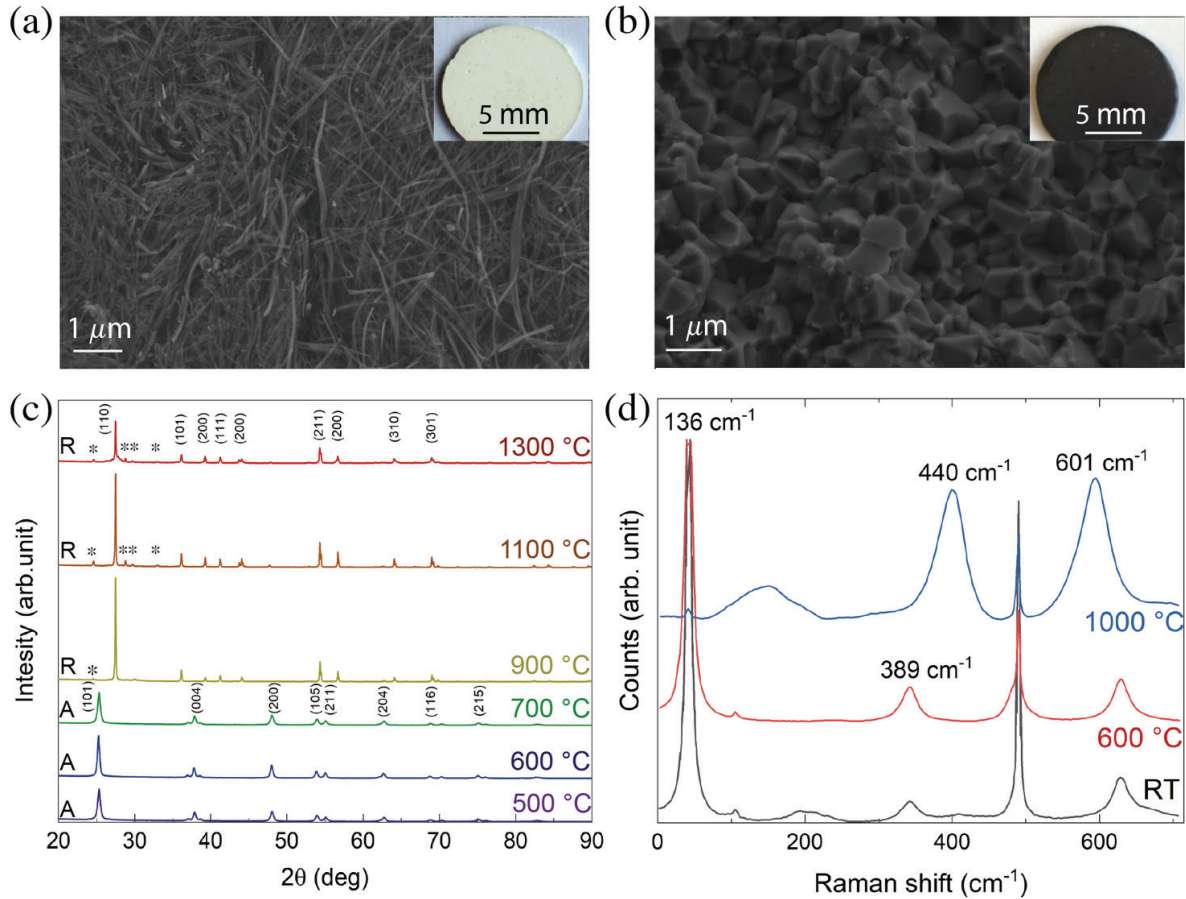


Figure 2:15 a) SEM micrograph of a TiO_2 pellet sintered at 600 °C (inset TiO_2 pellet sintered at 500 °C); b) Cross-section of a TiO_2 pellet sintered at 900 °C (inset TiO_2 pellet sintered at 900 °C); c) XRD of TiO_2 pellets sintered from 500 °C till 1300 °C. “A” is for anatase, “R” for rutile phase and “*” for TiO_2 (B) phase; d) Raman spectroscopy of a pellet at room temperature, at 600 °C and 1000 °C sintering.

Above 900 °C the nanowires assembled in the pellets were transformed into a dense, nearly isotropic crystallite based sintered body. The crystallite size increased considerably: between 500 and 700 °C the crystallite size is $\langle z \rangle = 23.5 \pm 3$ nm, while between 900 and 1300 °C we measured $\langle z \rangle = 78.3 \pm 4$ nm. This grain evolution can be attributed to the simultaneous effects of neck formation, surface diffusion, grain coarsening and pore pinning mechanism already studied in many systems both theoretically and practically (63)-(70). This 3D coarsening behavior at high temperature, above 900 °C,

is quite different from the one observed in the 2D system, where no rutile phase appeared, and the stabilization of the metastable anatase phase occurred at reasonably high temperature. We believe these marked differences are due to the interaction between titanium oxide nanowires with the SiO_2 substrate, which plays a dominant role for the 2D single nanowires and is absent in the 3D pellets or others assemblies.

Since the activation energy, surface wettability at high temperatures and topotactic effects strongly depend on the physicochemical properties as well as the crystallographic orientation of the matter, further studying the titanium oxide-support interfaces (metal, metal oxide, etc.) is necessary for the improvement of the TiO_2 based devices.

2.3.2.3 Hardness vs. porosity measurement of nanowires pellets

The micro hardness values of the 3D nanowire pellets sintered at 600 °C, having a single-phase anatase composition were measured by Vickers method (Figure 2:16). The hardness values of the sintered titania nanowires increase with decreasing porosity. For the anatase samples sintered at 600 °C the hardness of 115 HV (44% porosity) has increased to 372 HV (37% porosity) by varying the pressure. After sintering at 900 °C, we measured 941 HV (1.6% porosity), and isotropic particle shape and rutile phase was detected; this hardness value is in the range of the single crystal values 894-974 HV (71). Interestingly, comparing the hardness of anatase nanowire fiber pellets to a sample having identical porosity, but composed of nearly spherical anatase grains (commercial nanoparticles), 50% higher values of hardness were observed (Figure 2:16).

We believe that the beneficial role of elongated particle shape together with coarsening effects, such as high-quality grain boundary formation during sintering greatly contributes to these high hardness values and can open up the fabrication of nanowire reinforced ceramic sintered bodies.

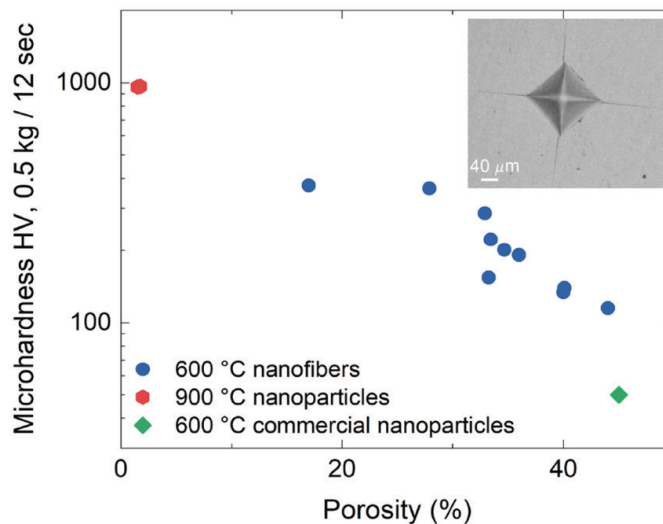


Figure 2:16 Vickers microhardness vs. porosity of 3D TiO_2 nanowire pellets sintered at 600 °C and 900 °C. Inset shows typical Vickers trace on the ceramics samples. Cracks along the diagonals evidence the typical ceramic behavior of the sintered pellets.

2.4 Conclusion

We have investigated the coarsening behavior of suspended and surface deposited single-crystalline titanate ($\text{H}_2\text{Ti}_3\text{O}_7$) nanowires and compared them to the behavior of 3D assemblies of the same composition. Two temperature-dependent geometrical transformation phase changes were identified both for single nanowire on the substrate (2D system) and for nanowire pellets (3D). During the first phase change (titanate to anatase recrystallization, above 200 °C and up to 600 °C) significant shrinking of the height of the nanowire was observed. During the second regime, at sintering temperature of 600-1000 °C an anomalous coarsening manifested as an increased surface area of the individual nanowires deposited on a surface. In addition to the strong surface effects, in the 2D system, we noticed an uncommon stabilization of the metastable anatase phase and the absence of rutile phase above 900 °C. In contrast, for 3D assembly of nanowires, from 600 °C, the classical Ostwald ripening particle coarsening was observed, accompanied by typical anatase to rutile phase transition at 900 °C.

The micro-hardness values of the sintered anatase nanowire pellets decreased with increasing porosity, showing considerably higher hardness values when compared to sintered bodies composed of nearly spherical nanoparticles.

These results will contribute to the fabrication of novel, mechanically more stable titanium oxide nanowire-based coatings and 3D functional ceramics, which is a prerequisite for safer and durable potential products.

Chapter 3 Mechanical response of individual layered titanate nanowires

This chapter contains a detailed study of the mechanical response of individual titanate nanowire: I measured their elastic modulus and computed the shear modulus, measured their flexibility, fatigue behavior and the rupture force. I have also characterized the change of Young's modulus due to the thermal transformation of titanate into anatase nanowires.

3.1 Motivations

Mechanical characterizations of different types of nanofilaments is an active field of research. It is a large interest to learn the properties of single nanowires, which influences the bulk modulus of the composite material.

The interest of these studies is mainly driven by applications. In fact, as we have seen in the previous section, titanates are the precursor structure of anatase nanowires. $\text{H}_2\text{Ti}_3\text{O}_7$ nanowires are indeed active components of a very sensitive humidity sensors (35), they serve as reinforcement fibers in composites (31), super-insulation aerogels (25), or catalyst (72). All these applications are getting credibility, since the synthesis from mg quantity by hydrothermal synthesis in autoclave, has been scaled up by an original approach to kg/month production rate (73). In all these devices it is important to assess the mechanical properties of the final system (for example in a water filter weaved from titanate nanowires) which depend on the properties of the single fibers. In addition, there is a significant interest to extend the applicability of titania thin films to flexible substrates in dye-sensitized solar cells (74)-(76), supercapacitors (77), perovskite solar cell (78)(79), gas sensors (80). Here, the preparation of porous, uniform and crack-free nanoparticle-based films is particularly challenging due to the intrinsic rigidity of sintered titania, ultimately deteriorating the performance values of lab-scale prototype devices. The effect of particle shape, replacing isotropic particles with highly anisotropic, fiber-like particles may open new avenues for the long-sought flexible devices with satisfactory electronic and mechanical performance.

3.2 Overview of experimental results on nanowires

Individual nanowire mechanical measurements are very challenging, mostly because it is very difficult to perform standard tensile or bending tests on freestanding nanoscale objects. Here, several possible approaches are illustrated.

3.2.1 Mechanical resonance excitation inside a TEM

First mechanical properties measurements have been done on individual carbon nanotubes by Treacy, Ebbesen and Gibson in 1996 (81). The measurement is based on measuring the amplitude of thermal vibration using a TEM over a large temperature range. The nanotube is fixed at one end, and the other free end is free to vibrate due to thermal excitation. This method, requiring only a TEM and a heatable stage, can be applied to other nanowires materials. Nevertheless, these measurements are subjected to large error bars between 20-60 % because of the subjective human decision when the tip starts blurring.

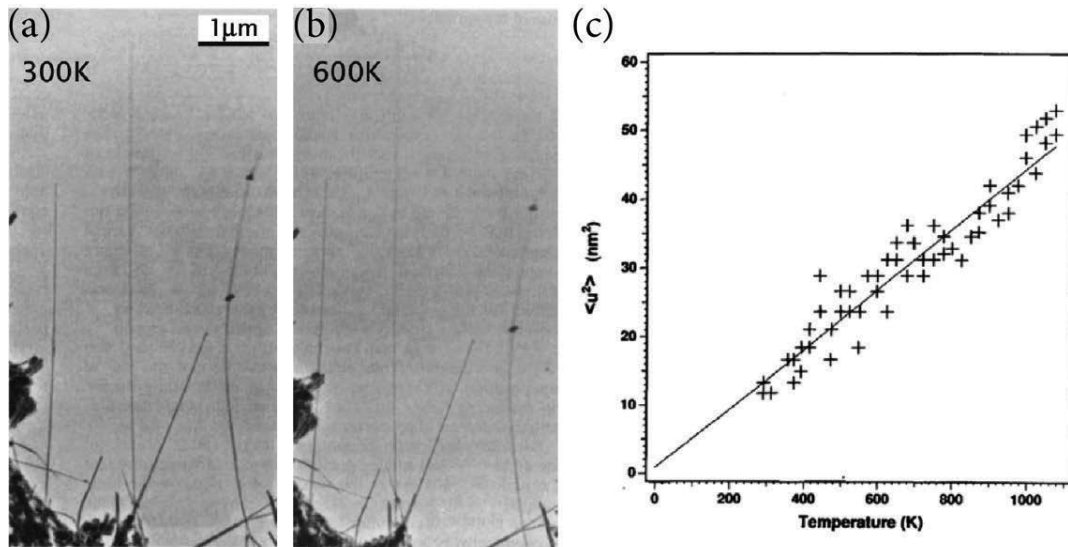


Figure 3:1 TEM images of carbon nanotube cantilever vibration a) 300 K, b) 600 K, c) mean-square vibration amplitude versus temperature. Fig. taken from Ref. (81).

Poncharal et al. (82) demonstrated another method using an alternating electric field on the carbon nanotubes. The Young modulus, E , is calculated from the resonant frequencies.

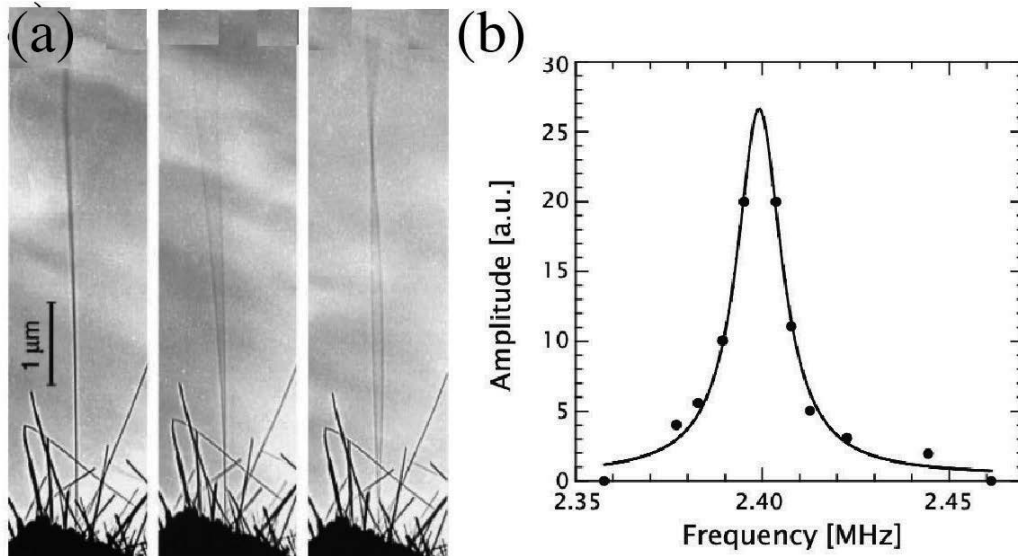


Figure 3:2 a) TEM images of excited nanotubes cantilever using an AC external field; b) amplitude versus frequency response. Fig. taken from Ref. (82).

3.2.2 Lateral deflexion by AFM

Setups based on AFM allow to apply a known force to an individual nanowire. The first AFM measurement on carbon nanotubes and SiC nanorods was reported by Wong et al. (83) in 1997. Multi-walled carbon nanotubes (MWNT) were dispersed on a flat surface of a molybdenum disulphide (MoS_2) single crystals in order to lower the friction; then this last parameter was further reduced by doing the measurement in water. As it is shown in Figure 3:3 carbon nanotubes are fixed at their extremity by arrays of square silicon oxide pads deposited using a shadow mask. The AFM cantilever is used for positioning and characterization of the nanotubes; they are deformed laterally by the AFM tip until it is passing over the nanotube and letting this last one going to the relaxation position. Young modulus has been extracted for different positions of the lateral-force distance.

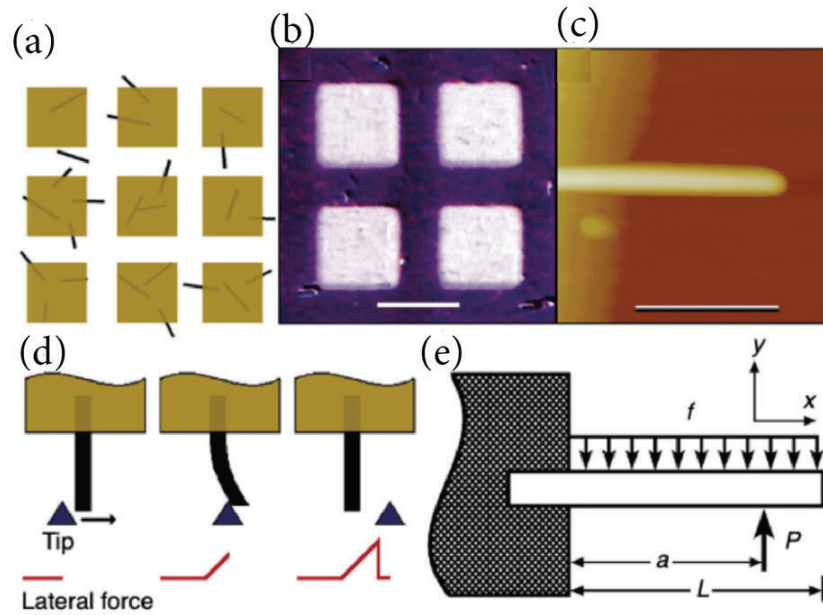


Figure 3:3 a) Carbon nanotubes fixed with SiO pads; b) optical micrograph of the substrate with carbon nanotubes; c) AFM image of SiC nanorod; d) tip moving the nanorod; e) nanorod of length L subjected to a force F . Figure taken from Ref. (83).

3.2.3 Normal deflexion by AFM

Due to demanding experiments, Salvétat and colleagues from our group at EPFL measured in 1999 the Young modulus for single-wall carbon nanotubes (SWNT) and ropes (84), MWNTs produced from various methods (85) and the shear modulus of SWNT ropes (86). The three-points bending measurement method in conjunction with the so-called “Swiss cheese method” made this experiment possible by measuring a vertical deflexion of nanotubes over holes or trenches of porous membranes. Carbon nanotubes are dispersed in ethanol and then deposited over alumina substrate. Due to van der Waals interactions, the tubes adhere to the substrate and sometimes crossing a hole. Once the good candidate found, a series of AFM images are taken increasing the load; the deflection is then obtained using the double clamped beam formula (87):

$$\delta = \frac{FL^3}{192EI} \quad \text{Equation 3:1}$$

Where F is the applied force, L is the suspended length, E the Young modulus and I the moment of inertia.

Carbon nanotubes showed exceptional mechanical properties, with a Young modulus of individual MWCT of 1 TPa.

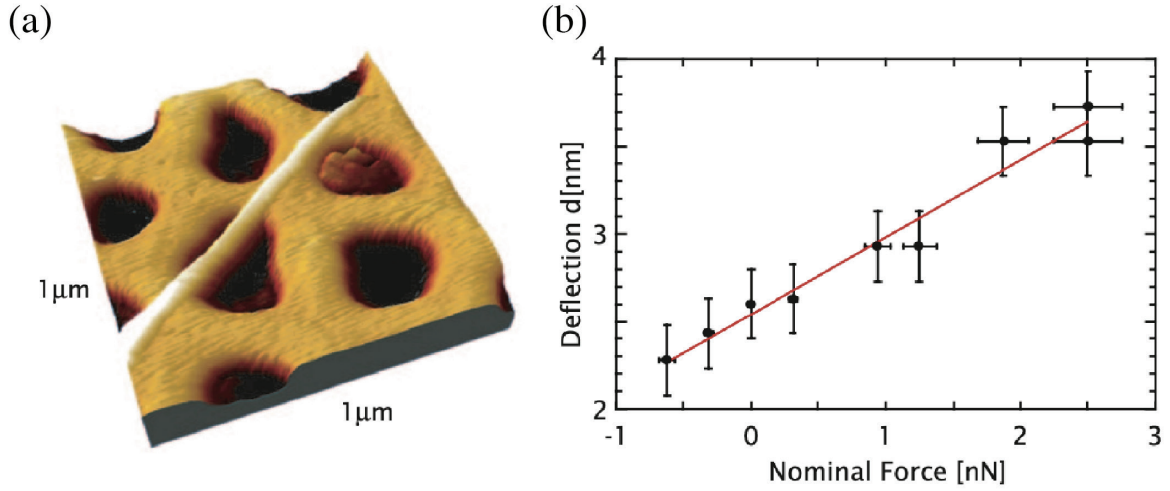


Figure 3: a) AFM image of a SWNT rope lying on a pore of the membrane; b) measured deflection δ versus applied force F . Fig. taken from Ref. (84).

In the case of a uniform beam, with negligible shear, the bending or flexural modulus (E_b) coincides with Young's modulus E . If there are subunits in the beam, which can slide on each other under the loading force, then both E and G , the shear modulus, affect E_b . In this case, the extraction of the moduli requires more careful data analysis, and the bending behavior needs to be measured for various diameters (D) and suspended lengths.

This analysis was successfully applied for single-walled carbon nanotube bundles in which the individual nanotubes are held together by weak Van der Waals forces. The obtained values were $E = 1$ TPa and $G = 5$ GPa (86). Kis et al. (88) reported that upon electron irradiation, the nanotubes got cross-linked and G tremendously increased.

The deflection is the sum of the deflections due to the bending and to the shear (87):

$$\delta = \delta_{bending} + \delta_{shearing} = \frac{FL^3}{192E_{Young}I} + f_s \frac{FL}{4GA} = \frac{FL^3}{192E_{bending}I} \quad \text{Equation 3:2}$$

Where f_s is the shape factor, A the area of the beam. $E_{bending}$ is equal to the Young modulus when shear can be neglected.

3.2.4 Literature survey on nanofilaments Young's modulus

Compared with the number of nanometer-scale materials, and in particular in nanowires shape, studies of their mechanical properties remain still limited, see Table 3:1 Nanofilaments Young's modulus summary table reported in the literature. We still don't have a global picture of the evolution of mechanical properties from bulk to nanofilaments as a function of geometrical parameters. For example, the E modulus for Si and Au nanowires is diameter independent and similar to the respective bulk modulus (89)(90). Concerning ZnO nanowires, different results are reported in the literature. Chen et al. (91) observed a size-dependent Young modulus. On the other hand Wen, Sader and Boland (92) demonstrated that Young modulus is independent of the diameter and close to the bulk value. Concerning TiO₂ anatase nanowires and in particular the precursor phase H₂Ti₃O₇ nanowires, only a few studies reported values for Young's modulus. However, it is important to point out, that according to our best knowledge, it has never been done a systematic study like the one we will illustrate in this work.

Table 3:1 Nanofilaments Young's modulus summary table reported in the literature

	<i>Nanofilament Young's modulus (GPa)</i>	<i>Bulk Young's modulus (GPa)</i>
<i>Ag</i>	80-96 (93),(94)	83
<i>Au</i>	70 (90)	78
<i>Pb</i>	67 (95)	76
<i>WS₂</i>	152 (96)	150
<i>WO₃</i>	10-110 (97)	310
<i>Si</i>	158 (89)	169
<i>LaB₆</i>	467 (98)	444
<i>Te</i>	45-85 (99)	47
<i>ZnO</i>	50-220 (91)	144
<i>ZnO</i>	140 (92)	144

3.3 Mechanical properties of titanate nanowires

3.3.1 Description of the method

3.3.1.1 Mechanical characterization method

In order to carry out mechanical characterization of NWs, we applied the three-points bending measurement method using an AFM in conjunction with the so-called “Swiss cheese method” as first proposed by J. P. Salvetat and colleagues (85)(86) for carbon nanotubes (see previous section 3.2.3). The configuration is the following: on an e-beam lithography defined holes in a silicon substrate (800 nm diameter and 400 nm depth), individual titanate NWs are deposited from an ultra-sonicated suspension via a stamping method. First, the nanowire suspension was filtered on a Teflon membrane and subsequently stamped against the microfabricated hole-containing silicon substrate. Due to the wettability differences of the substrates, the nanowires were preferentially transferred to the silicon substrate with high yield. After the evaporation of the remaining isopropanol, the NWs’ adhesion to the silicon substrate is strong so they can be treated as a double clamped beams of suspended length L (86). This strong attachment is caused by adhesion, as well as hydroxyl bond formation between the titanate and native silicon oxide layer, and is clearly demonstrated during extended AFM imaging and no displacement of the portion lying of the NW is observed.

In Figure 3:5a an optical image of nanowires deposited via a stamping method on the substrate with prefabricated micrometric holes is shown. The vast majority of the belt-shaped fibers are attached to the substrate with their largest plane, and only very few of them are attached with their smaller side-plane to the substrate. A magnification of an individual titanate nanofiber crossing a microfabricated hole is shown in Figure 3:5b. The direction of the movement of the AFM tip is indicated in the scheme. The three-point bending test were all carried out on selected nanoribbons, having the layers posed in a parallel position relative to the supporting substrate. The thickness (or height) of the nanofiber is determined on the non-suspended, clamped zone of the nanowire. The width was deduced from combined AFM and SEM micrographs (Figure 3:5c, d). The plot in Figure 3:5e shows the typical structure of our fiber with a width of about 100 nm and a height of about 30 nm. The actual cross-section dimension is smeared by the finite thickness of the AFM tip, about 40 nm in radius. Therefore, this plot gives an exact indication only of the height of the fiber.

In the double clamped beam model (87) the bending modulus (E_b) is related to the deflection δ via the moment of inertia I of the NW, to the suspended length and the loading force F according to the Equation 3:1:

$$E_b = \frac{FL^3}{192\delta I} \quad \text{Equation 3:3}$$

Where $I = bh^3/12$ for rectangular cross-section beams.

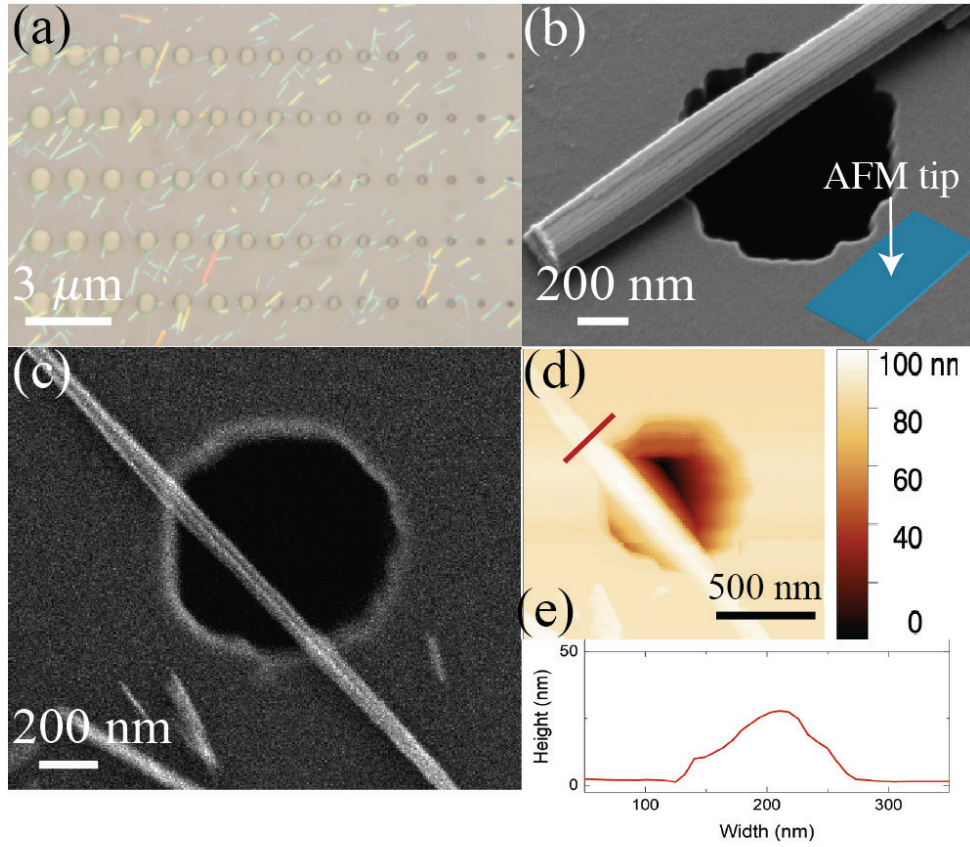


Figure 3:5 a) Optical image of nanowires deposited on the silicon substrate via a stamping method; b) SEM picture of a typical nanowire. Belt-like shape, rectangular cross-section and layered structure is observable on the micrograph acquired under tilted detector to sample conditions; c), d) SEM and AFM images of a typical nanowire crossing a hole; e) Typical cross-section profile, here an aspect ratio 1:5 (thickness to width ratio) is shown in d) and e).

The bending data were collected in the following way. After the deposition of the suspension of titanate NW on the silicon substrate containing the array of microfabricated holes and the evaporation of the solvent, the surface was imaged in a non-contact AFM mode. In cases, where NWs were bridging a hole, in a contact AFM mode, force-displacement measurements were taken (see Figure 3:6a). For each NW, before measuring the deflection on the hole, we carried out spectroscopy on the part laying on the substrate. This measurement served as a reference (black curve in Figure 3:6b). Subsequently, the same measurement was taken in the middle of the NW suspended above the hole. Both force-displacement measurements were taken with a speed of $0.3 \mu\text{m/s}$. The difference in position, i.e. of the displacement signal, for the same applied force between the two measurements, define the actual deflection δ , as plotted in the inset Figure 3:6b. The E_b is calculated from the slope of the linear regression of the $F - \delta$ graph according to Equation 3:3. The suspended length and the cross-section of the NWs varied considerably for each sample.

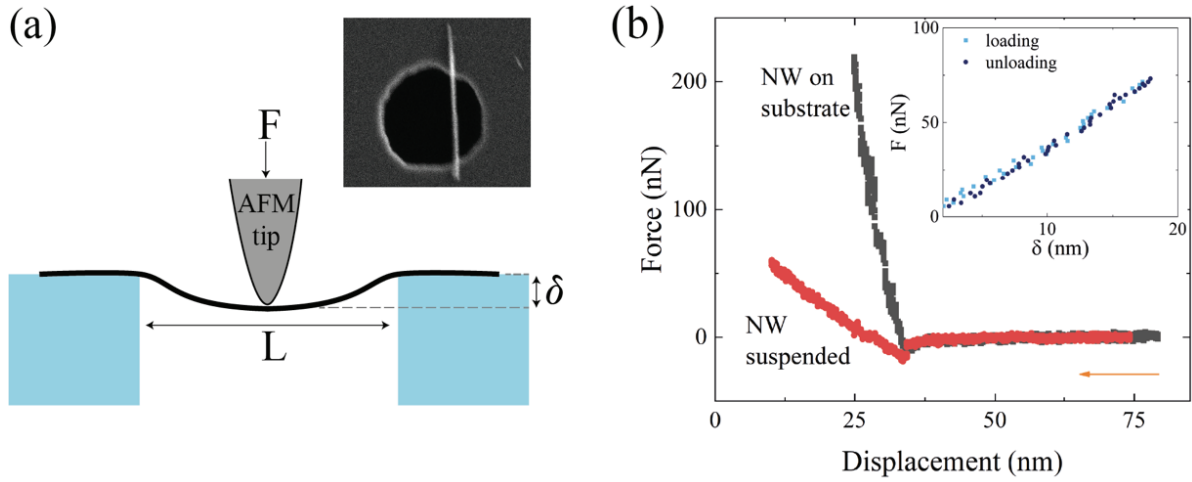


Figure 3:6 Experimental configuration for measuring the elastic response of titanate NWs. a) Sketch of the three-point bending test by AFM, indicating the major parameters for the evaluation: the inset shows an SEM image of the suspended NW over the lithographically defined hole in silicon; b) Applied force versus displacement for the three-point bending test. The black line, the reference curve, measured on the NW supported by the solid substrate; while red line is recorded in the middle of the hole, The deflection δ , used for the calculation of the bending modulus in Equation 3:3, is extracted as the difference between the red and black curves at a given force, as shown in the inset.

In the case of a uniform beam, with negligible shear, E_b coincides with the Young's modulus E . As mentioned in 3.2.3, if there are subunits, i.e. layers, in the beam, which can slide on each other under the loading force, E_b is affected also by G , the shear modulus, which can be derived with E by measuring the bending at various diameters (D) and suspended lengths (L). In this case, one can extract the two moduli (E and G) using the relation Equation 3:2 rewritten in a simpler form and the bending modulus expressed as follows (87):

$$\frac{1}{E_b} = \frac{1}{E} + \frac{10}{3} \frac{1}{G} \frac{D^2}{L^2} \quad \text{Equation 3:4}$$

3.3.1.2 Ceramic behavior of nanofibers and measurements repeatability

In order to prove the quality of the adhesion (i.e. the validity and applicability of double clamped beams model of suspended length L in our case) and repeatability of our measurements, we submitted one individual nanofiber to a loading-unloading cycle for 300-times at a force of 150 nN at the center of the NW. From Figure 3:7 one can observe the force vs. displacement ($F - \delta$) curves dur-

ing loading and unloading processes for all the 300 curves: the 300 curves overlap perfectly, indicating a full recovery from the deformation, i.e. the NW stays well inside a full elastic regime and the absence of gradual nanowire sliding, likewise testifying the validity of double clamped beams model. The lack of nanowire sliding and displacement were double-checked via comparing AFM and SEM images, prior and after the spectroscopy force measurement.

Our $\text{H}_2\text{Ti}_3\text{O}_7$ NWs show an excellent elasticity behavior, remaining in the elastic regime until the rupture point, with a slight nonlinear behavior, still inside the elastic regime, at small deformation. We noticed that during the loading and unloading process a snap-in and snap out, due to the adhesion phenomenon which is usual in AFM measurements (8). In Figure 3:7 an attractive force of about 30-50 nN, can be observed detected by AFM tip at the beginning (loading) and the end (unloading) of the measurement. As suggested by H. J. Butt et al. (100) we attributed this attraction between the tip and NWs surface to van der Waals force. Then, starting to increase the displacement, the force also increases with a slight non-linear behavior, as observed by A. Heidelberg et al. (89) for their *in situ* bending of Si NWs. Then, as shown in Figure 3:7 the curve ($F - \delta$) NW become linear until 334 nN when suddenly the force suddenly drops, showing a typical brittle fracture.

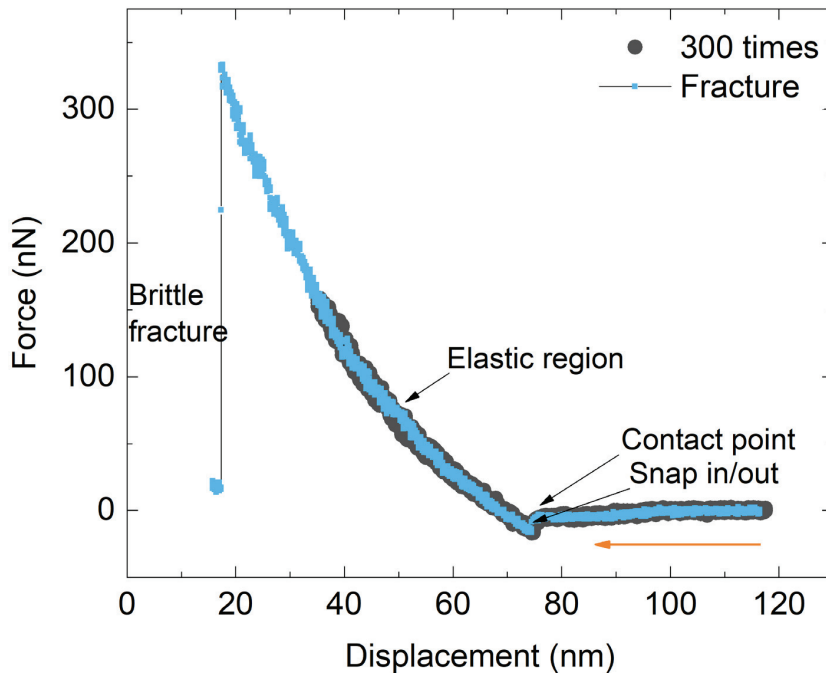


Figure 3:7 The force – release cycle has been applied 300 times, pushing till 150 nN. At 334 nN the force suddenly drops and the nanowire shows a typical brittle fracture.

3.3.2 Results: shear and Young's moduli of titanate

Figure 3:8a displays the measured E_b for a large assembly of NWs. Surprisingly, it has a strong cross-section (translated into equivalent diameter) dependence. Actually, we have considerable bending due to the weak interaction between the layers in the structure. In consequence, shear between layers plays an important role in the mechanical response of NWs. In the spirit of Equation 3:3, shear is important when: $L/R \leq 4\sqrt{(E/G)}$ (87). In our case, L/R ranges from 7.5 to 20 (evaluated by SEM and AFM measurements), so the ratio of E/G should be above 25. Using the Equation 3:3, the two moduli are deconvoluted in the following way.

The titanate NWs have a rectangular cross-section, of aspect ratio between 0.7 and 2, that can be conveniently characterized by an equivalent diameter, D_{eq} . The use of D_{eq} permits more direct comparison with the results of other authors obtained on nanowires with circular cross-section. The E_b values shown in Figure 3:8a for 25 titanates as a function of the D_{eq} , were calculated from the linear part of the $(F - \delta)$ curves, typically restricted to the 50–150 nN force range (or 25–35 nm displacement range), well below the rupture point. The reason for not going too high in loading, was to avoid damaging the NWs, which were later submitted to thermal treatment, to transform them into anatase. Making use of Equation 3:4, the plot of $1/E_b$ versus $(D/L)^2$ in the inset to Figure 3:8a allows us to extract E and G . The slope gives G while the intercept gives directly $1/E$. We obtained: $G = 1.5 \pm 0.8 \text{ GPa}$ and $E = 66.7 \pm 25 \text{ GPa}$. Despite the considerable error bar, the presence of G (of a non-zero slope) is evident in these measurements.

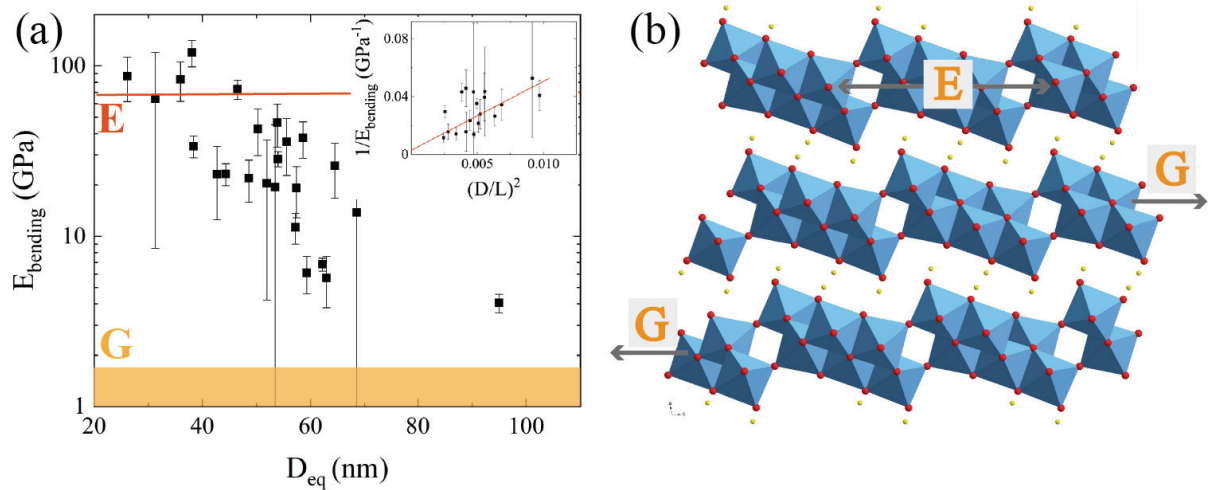


Figure 3:8 a) Measured bending modulus E_b for 25 different titanate NWs with different equivalent diameters between 26 and 95 nm; in the inset the $1/E_{bending}$ as a function of $(D/L)^2$ for determination of E and G , according to equation (2); b) Sketch of the crystal structure of titania NW, in order to illustrate the E and G moduli extracted from the left panel.

Other publications on $\text{Na}_2\text{Ti}_3\text{O}_7$ NWs, report an elastic modulus E for the NWs of 33 ± 7 GPa (101) and between 37–250 GPa (102). We believe that their low value and the large dispersion is due to a non-accounted presence of shear modulus in their measurements. To the best of our knowledge, our result is amongst the first ones to report G for layered titanate NWs. We think that this effect of diameter dependence of the flexural modulus as due to inter-layer shear found for our system in Figure 3:8b, which could be important for other layered or composite nanostructures too. The only other report on mechanical response of layered titanate nanoribbons somehow similar to ours is that of Humar et al. (103), which values are however surprising: E reaches 260 GPa, but G is in the 0.01 GPa range (hundred times smaller than ours). Actually, the very low value for G is coming probably from the shear among nanoribbons in a bundle, and not among the layer of the same ribbon, measured by us. It has to be mentioned that the E vs diameter trend shown in Figure 3:8a is similar to the one reported by Chen et al. (91) for ZnO NWs. Beyond the fact that they have covered a broader diameter range, ZnO has no layered structure, so they attribute the decrease of the modulus to binding energy balance in a core-shell model. So our data and their interpretations look to us quite unique and consistent.

3.3.2.1 Fatigue

If one is dealing with functional NWs, exposed to continual mechanical loading cycles, it is important to check the fatigue behavior of the material. A NW was submitted to a fatigue cycle with the result shown in Figure 3:9a. The red curve represents the first 600 force-release cycles up to $F = 300$ nN. The overlap of different cycles is remarkable: the NW did 600 cycles and still remained perfectly elastic, with the absence of noticeable hysteresis. The following cycles, in turquoise for the load and in blue for the unload, show a lower force than previous one (red) for the same displacement and a marked hysteresis. In the subsequent #602 loading/unloading cycle (dark green for the loading and light green for unloading) one can observe a dramatic change in the bending modulus with a drop of factor 3. We interpret these changes as a gradual rupture of the layers upon mechanical loadings composing the NWs. Presumably, the shear, translated into friction between the layers has a role in the breaking of the individual layers. In the end, the sample did not oppose any resistance to the AFM tip, the NW was ruptured. The SEM image in Figure 3:9b illustrates the end result.

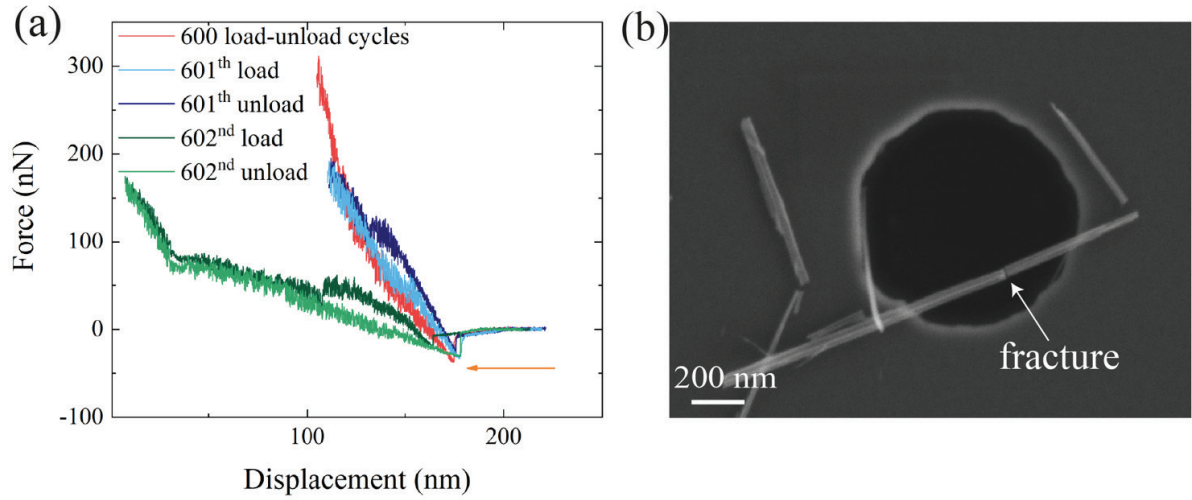


Figure 3:9 Fatigue-test of the titanate NW. a) The force – release cycle has been applied multiple times, showing the gradual decrease of the slope (stronger and stronger deflection) due to the consecutive ruptures of the titanate layers, until the final rupture of the NW; b) SEM image showing the rupture in the middle of the NW.

3.3.2.2 Superelasticity

The surprising observation of elastic behavior under repeated cycles very near to the rupture point can qualify our titanate NW as superelastic fiber in the sense that the elastic behavior is maintained until the rupture. The results of our measurements, inferring a radius of curvature of 1.5-2.5 μm in elastic regime, merits few words. It has to be mentioned that this behavior has been observed for other NWs as well (gold NWs (90), $\text{CH}_3\text{NH}_3\text{PbI}_3$ NWs (104)). However very little can be found about similar behavior on titanate NWs. In our view, this behavior that we have called “superelastic”, borrowing the definition from others different systems, is a strong indication of absence of crystalline defects, like grain boundaries and dislocations. The presence of defects, would cause a departure from the elastic behavior, and would result in a higher fragility, as pointed out by the study of anelastic behavior versus defects presence for similar ZnO NWs reported by Cheng et al. in Ref. (105). This fully elastic behavior for nanosized fibers with defects free structure is pointed out also by the study of Dai et al. (106). Therefore, we can postulate that a good number of titanate NWs have a considerable high structural quality. The origin of the superelastic behavior of layered titanate nanowires definitely deserves further, more in-depth structural and theoretical investigation.

3.3.3 Transformation of titanate into anatase

For two NW we measured the mechanical properties at intermediate temperatures, too, a 200, 400, 600 °C (Figure 3:10). Unfortunately, because of the multiple heating and cooling these fibers did not survive at 800 °C. However, we see a small change in the Young modulus with treatment temperature which justifies a direct study of the fibers after 800°C treatment skipping intermediate steps.

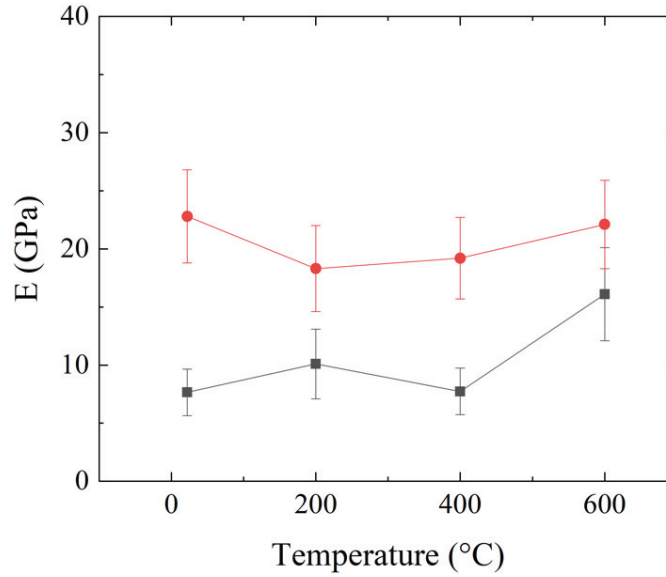


Figure 3:10 Evolution of Young's modulus of two fibers (one in red and the other in grey) as a function of temperature heat treatment.

After full characterization of the titanate NWs at room temperature, they were submitted to a thermal treatment up to 800°C in the air in order to transform them into anatase polymorph of TiO_2 . The temperature ramp rate was 20 °C/min and the samples were kept at 800 °C for one hour. One has to observe, that at such a high temperature, usually the bulk anatase transforms into rutile polymorph. But our structural investigations show, that the anatase nanowires preserve their structure even at this high temperature. A representative SEM imaging of this transformation is shown in Figure 3:11a (titanate) and Figure 3:11b (anatase). The shrinkage of the NW upon this transformation is clearly visible, since the layered texture is lost and the anatase has a uniform structure. Shrinkage due to recrystallization into the anatase phase introduces mechanical stresses in the structure, enhanced by the mismatch of NW-substrate thermal expansion coefficient and despite great care in handling, only 15 out of 25 samples survived the heat treatment.

These were exposed again to bending measurements, and the values of E_b are reported in Figure 3:11c, where for the sake of comparison, the titanate NWs are plotted, as well. One can notice that E_b is much higher for the anatase NWs, due to the absence of the shear modulus in the mechanical response, so E_b corresponds to E . It is known from indentation measurement, that for the bulk,

anatase single crystal $E = 167 \pm 15 \text{ GPa}$. The anatase NWs reach this range, although the high abundance of lower values testifies that during the recrystallization a considerable amount of defects were created, which reduce its elastic response.

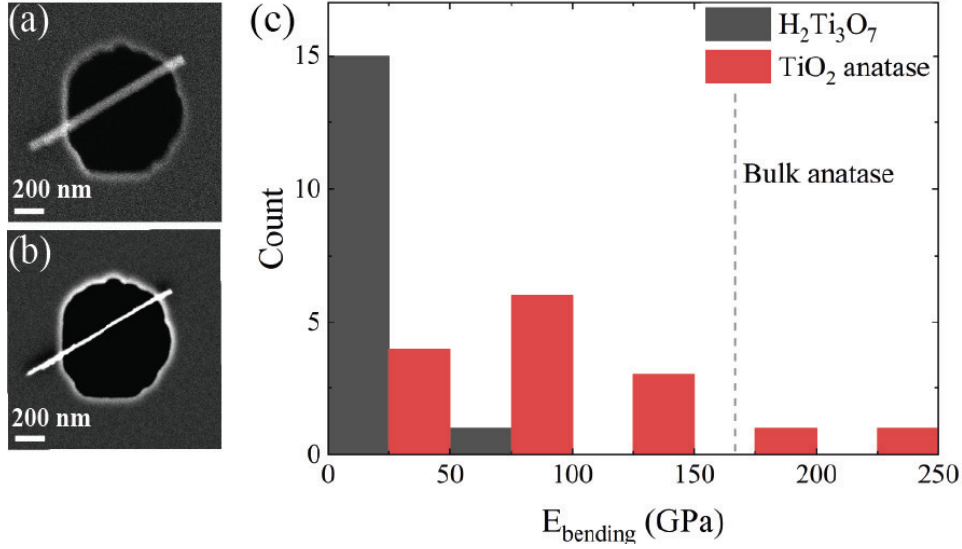


Figure 3:11 SEM image of a typical titanate NW a) Before and b) after the thermal treatment at 800°C which transforms it into the anatase phase; c) Histogram of the bending modulus (E_b) measured on 15 NWs at room temperature in the titanate and anatase forms.

3.4 Mechanical properties of titanate nanowires of $\text{H}_{2-x}\text{Cu}_x\text{Ti}_3\text{O}_7$

Motivated by the results exposed in the previous section, we wanted to investigate the trend of the bending modulus before and after the Cu ion-exchange on the NW's. The charge balance in the gallery spacing, may affect the size of this spacing, which we know that can vary, shrink or expand depending on the conditions. Any variation, shrinking or expansion may enhance or weaken the modulus. It is not known yet, so we perform the first tests below.

3.4.1 Ion-exchange process

The intercalation takes place in the titanate phase in most of the cases (107)-(109), as depicted in Figure 3:12. In order to perform the ion-exchange and study the effect of copper intercalation of the gallery spacing of NW's the following experimental procedure was used: $\text{Cu}(\text{NO}_3)_2 \times \text{H}_2\text{O}$ was the source of Cu^{2+} ions. In a typical synthesis 5 ml of $\text{H}_2\text{Ti}_3\text{O}_7$ suspension (with 100g/l trititanate nanowires dispersed in distilled water) and respective amounts of distilled water solutions of $\text{Cu}(\text{NO}_3)_2 \times \text{H}_2\text{O}$ were mixed for 1h and washed 3 times with distilled water in order to remove the excess Cu ions, which were not intercalated into the gallery spacing.

EDX analysis revealed that the typical Cu:Ti atomic ratio was 3:97. STEM image revealed that the distribution of Cu ions are fairly homogenous in the gallery spacing, Figure 3:13.

The sample for the nanomechanical measurement was prepared in the same way described in Section 3.3.1.1.

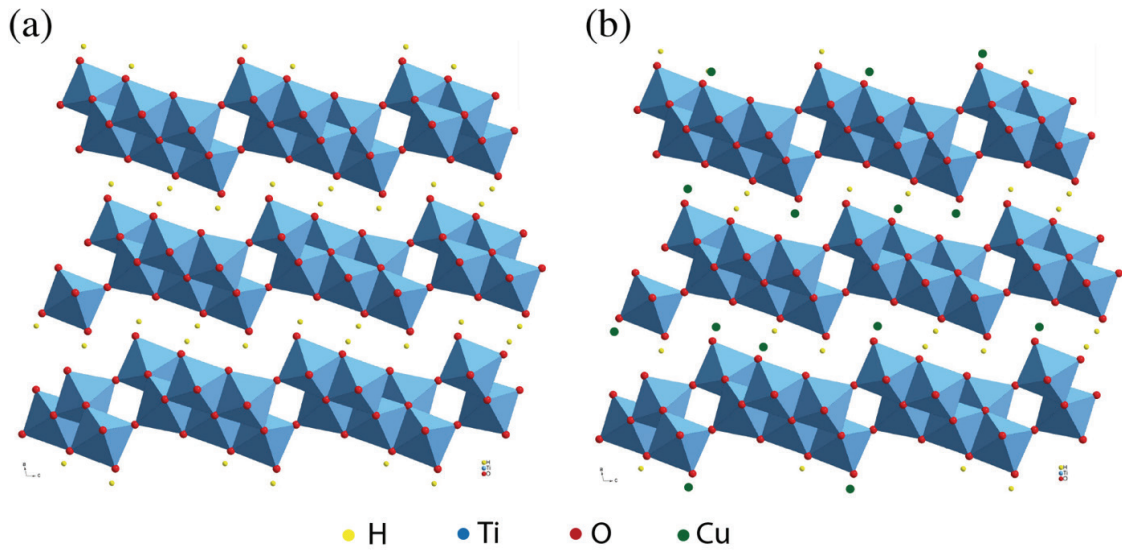


Figure 3:12 Schematic of titanate nanowires ion-exchanged with Cu^{2+} . a) Before ion-exchanged; b) after ion-exchanged.

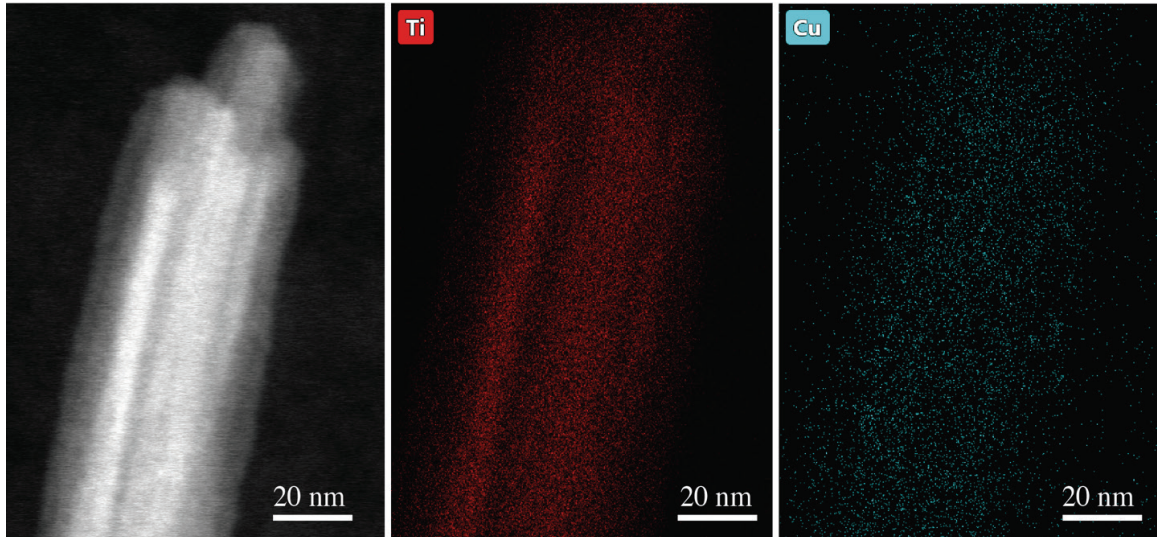


Figure 3:13 STEM/EDX images of a NW (left) showing uniform presence of titanium (center) and copper (right).

3.4.2 Results

Bending modulus results for three different NW's are exposed in Table 3:2:

Table 3:2 Nanowires bending modulus before and after Cu ion exchange.

NW's #	E_b (in GPa) before ion-exchange	E_b (in GPa) after ion-exchange
1	17.3 ± 5	12.7 ± 3
2	18.8 ± 5.2	34.2 ± 6
3	25.8 ± 4	18.9 ± 3

For fiber 1 and 3 the bending modulus decreases after ion exchange of 26%, while for fiber 2, E_b increases 45%.

These are preliminary results, hence they do not give an ultimate conclusion how the Cu ionic-exchange affects the structure of the gallery spacing and consequently the mechanical properties. More detailed work including combined TEM, XRD analysis is needed to shed light of the effect of ionic change on the E_b of this layered oxide-type compound.

3.5 Conclusions

We performed mechanical measurements on titanate NWs using an AFM-based bending test. In this layered structured material, we have given evidence of the presence of a low shear modulus of $G = 1.5 \pm 0.8$ GPa, which strongly influences the mechanical response of these NWs, despite the high E of 67 ± 25 GPa. The low G may play a role in the fatigue of the NWs. The thermal transformation and recrystallization of the titanate into anatase NWs, without shear behavior, increase E towards the bulk value.

Owing to the small radius of curvature coupled with the superior mechanical strength of titanate and anatase nanowires against repetitive bending stress conditions, these materials may serve as building blocks of future flexible energy devices, environmental decontamination systems, super thermal-insulators, sensors, catalyst supports and fiber-reinforced plastics, metals and ceramics.

Chapter 4 Metal nanoparticles interaction with TiO₂ nanowires

A striking feature of our nano-system is that the size of the supported gold nanoparticle remains quite stable even after treatment at higher temperatures. In the case of the 2D system i.e. when the NWs are laying on the surface, I verified that the nanoparticles deposited over the wide side of the nanowire, have a moderate size growth versus temperature, limited by the width of the nanobelt, which is between 30-100 nm. However, the gold nanoparticles deposited on the edge of the nanobelt show a remarkable size stabilization mechanism. I found out that even at temperatures as high as 800 °C their size doesn't change significantly, staying in the 1-10 nm range. The size stabilization is suggested to happen due to various mechanisms: intrinsic geometrical effect and strong metal support interaction (SMSI), which is enhanced by the presence of Ti³⁺ defects. SMSI is further reinforced, if the heat treatment is carried out in a reducing atmosphere rather than in standard air.

I studied also the interaction between Au NPs with TiO₂ NWs in 3D assemblies, i.e. pellets obtained by sintering powder of TiO₂ NWs and Au NPs suitably reacted and ground, with different Au concentration. We investigated the mechanical properties and the optical properties (plasmonic colour) of several pellets.

4.1 Introduction

Supported metal nanoparticles are among the most frequently used catalyst in industrial-scale heterogeneous catalysis. Figure 5:1 illustrates that there are only 12 elements that can be used as catalytic metals. The first metal nanoparticles used for catalytic applications were the 3d metals at the beginning of the 20th century with Fe for ammonia synthesis and Ni for hydrogenation of unsaturated fats, Co for gasoline and Cu for methanol synthesis. Then, in the middle of the 20th century, 4d metals like Rh, Pd and Ag were used for chemicals production. Ir and Ru found just a few applications for industrial processes. Later, at the end of 20th century Pt, a 5d metal, entered in use as a catalyst for environmental protection and fuel cell development. Osmium was excluded because of its toxicity, while gold nanoparticles have been recently discovered to have a unique catalytic activity for CO oxidation.

The high-temperature calcination, which often is part of the fabrication method, and the necessity of high-temperature regeneration during the operation, may severely degrade the performance of the device based on metal nanoparticles. One of the factors heavily affecting the perfor-

mance is the nanoparticle size growth, due to sintering processes at high temperature, which negatively effects the catalytic activity. Sintering may be induced by various intrinsic factors: nanoparticle kinetics, their size (which impacts directly on the specific surface area), their shape, their composition. In addition, the interaction strength between the nanoparticles and the support on which they are deposited is also important, therefore, the composition and structure of the support itself significantly affect the sintering process. The most important process driving sintering is the Ostwald ripening mechanism, occurring among nearby particles of different diameters, and the migration and/or coalescence processes.

The observation of strong stabilization of gold nanoparticles on titanate nanofibers is therefore very interesting phenomenon and may open the way for the application of TiO₂ nanowires charged with Au nanoparticles as a new generation of sinter-resistant metal-nanoparticles-based catalysts.

Catalytic metals: 3d → 4d → 5d

Group Valence Orbital	VIII			IB
	8	9	10	11
3d	Fe NH ₃	Co Gasoline	Ni Fats	Cu CH ₃ OH
4d	Ru Fine chemicals	Rh Fine chemicals	Pd Fine chemicals	Ag Ethylene epoxidation
5d	Os Toxic	Ir Hydrazine burning	Pt Cracking Environm.	Au
	Excl'd.	Minor	Major	Frontier

Base
 ↑
 ↓
 Noble

Figure 4:1 Catalytic metal elements. Fig. taken from Ref. (110).

4.2 Supported metal nanoparticles as catalyst

Since the 19th century, metal nanoparticles supported on various oxide supports are very important class of materials for the development of new technologies stemming from material sciences and in industrial chemical processes like heterogeneous catalysis (111)-(114). Nowadays, metal-supported nanoparticles are used in the production of chemicals, pharmaceuticals, fuel cells for clean energy technology, for hydrogen production, solar energy harvesting and also for removal of pollutants (115)-(125). One of the crucial parameters for all these applications is to keep particles nanosize even after sintering process or other thermal process. Thermally driven size growth is one factor that can limit the practical application of certain class of nanomaterials is to increase the stability of the metal nanoparticles controlling size growth (126)(127); for example, a catalyst using

gold nanoparticles whose diameter size is 3 nm or below, becomes inactive when particles exceed the size of 6 nm in diameter (128). Most of these reactions take place at relatively high temperatures, above 300 °C indeed, and the nanoparticle sintering strongly reduces the catalytic activity, thus restricting the practical applications (129)(128). Nevertheless, we have to notice that other factors, besides sintering, can lead to catalyst deactivation such as poisoning, leaching and strong metal-support interaction (SMSI) (130)(131).

Since the discovery of Haruta and Hutchings in the late 1980s (132)(133), supported gold nanoparticles, having diameters of 3-5 nm, have attracted considerable attention because of their unique catalytic activity for oxidation, hydrogenation, hydrochlorination and carbon-carbon coupling reactions (134)-(137). A Taketoshi and M. Haruta (110) studied gold nanoparticles smaller than 2 nm in diameter and less than 200 atoms and they showed that decreasing the diameter of the electronic structure also changes. When gold metal is in a bulk form, electronic levels are very close to each other, such that they form a continuous band. For a small size particle, the spacing between electronic levels is given by the following expression: $\delta = \varepsilon_F/N$, where ε_F is the Fermi level energy and N is the number of atoms in the particle (138). When the energy level space becomes larger than the thermal energy $k_B T$, the particle can lose its metallic behavior. At room temperature, the critical spacing has been calculated: $\delta = 2.5 \times 10^{-2} \text{ eV}$.

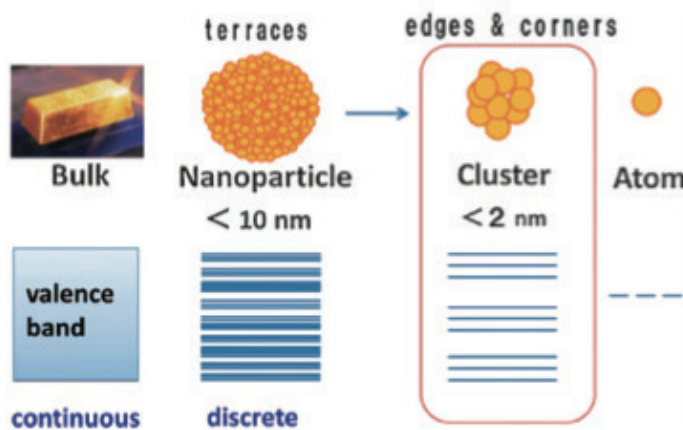


Figure 4:2 Electronic structures of gold depending on its size. Fig. taken from Ref. (110).

Gold nanoparticles have poor thermal stability compared to the platinum-group-metal (PGM) catalysts making very challenging to stabilize them in small sizes, hence restricting their practical applications (110)(119)(139)-(141). For these reasons heterogenous gold catalysis arrived late and the commercial use is so far very limited. Baker (142) by *in situ* electron microscopy did direct observations of particle mobility and he suggested that the onset of mobility happens for temperatures close to the Tammann temperature (143) ($0.5T_{melting}^{bulk}$ [K]); in fact, this temperature is the one where at-

oms on a surface become mobile and this atom's motion induces the mechanism for particle mobility. Gold nanoparticles have a relatively low melting point, around 1065 °C for bulk and 327 °C for nanoparticles with a diameter of 2 nm (144). It is known that gold nanoparticles have a size-dependence melting temperature, this last being much lower for nanoparticle than for bulk material (145)-(148). In addition, for nanoparticles of fixed size, the sintering rate increases exponentially with temperature (130) and at fixed temperatures, the sintering rate slows down with time dramatically (149).

Therefore, understanding the sintering processes of gold nanoparticles and preventing sintering is an important issue in the topic of nanocatalysis.

4.3 Sintering process

Sintering is the process where small clusters form into larger clusters. The consequence of this phenomenon in a catalytic system is (i) the loss of the active surface (150), (ii) reduction of low-coordination atoms at corners and at the edges, (iii) a variation of the electronic structure which can lead to a different reaction path (151). This process remains still not well understood. Detailed works using advanced techniques such as *in situ* microscopy and spectroscopy allow us to observe sintering in real-time at high temperatures and subnanometer resolution (129)(152)(153). Summary Table 4:1 resume the advanced techniques for study the sintering process (154). Theoretical models are used for modeling the sintering process. At the beginning of the 20th century, the model was based on the Gibbs-Thompson relation, which correlates the chemical potential with the inverse of the particle diameter. But this formula was valid mainly for large particles. Campbell et al. (150) discovered in 2002 that sintering is very dependent on the coordination of surface atoms. In the case of gold nanoparticles, the challenge is to stabilize $\{100\}$ and $\{111\}$ terminations because they tend to form thermodynamically stable cuboctahedrons. Yuan et al. explained this facet-dependent sintering behavior by density function theory calculations (155).

Moreover, as demonstrated by experiments, metal nanoparticles sintering path can depend on the size of the particle (156).

Finally, as it will be shown in our results, the sintering kinetics is dependent on the surrounding atmosphere. Supported metal nanoparticles sinter rapidly under an oxidative atmosphere, *e.g.* O₂ and air, while in vacuum or reducing and inert atmospheres *e.g.* H₂, He, Ar, the sintering process is much slower.

Table 4:1 Summary of the in-situ techniques for sintering process study. Taken from Ref. (43).

Techniques	Pros	Cons
<i>In situ</i> TEM	(i) Practical/model catalyst (ii) Dynamic changes (<i>e.g.</i> , size, shape, structure, and lattice spacing) (iii) Single-particle level with atomic resolution (iv) Convenient combination with spectroscopy (<i>e.g.</i> , EDX and EELS) (v) Environmental gaseous/liquid conditions (<i>e.g.</i> , CO, O ₂ , H ₂ O vapor, air, and liquid)	(i) Electron-beam damage (ii) Limited upper pressure of ~10 mbar
<i>In situ</i> STM	(i) Dynamic surface changes (<i>e.g.</i> , electronic structure, coordination environment, and chemical bonds) (ii) Environmental gaseous conditions (<i>e.g.</i> , CO, and O ₂) (iii) Single-particle level at atomic resolution	(i) Model catalyst only (ii) Difficult to track sintered aggregates (iii) Limited upper pressure of ~0.1 mbar
<i>In situ</i> XPS	(i) Practical/model catalyst (ii) Dynamic surface changes (<i>e.g.</i> , oxidation state, and composition) (iii) Statistical information of ensemble (iv) Environmental gaseous conditions (<i>e.g.</i> , O ₂ , and H ₂)	(i) Limited depth of the top few atomic layers (ii) Limited upper pressure of ~1 mbar
<i>In situ</i> INPS	(i) Facile operation at ambient pressure (ii) Dynamic changes in sizes in sub-second range (iii) Statistical information of ensemble (iv) Environmental gaseous conditions (<i>e.g.</i> , O ₂ , H ₂ , and NO ₂)	(i) Model catalyst (ii) Additional correlation with <i>ex situ</i> TEM analysis (iii) Complex fabrication procedure of sensor chips
Metal atom adsorption microcalorimetry	(i) High accuracy in metal-support bonding energy measurements (ii) Provides metal/support adhesion energy and metal atom chemical potential vs. particle size for ensemble average	(i) Limited to planar support (ii) Only probes ensemble average, not single particle (iii) Limited to UHV, no <i>in situ</i> observation nor environmental conditions

4.3.1 Forces inducing the sintering mechanism

Nanoparticles sintering is a complex phenomenon and catalyst nanoparticles are mainly driven by the reduction of the forces the total surface free energy of the system. When the chemical potential of a metal nanoparticles atom increases, the sintering process is accelerated, as discussed in the review paper by Y. Dai et al. (154). The formula that best describes the chemical potential in presence of adhesion energy at particle/support interface E_{adh} for a large hemispherical particle of R in radius (see Fig. 2B in (154)) is reported to be (157):

$$\mu(R) = (3\gamma_m - E_{adh})(V_m/R) \quad \text{Equation 4:1}$$

However Dai et al. (154) reports also that experimental investigations of $\mu(R)$ for metal nanoparticles of late transition metal on oxide supports, which is our case (Au on TiO₂) have shown that the chemical potential increases faster with decreasing particle size than predicted by Equation 4:1, specifically when they have an average diameter smaller than 6 nm. They report also a precise fit of the data, according to the following relation (158):

$$\mu(R_{eff}) = (3\gamma_m - E_{adh})[1 + D_0/(2R_{eff})](V_m/R_{eff}) \quad \text{Equation 4:2}$$

In any case, lowering the free energy of the nanoparticles (or μ) by increasing the adhesion force at the nanoparticle/support interface is the way to reducing the sintering phenomenon.

4.3.2 Ostwald ripening vs. migration coalescence

Sintering dynamics can be described by two mechanisms: Ostwald ripening and particle migration-coalescence.

Ostwald ripening (159) was described for the first time in 1900. Larger particles grow with interparticle transport of mobile molecular species driven by differences of surface energies. This mechanism has been proposed for metal nanoparticles sintering for nanoparticles with distinguishable diameters. Scientists have investigated and observed Ostwald ripening in various systems. For example, Challa et al. (160) observed using *in situ* TEM that small nanoparticles were immobile but exhibits remarkably sintering into larger ones via Ostwald ripening process. Numerous researches showing Ostwald ripening to be a primary mechanism (161) of sintering for different metal nanoparticles like Pd, Au, Ni, Cu under reactions condition and heating are observed *in situ* measurements (153)(156)(160)(162)-(165).

The particle migration-coalescence process involves the Brownian motion of metal nanoparticles on the support surface leading to the formation of larger particles when small particles are close to each other. Yuan et al. (155) investigated by *in situ* TEM sintering process of gold on anatase TiO₂ and they observed the small nanoparticles migration and coalescence in order to form larger particles (see Figure 4:3). Then the larger particles sintered with the small particles via Ostwald ripening process; this experiment confirmed that both different mechanisms of nanoparticles sintering act simultaneously on a sample.

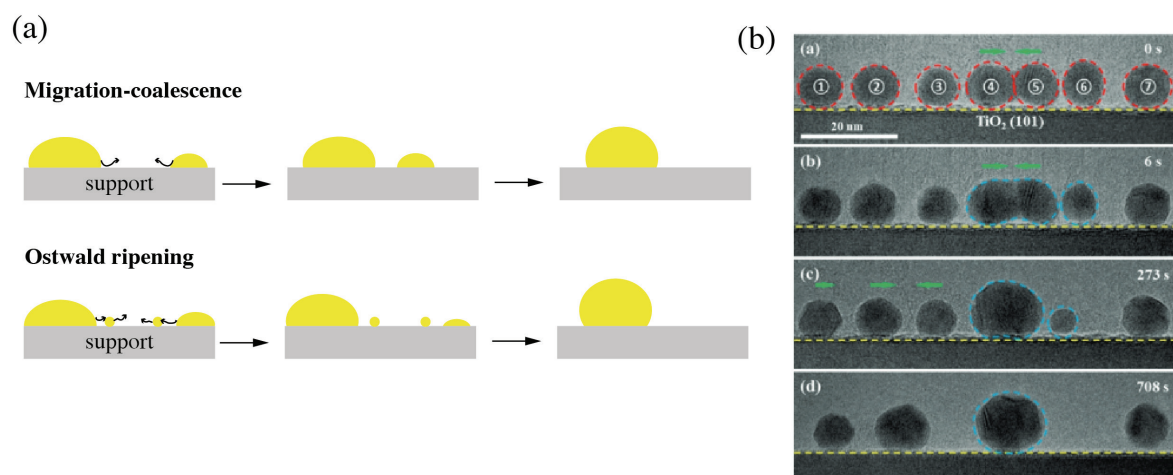


Figure 4:3 a) Sketch of migration-coalescence and Ostwald ripening sintering; b) Series of TEM images at 500 °C showing the sintering behavior process of Au NPs on a TiO₂ (101) surface. The red and blue dashed circles show the initial position of Au NPs and their change, while green arrows show the moving direction of the Au NPs. Fig. taken from Ref. (155).

To differentiate between coalescence and Ostwald ripening is not always easy, as the sintering sometimes can be due to both phenomena. However, several suggestions were put forward to differentiate these two competing phenomena. One approach is based on the particle size distribution (PSD) to identify the sintering pathway (129). Granqvist and Buhrman (166) suggested that particle coalescence gives a log-normal size distribution with a long tail for large particle sizes. By contrast, Ostwald ripening shows a distribution with a tail for small particle size. However, for particles having a diameter between 6 and 10 nm, it is difficult to use the shape of the PSD to follow the sintering pathway (149). In fact, migration-coalescence always results in a decrease of the particle number, and on the other hand at the beginning of the Ostwald ripening effect the number of particles is the same, and the smallest particles can disappear before one can detect any measurable changes in particle size for the larger particles. Comparing PSD before and after sintering could lead to large error. For this reason, as we previously mentioned, *in situ* measurements are considered to be the most reliable methods.

In literature few reviews sum up the sintering mechanisms of metal nanoparticles during a catalytic activity (129)(154)(167). Hansen et al. (129) observed catalysis at high temperatures and under working conditions, via *in situ* TEM and Monte Carlo simulations. They divided the process into three phases.

Phase I): a rapid loss of catalytic activity (surface area) is observed, due to Ostwald ripening where small particles disappeared causing a strong reduction of the catalyst activation.

Phase II): sintering process decreases because of small particles have disappeared. There is a combination of particles migration-coalescence and Ostwald ripening.

Phase III): the catalyst tries to reach an equilibrium performance but other parasitic phenomena can become important at high temperatures.

4.4 Strategies for the fabrication of a sinter-resistant metal-NPs-based catalysts

These understandings have encouraged scientists to develop several strategies in order to stabilize metal nanoparticles against Ostwald ripening effect and against migration coalescence. Different strategies, like strong metal-support interaction (SMSI) and confine metal nanoparticles in mesoporous materials or channels, are schematized in Figure 4:4.

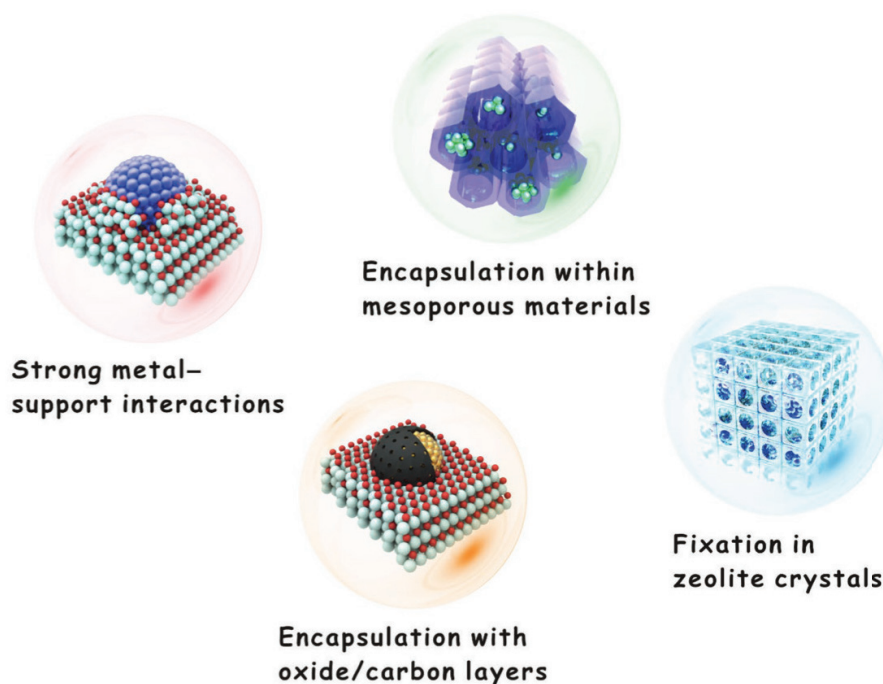


Figure 4:4 Schematics of various architecture for various preparation of metal-nanoparticles-based catalysts stabilized against sintering. Fig. taken from Ref. (168).

Of the above phenomena, we are particularly concerned about SMSI, since it has visible effects in our experiments.

SMSI has been reported for the first time in the 1970s by Tauster and Fung (169)(170) to explain the suppression of CO and H₂ adsorption between platinum (Pt) nanoparticles and TiO₂ after high-temperature treatment. Classical SMSI happens when the Pt nanoparticles are covered/encapsulated by a layer of oxide that migrated from the support. This physical oxide barrier on the surface of the nanoparticles, see Figure 4:4 top left case, prevents any sintering. Treatments in the oxidative or reductive atmosphere have extended the SMSI from the classical concept also to non-metal oxide support for example via calcination in an inert gas with transformation into oxide support of metal hydroxide or via wet chemical method at ambient temperature. A further extension of classical SMSI happens also when reducible oxide support may fix the metal nanoparticle without a physical barrier, just enhancing electronic SMSI.

The TiO₂ substrates are among the most extensively used substrates for nanoparticles, thanks to easy accessibility and their excellent reduction/oxidation properties, in particular the easy removal of lattice oxygen from the surface.

4.5 Titania as Au NP support

Metal oxides, and in particular TiO₂, have been used as support for Au nanoparticles as catalyst, as an alternative to carbon-based supports, for example for the oxidation of alcohol and alkanes as reported by Carabineiro (171). Gold has proved to be more active and selective as a catalyst than other noble metals, but small size nanoparticles is a necessary condition to achieve high reactivity. Chen et al. (172) showed promising properties as catalyst for hydroformulation of vinyl acetate of Au-Rh nanoparticles supported by titanate nanotubes and they pointed out the nanoparticles system must have high dispersion and moderate size particles (5-13 nm average size and 10-26 nm maximum size).

Marques et al. (173) reported the enhancement in high hydrogen production from aqueous glycerol by using gold nanoparticles distributed over titanate nanotubes. The photocatalyst properties are improved by the homogenous nanoparticles distribution and stabilized reduced size (9.6 nm).

The use of Au NPs exceeds the domain of chemicals production: for example, Loiseau et al. (174) have shown promising results of titanate nanotubes with engineered gold nanoparticles for improving the effectiveness of oncological radiotherapy.

In the track of all very recent studies previously reported, our research aims at stabilizing Au NPs at small sizes, thanks to the interaction with titanates nanowires, with a reliable and relatively simple method.

4.6 Investigation on 2D systems

4.6.1 Experimental methods

We have deposited, via a sputtering method, a few nanometres of a gold thin film on H₂Ti₃O₇ nanowires on a SiN substrate. Heat treatments have been carried out in a controlled atmosphere (air or hydrogen) at various temperatures up to 800 °C in order to reproduce operating conditions for various applications previously mentioned. After each temperature step, the sample has been removed from the furnace, after natural cool down for visualization by means of TEM and consequent analysis. To support our analysis one sample sintered in vacuum at 900 °C has been analysed via Electron Spin Resonance (EPR) and one special SiN substrate with grooves covered with TiO₂ on which gold NPs have been grown at 400 °C and then analysed with TEM.

4.6.2 Heat treatment in air

Following the initial thermal treatment at 200 °C in the air, the homogeneous and dense 5 nm thick gold film breaks up into separate, well defined gold nanoparticles. As a result of increasing the temperature by 200 °C each time, the morphology of the NP changes. Their size increases and their number is reduced. We have followed the evolution of the size distribution of the Au NPs laying above and nearby one H₂Ti₃O₇ NW deposited on the TEM substrate. The series of TEM images of

our sample, taken right after the Au film deposition and after each treatment step, are shown in Figure 4:5a. At first glance, we notice that particles are regrouped in two main families. One family is composed of particles showing a considerable size increase and reducing the number with increasing temperature, while the second family is composed of particles maintaining approximately constant size and number after being subjected to a high-temperature heat treatment. From the picture, one can clearly see that the NPs of the first family are laying on the SiN substrate and above the wide face, that we will call top-wall of NW (whose shape is actually more similar to a belt), see Figure 4:5b. Another feature is that most of the size increase happens following the 400 °C treatment. The second family is composed mainly of particles that stick to the narrow face of the NW, i.e. side wall of the nanobelt. For this family, we can visually detect a clear reduction of the number of particles, with a non-negligible size increase only after 800 °C treatment.

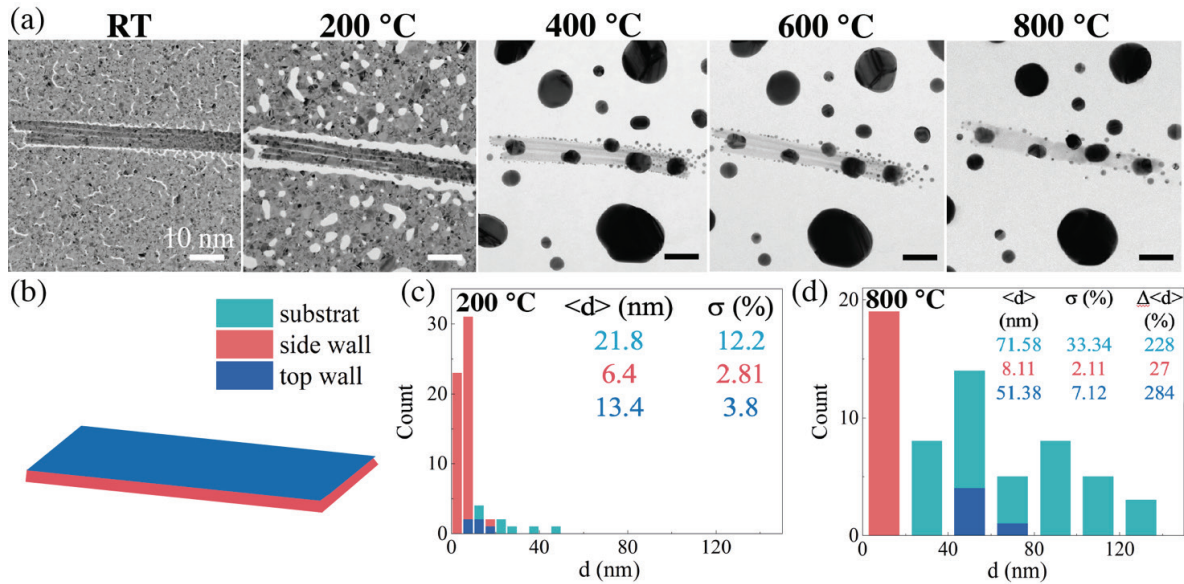


Figure 4:5 Gold NPs on a titanate NW as a function of heat treatment done in the air a) TEM pictures; b) sketch of a nanowire showing the three families; c) and d) histogram distribution of gold nanoparticles diameter and statistics at 200 °C and 800 °C, respectively.

The histograms in Figure 4:5c and d give quantitative information on the size increase versus heat treatment for the two families above discussed. Actually, in the plots, we have distinguished particles laying on the SiN substrate from particles laying directly above the H₂Ti₃O₇ nanobelt, on the top wall, therefore three families are actually presented.

Histograms in Figure 4:5c and d are complemented by the statistics reported in the table. Both particles on the substrate and the top wall more than triple their average diameters <d>. However, particles on the top wall remain noticeably smaller and more uniform than particles on the substrate.

Particles pinned on the side wall are very stable in size, and number, with a $\langle d \rangle$ increase less than 30% remaining almost all well below 10 nm.

The most surprising observation happened on the NPs anchored to the side wall, therefore we have investigated in more detail their behavior. In Figure 4:6 we indicated with red circles 10 nanoparticles on the TEM image of Figure 4:5. We have individually tracked them, measuring their size after each thermal treatment. In the graph of Figure 4:6 b the diameter *versus* temperature for each of them is plotted. Clearly, up to 400 °C, the particle size is very stable; we noticed a small increase after 600 °C treatment followed by a further size enlargement after 800 °C heat treatment. However, the size increase is very modest, less than 5% in average diameter when passing from 400 °C to 800 °C heat treatment.

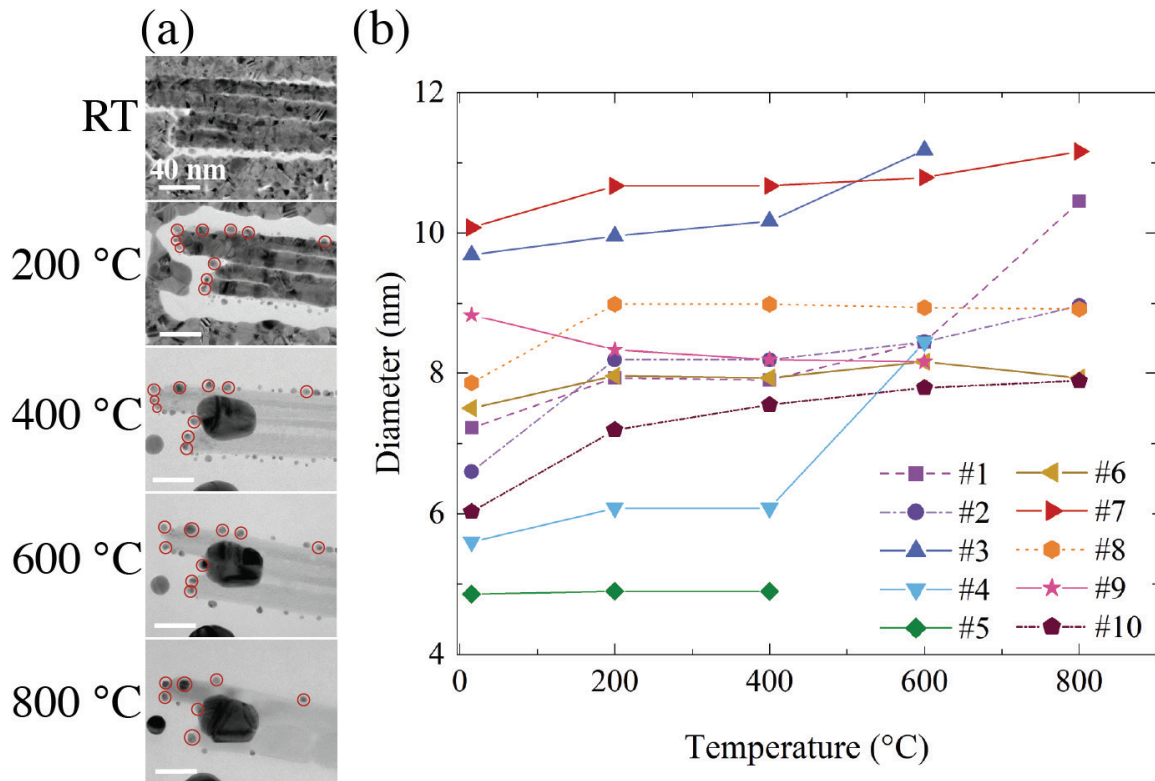


Figure 4:6 a) TEM pictures of ten gold nanoparticles laying on the side wall of the fiber as a function of temperature; b) Diameter evolution as a function of the temperature of ten gold nanoparticles circled in red in (a).

The evolution of the side wall NPs for another NW, with larger statistics $N_{200\text{ °C}} = 66$ and $N_{800\text{ °C}} = 25$ is reported in Figure 4:7. In this case, the relative size increase is larger about 50% after 600 °C and 140% after 800 °C. However, the initial diameter is very small, $\langle d \rangle = 3.67$ nm, such that the average size after the maximum temperature still remain $\langle d \rangle = 8.66$ nm, very similar to the previously discussed sample.

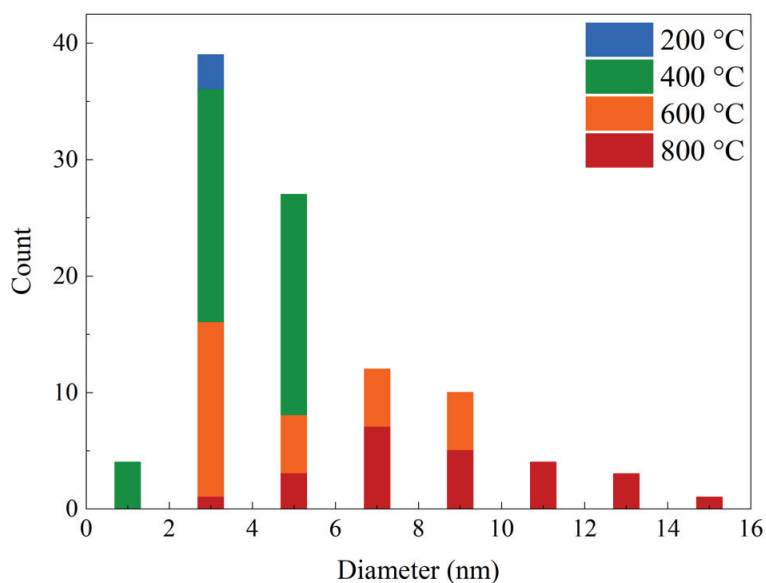


Figure 4:7 Histogram distribution of gold NPs's diameters located on the side wall of the NW after heat treatment in air.

4.6.3 Heat treatment in hydrogen atmosphere

We have investigated also the effect on particle size growth of a reducing atmosphere by carrying out thermal treatment in hydrogen gas. In Figure 4:8a we show the “time-lapse” TEM images after heat treatment under the H₂-atmosphere steps 200 °C to 800 °C.

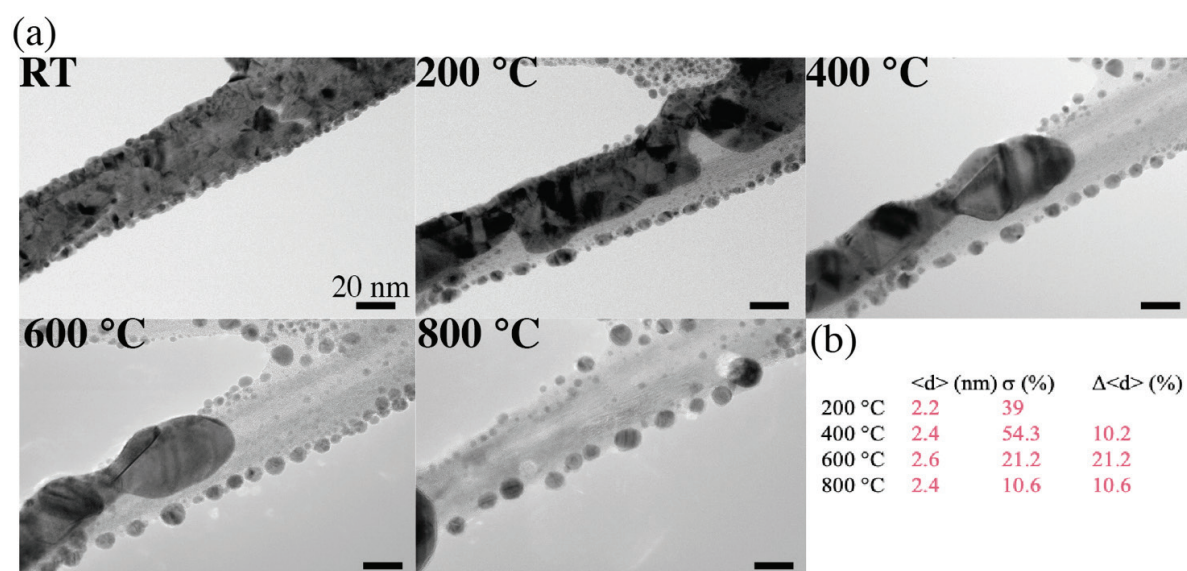


Figure 4:8 a) TEM images of gold NPs on a titanate NW as a function of heat treatment done in hydrogen; b) Gold NPs statistics for particles on the side wall of the NW.

Actually, we found out that NPs treated under hydrogen are definitively more stable than the ones treated in the air. Their size is smaller since the NPs formation at 200°C, with $\langle d \rangle = 2.2$ nm, there is no sintering observed at all. The sample population remains 150 nanoparticles, after each heat treatment, and the size increase is limited to an astonishing value of 10%, with modest increase of the size variance from 40% to 70%. All this is well depicted by the histogram in Figure 4:9. (with the same scale as the histogram of Figure 4:7 to easy comparison). Complete statistics for all 150 nanoparticles on the side wall is reported in the same Figure 4:8b, too. The average size of 2.4 nm after 800 °C is to be compared with the 8 nm average size of the NPs treated in the oxidant atmosphere. We believe that this exceptional stability at such a high temperature is due to the enhancement of the classical SMSI effect that is known as electronic SMSI as discussed in the next section.

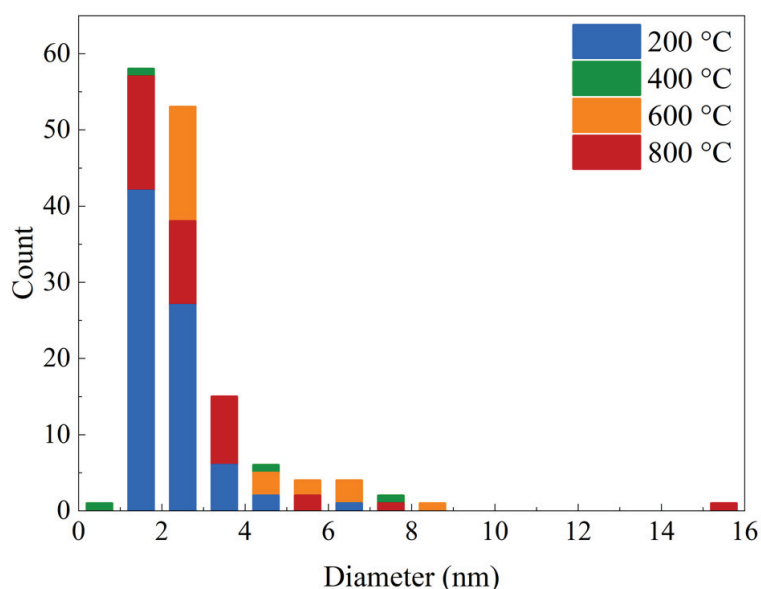


Figure 4:9 Histogram distribution of gold NPs's diameters located on the side wall of the NW after heat treatment in hydrogen.

4.6.4 Stabilization mechanism

From the fact that NP pinned on the side wall of our H₂Ti₃O₇ NW, particles are much more stable in diameter than particles laying on the top wall of the NW, we may conclude that the predominant mechanism is of geometrical nature. However, NPs remain less than 10 nm in size, despite the fact that the height of the side wall is about 20-30 nm. So we suspect that the geometrical effect is particularly strong near the corner and less effective in the middle of the top wall. To verify this hypothesis, we have tried to mimic these conditions (the shape and aspect ratio of titanate nanowires) by depositing gold on microfabricated SiN grooves covered with TiO₂. The TEM picture in Figure 4:10a, depicts that after 400 °C treatment group of small gold nanoparticles, about 10 nm in size, concentrate nearby the corner of the grooves. This experiment may confirm our hypothesis, that

geometrical effects may restrict the sintering mechanism. However, the geometrical effect is not the only one affecting our system. Temperature driven Ostwald ripening and particle coalescence are opposed also by the SMSI effect. The most important evidence is shown in Figure 4:10b, where we see a particle that is covered by the titanate layer. The presence of titanate is also confirmed by the EDS spectrum, Figure 4:11b. Also, we point out the results of an experiment in a reductive atmosphere, Figure 4:10b, a clear indication of strong classical SMSI (168). The fact that in reducing atmosphere NPs are considerably smaller also at 200 °C is probably an indication that SMSI fights Ostwald ripening at the very beginning of NP formation.

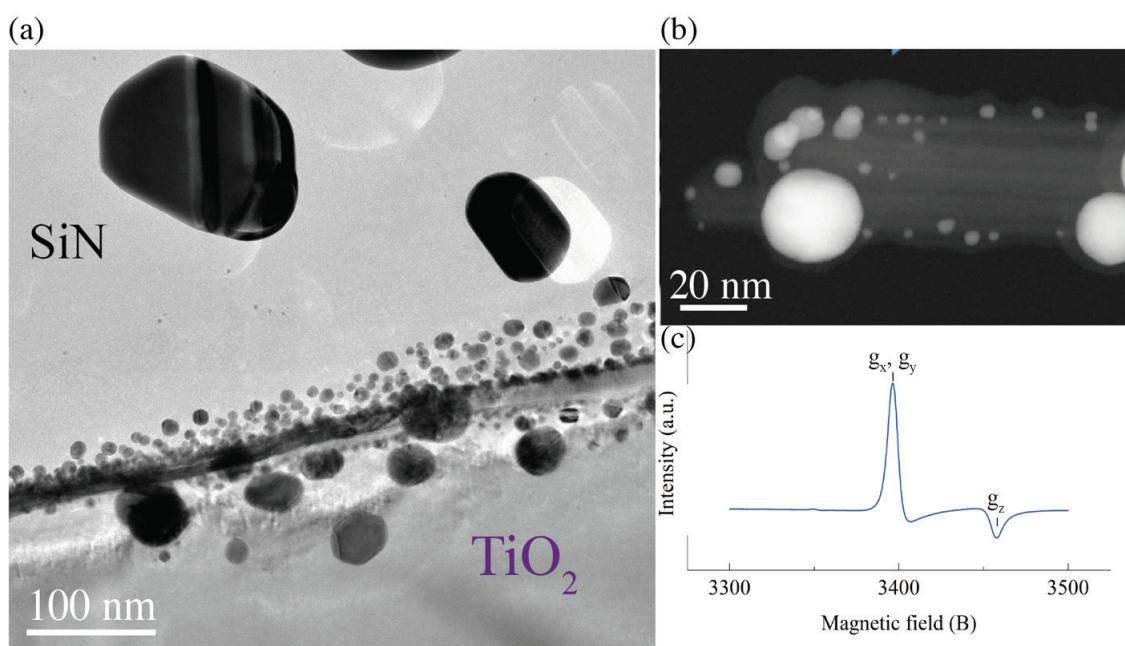


Figure 4:10 a) TEM image showing Au NPs stabilized by the edge of the TiO₂ tranche; b) TEM image of Au/TiO₂; c) EPR spectra of a sample sintered at 900 °C in vacuum.

As mentioned at the beginning of the chapter SMSI can be enhanced by a non-classical mechanism like electronic SMSI (168). Ti³⁺ are evidenced by a more sensitive measurement via electron paramagnetic resonance (ESR) on titanate and gold powder sintered in vacuum at 900 °C is reported in Figure 4:10c. Signal with $g = 1.95$ which is attributed to bulk Ti³⁺ defects (175) is present in the sample.

We believe that the presence of Ti³⁺ defects is a clear indication of the electron SMSI mechanism taking place between the gold and the fiber itself. It remains to explain why SMSI is more effective on the side wall than on the top wall of the NW. Particles on the top wall remain small than particles on the substrate however the difference in diameter is not even a factor two.

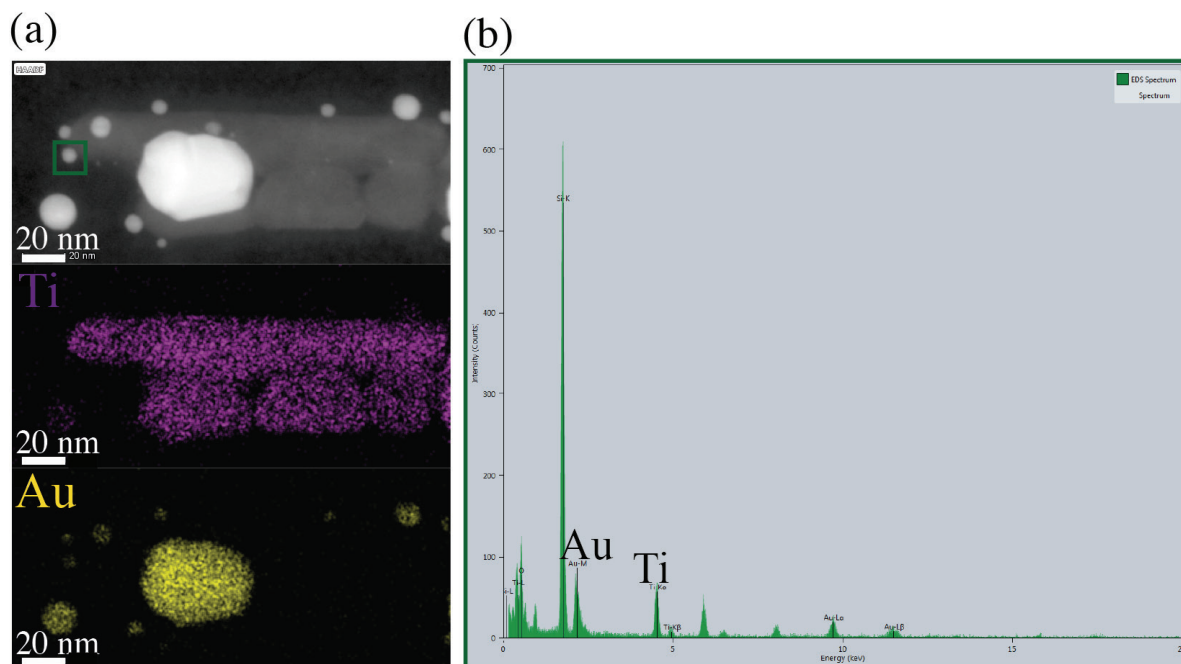


Figure 4:11 a) STEM and EDX images of Au NPs on a NW heat-treated at 800 °C in the air; b) EDX on an Au NP, showing the presence of Ti element.

The following question can be raised: is this a specific phenomenon to Au TiO₂NW system or may be a general mechanism potentially valid to other metal as well?

In order to test this, Iridium (Ir) has been deposited onto the titanate nanowires, instead of Au. Heat treatment has been done directly at 800 °C, without intermediate temperature steps in hydrogen. As can be seen in Figure 4:12b the Ir NPs, after the 800 °C, remain small, too: $\langle d \rangle = 4.5$ nm and a variance of 73%. This result confirms that Ir NPs stabilized by our NWs behave very similarly to Au NPs. These results may suggest that the side-wall stabilization may occur to large variety of metallic nanoparticles.

Nevertheless, many questions remain open and deeper and more systematic studies are needed to clearly disentangle the various factors resulting in this side-wall stabilization. However, we want to conclude on the positive note; our NWs system provides a mechanism to stabilize Au NPs against temperature-induced sintering: a large number of NPs show a diameter smaller than 10 nm even after 800 °C treatment of 30 min.

We believe that our stabilization mechanism works for all noble metals which can be very important for use in catalysis to substitute Platinum as a catalyst with more effective metals like Au and Ir.

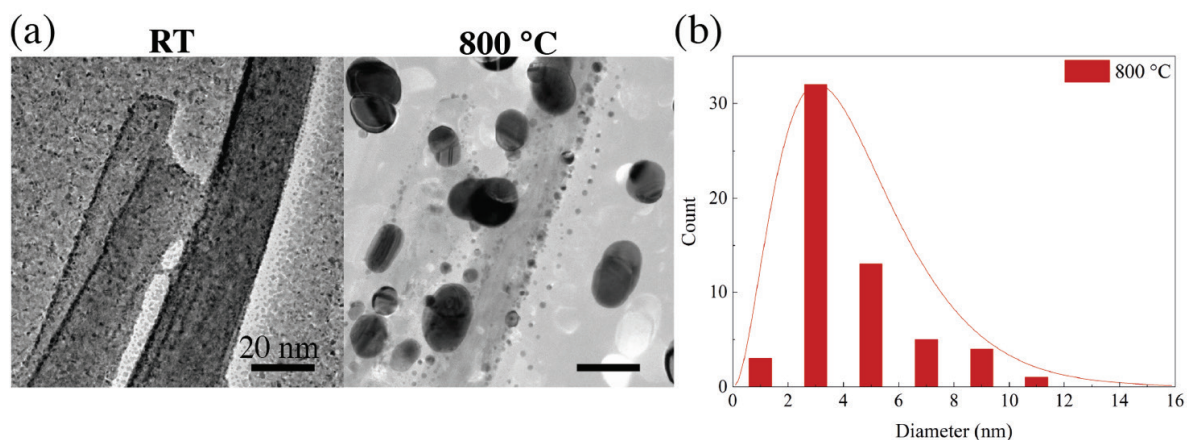


Figure 4:12 a) Iridium NPs on NWs as-deposited and after 800 °C heat treatment in hydrogen, the scale bar is the same; b) Histogram distribution of Iridium NPs's diameters located on the side wall of the NW after heat treatment in hydrogen at 800 °C.

4.7 Investigation of 3D pellets

Gold is one of the metals with the longest tradition in the jewelry and in the watch industry. However, it is mostly used in the alloyed form, because pure gold is a relatively soft metal.

In jewelry the purity of gold alloy is traditionally indicated with a carat number: 24-carat indicates pure gold, 18-carat indicates 75% gold weight content (18/24) in the alloy, and so on.

The alloying element affects the mechanical properties and the colour of the metal alloy. Among the mechanical properties which are more important for our application (watch and jewelry industry) are the resistance to deformation and scratches.

We have investigated the mechanical effect of Au NPs anchored to our TiO₂ NWs, and we have observed also the coloration effects, mainly due to plasmonic effects.

The work presented in this section 4.7 has been carried out in collaboration with a Swiss industry with the scope of exploring the applicability of our nanotechnology to cutting edge watch and jewelry industry.

4.7.1 Plasmonic effect and color tuning

Gold NPs of 10-30 nm size have a strong light absorption. Colloidal gold suspensions with spherical particles in water show an intense red color: the gold nanoparticles have strong absorption of light which peaks around 520 nm in aqueous solutions. The origin of this color of metallic nanoparticles is the localized surface plasmon resonance.

The real origin of nanoparticle coloration was unknown up to the early 20th century when theoretical studies clarify what is today known as the plasmonic effect (photon-electron coupling). The plasmon, generated from the collective oscillation of the free electrons, can be described by the classical Maxwell's equation. The plasmon is the oscillations of the metal electron gas resulting under an external oscillating electric field. Surface plasmons are waves that spread over the surface of a conductor. These plasmons can resonate with a natural frequency that is determined by particle parameters such as material shape, size, and the dielectric nature of the surrounding environment.

For NPs whose dimension is far below the wavelength of the incident electron magnetic waves, plasmons oscillate locally around the particles, therefore it is called localized surface plasma resonance. The conduction electrons in the nanoparticles move all in phase upon excitation with incidence light and polarize the particle surface (see Figure 4:13). Since the electrons are displaced from their equilibrium position, the surface charge distribution generates a restoring force on the displaced electrons, resulting in oscillation with a certain frequency, known as the plasmon resonance frequency. Of course, light with the same frequency as the plasmon resonance is absorbed.

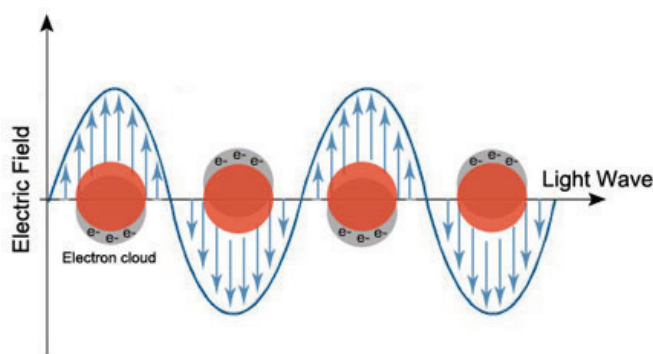


Figure 4:13 Light incident on a metal nanoparticles and their conduction band electrons start to oscillate. Image source: Wikipedia.

This collective absorption of light waves from nanoparticles gives a color to the nanoparticle system. The color can be changed, and even selected by changing the size and the spacing between NPs, which control the plasmon resonance.

In Ref. (176) is reported a study of colloidal nanoparticles of plasmonic noble metal (gold and silver) that exhibit localized surface plasmon resonance resulting in significant scattering and absorption in the visible spectrum. The plasmon excitation can be widely tuned by arranging multiple nanoparticles nearby, for instance, by forming one-dimensional (1D) chain structures, to take advantage of the interparticle near-field plasmon coupling effect. By modifying the plasticity of the polymer, they demonstrated that the plasmonic shift and colorimetric change respond to a large range of stresses. They demonstrated that a gold nanoparticles chain-polymer composite film shows a colorimetric response to mechanical forces see Figure 4:14a. This change in color is caused by a shift of the plasmonic band, which can be correlated to the applied mechanical stress.

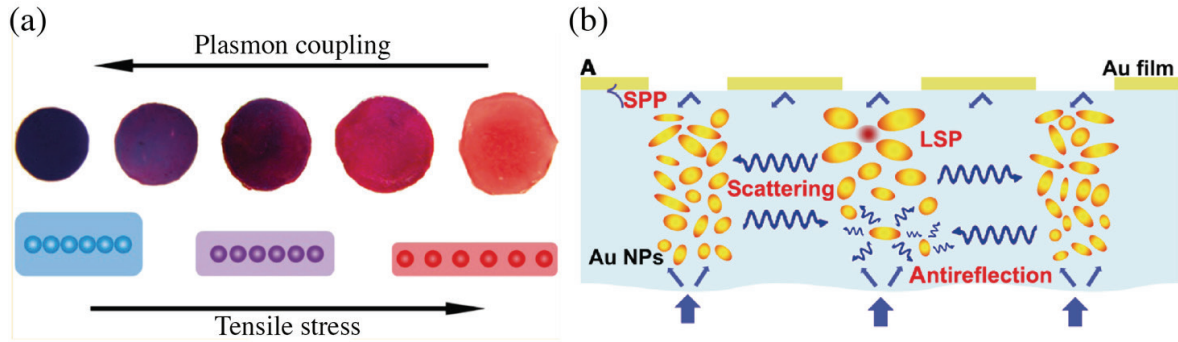


Figure 4:14 a) Illustration of film and compression test results. Adapted from Ref. (176); b) Schematic of an ideal plasmonic absorber. Fig. taken from Ref. (177).

In certain cases, a nanoporous substrate can be used to trap gold nanoparticles. If the nanoparticles have different sizes and aspect ratio the light absorption can happen in a very broadband and high efficiency. For example, it has been reported in (177) that nanoporous template (substrate) of alumina Al₂O₃ when filled with gold nanoparticles the absorbance can reach 99% in the visible and near-infrared spectra. Because of the broad size and broad distribution of nanoparticles, various types of surface plasmon phenomena play a role (localized surface plasmon resonance and surface plasmon polariton) in increasing the coupling between light and particles giving rise to this broadband, very efficient absorption.

This is the reason why under certain conditions distribution of gold nanoparticles in a substrate can be seen as completely black color, see Figure 4:14b.

We have dispersed gold NPs in our TiO₂ system and from this we have fabricated pellets of different carats and we have demonstrated color control capability.

4.7.2 Experimental

4.7.2.1 Preparation of TiO₂-Au synthesis

The TiO₂ NWs preparation has been already described in section 2.2.3.1. Here we focus on the gold-TiO₂ synthesis.

We started from 24-carat pure gold whose SEM image is shown in Figure 4:15a. According to the final target carat, the concentration balance of TiO₂ and Au is determined, according to Table 4:2. The synthesis happens in a reactor charged with 100 l of distilled water at 85 °C. A solution with TiO₂ NWs well blended using ultrasounds is added to the distilled water and then gold in the ionic phase is added, too. Finally, a surfactant is added for controlling the size of the nanoparticles,

see Figure 4:15d. After about 6 hours the material has sedimented and we can proceed with filtration and cleaning stages followed by grinding step to produce the powder with micron-size grains.

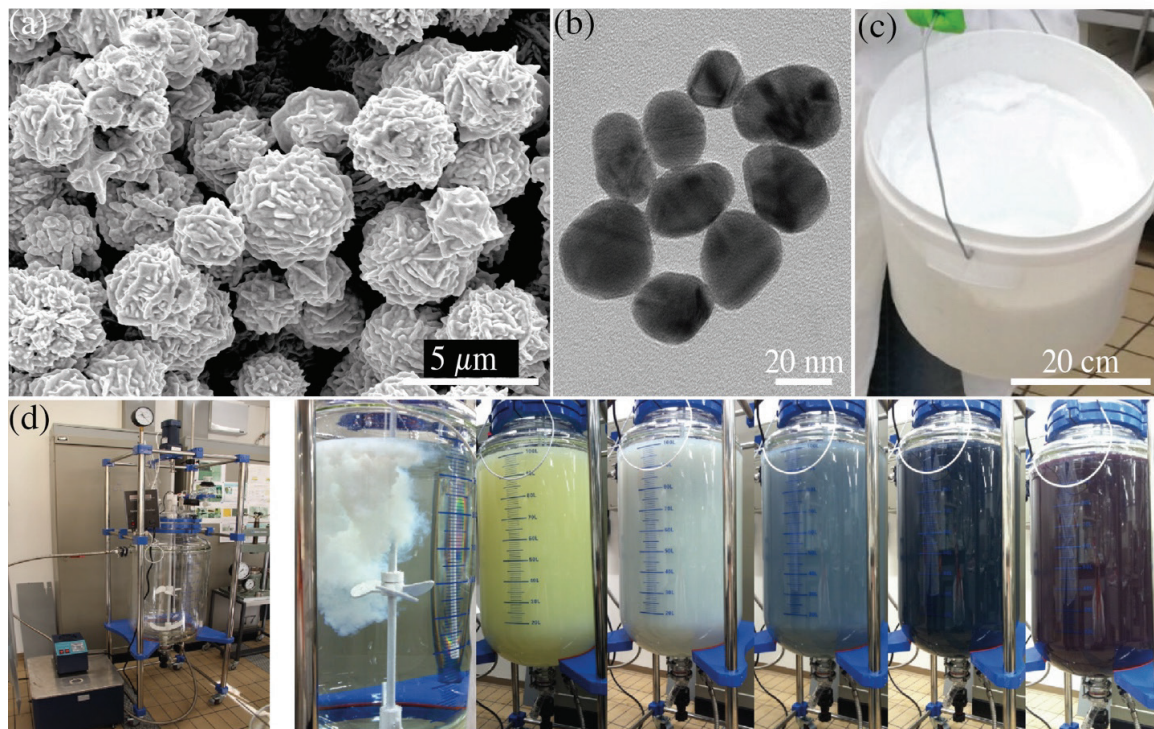


Figure 4:15 a) SEM image of 24-carat gold grains; b) TEM picture of gold nanoparticles, their average diameter size is 30 nm; c) Photograph of a batch of 200 g of TiO₂ NWs; d) Picture of the reactor for gold-titanium dioxide synthesis in our nano laboratory. Different steps of the synthesis are shown as a function of time.

We have chosen to study Au/TiO₂ composites having various metal to oxide ratios: in particular 18, 12 and 1.5-carats.

In Figure 4:16a and b TEM and SEM image, respectively, of Au/TiO₂ composite, depicts a fresh sample composite after the liquid phase preparation.

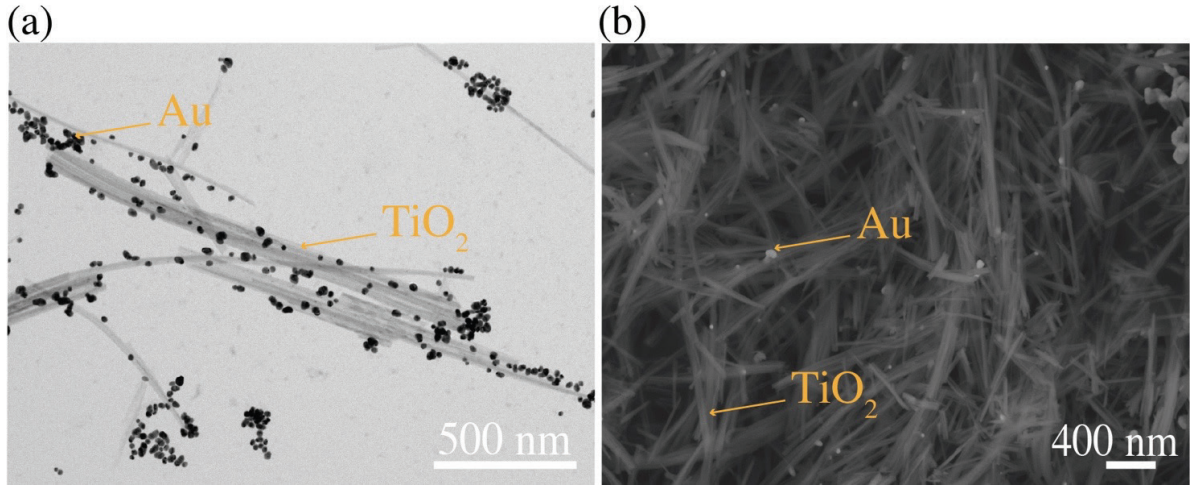


Figure 4:16 Gold/titania composite with 75w%Au. a) TEM image of the nanoparticles after the liquid phase preparation; b) SEM image of the as-synthesized powder before heat treatment.

From TEM and XRD analysis, we know the gold NPs average size, about 30 ± 3 nm (Figure 4:15b), therefore we can calculate the average spacing of the gold NPs for the various concentrations. The nominal distance between Au NPs for the three carats that we have studied is shown in Figure 4:17. In a few special cases we have treated the TiO₂ NWs solution with ball planetary milling: in this way, the nanofibers lost their monodimensional characteristic.

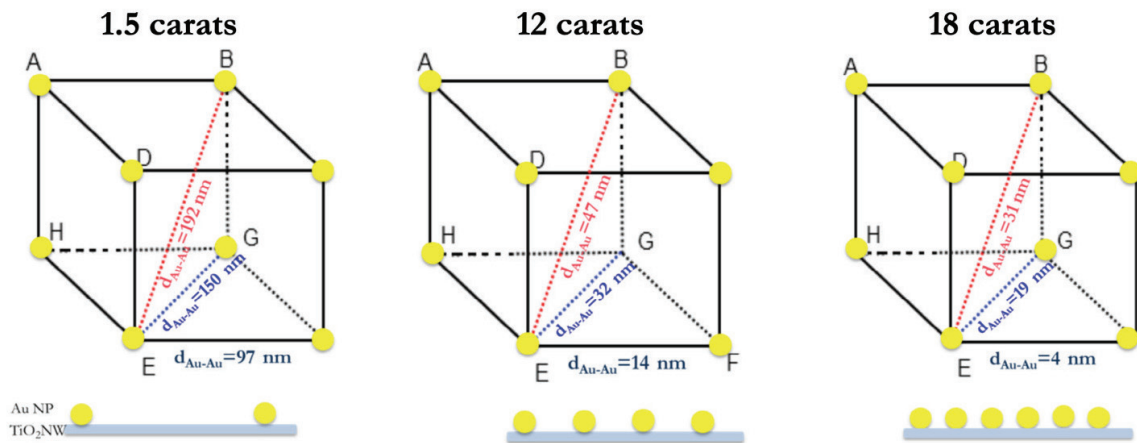


Figure 4:17 Au-Au theoretical distance over a TiO₂ NW according to the carat.

Table 4:2 Summary of Au and TiO₂ weight percentage and their theoretical density according to the carat.

<i>Carat</i>	<i>Au wt%</i>	<i>TiO₂ wt%</i>	ρ_{th} (g/cm ³)
18	75	25	9.7
12	50	50	6.5
1	4.2	95.8	4.0

4.7.2.2 Preparation of the 3D pellets

From the powder, see the picture in Figure 4:18, we have prepared a variety of pellets, using the instruments described in section 1.2. By applying uniaxial press we obtained pellets of 12 mm in diameter and thickness in the range of 0.7 - 1.5 mm. Pellets produced with SPS have a diameter of 20 mm and thickness of in the range of 1.3 - 2mm. All samples are eventually dry polished by hands with various grades of SiC papers.

Temperature and pressure are optimized to maintain NPs spacing, especially after sintering, avoiding gold nanoparticle aggregations. This is very challenging because gold is ductile and is very prone to Ostwald ripening and coalescence under high temperature and pressure.

Figure 4:18 Photograph of Au-TiO₂ ready to be sintered. From left to right: 18, 12 and 1.5 carats, respectively.

4.7.3 18-carats

We start discussing the 18-carat samples since it is the standard alloy for the jewelry and watch industry. Out of the many samples prepared, we discuss results on the two samples whose characteristics are reported in Table 4:3. These samples are among the best performing in terms of colorimetry, porosity and microhardness.

Table 4:3 Summary table of 18-carat samples

Sample #	Sintering method	$T_{\text{sintering}}$ (°C)	Mass (g)	Thickness (mm)	Diameter (mm)	ρ (g cm ³)	Porosity (%)	Micro hardness (HV) ¹
B2022	SPS	900	4.06	1.3	20	8.76	0.1	320±8
41	HUP	130	1	0.8	12	7.75	0	253±6.7

4.7.3.1 Sample B2022

This sample has been produced by SPS according to the cycle depicted in Figure 4:19. This sample has shown almost no porosity and good hardness value, in line with expectations for the watch industry.

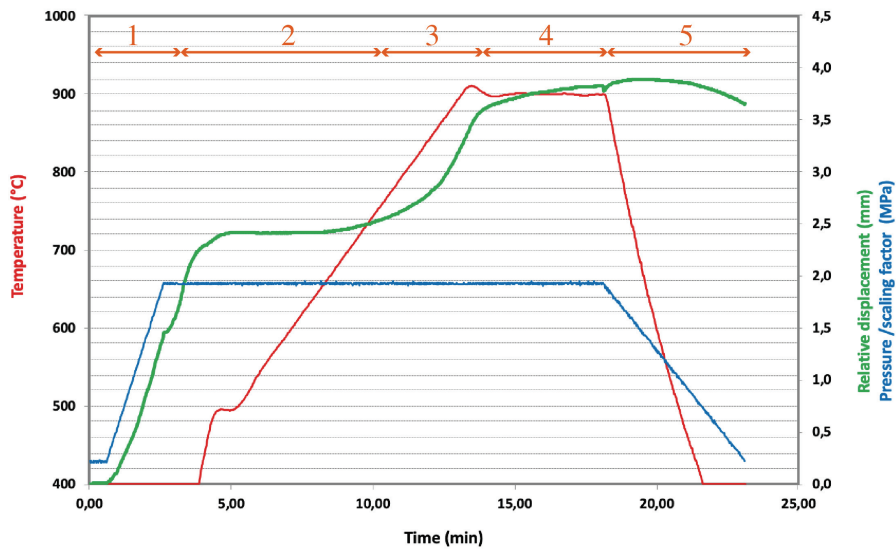


Figure 4:19 SPS cycle for 75wt%Au B2022 sample. We can observe 5 different zones. 1: 50 MPa pressure is initially applied to the sample at low temperature (< 400°C), with a 2.4 mm displacement of the pistons. 2: The temperature rises steadily up to 700 °C at a constant piston position. 3: Above 700 °C the pistons start to move again to keep constant pressure, strongly densifying the pellet (total movement of 1.2 mm). In this temperature range occurs the phase transformation from anatase to rutile. 4: Temperature ramp stops at around 900 °C with 5 min temperature plateau in which the pistons make a further small 0.3 mm displacement due to creep. 5: Finally temperature is dropped and pressure is released in about 5 min.

¹ Micro hardness Vickers : F= 0.5 kg, t=12 sec.

After polishing, the sample appears in an interesting “kaki” tone, an unconventional gold color, see Figure 4:20a inset. In order to investigate the microstructure by TEM, a 100 nm sample lamella has been cut using a focus ion beam (FIB). The microstructure is visible in Figure 4:20a and the magnification in b and c. From the TEM image analysis, we observed that the Au grain size ranges between 100 and 600 nm, while for TiO₂ grain size is around 200 nm.

In Figure 4:20b one can first observe that gold domains are polycrystalline containing grain boundaries. Also, dislocations are visible inside the gold grain, due to FIB cut, with a morphology typical for an FCC structure, while in Figure 4:20c Moiré fringes are well visible. The same lamella was imaged in the bright field see Figure 4:20d by a means of a TEM JEOL 2200FS for nano diffraction mapping². The image has been analyzed for grain orientation of Au and TiO₂, as shown in e and f: the random orientation shows the lack of preferential texture.

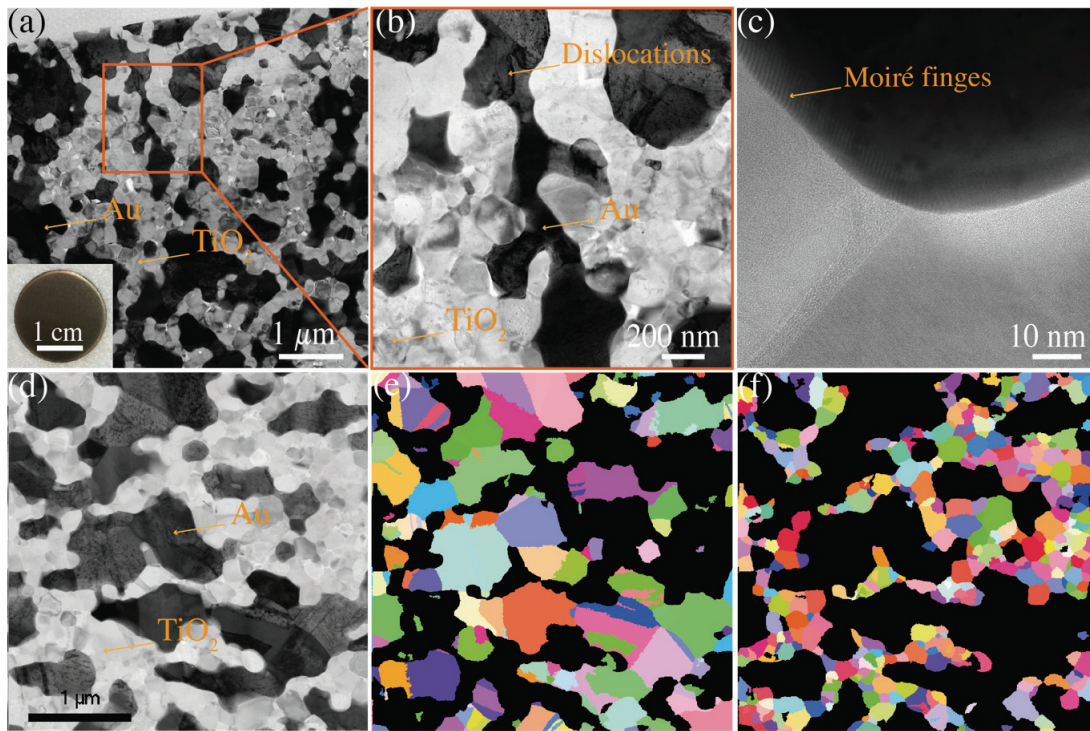


Figure 4:20 Au/TiO₂ composite with 75wt%Au. a) TEM micrograph of a lamella cut by FIB out of the pellet after sintering. The pellet is shown in the inset; b) Magnification of the yellow square of the image in a); c) HR-TEM image of a lamella detail, showing Au and TiO₂ crystallization and Moiré fringes at the interface between the gold and titanium dioxide; d) Bright-field TEM image of the lamella; e) and f) Gold and TiO₂ grains orientation, respectively, of Figure d). Each color corresponds to a particular orientation (same color code for gold and TiO₂).

² The Automated crystal orientation mapping (ACOM-TEM) with the NanoMegas ASTAR system, uses a TEM to collect and index nanodiffraction patterns over a scanned area. NanoMegas ASTAR system is mounted on JEOL TEM 2200FS having a spatial resolution of 5 nm and a probe diameter of 2 nm. Measurements done by courtesy of Dr. T. LaGrange, CIME.

From XRD measurements TiO₂ is in the rutile phase with a low content of anatase phase like it has been also shown for the pristine TiO₂ sample sintered at the same conditions in section 2.3.2.2. Crystallite sizes have been calculated : $\langle z \rangle_{gold} = 45 \text{ nm}$, $\langle z \rangle_{rutile} = 62 \text{ nm}$ and $\langle z \rangle_{anatase} = 49 \text{ nm}$.

Finally, we have carried out micro and nanoindentation. In Figure 4:21a it is shown a micro Vickers indentation; once the pyramidal tip is removed from the sample, the surface shows a strong plastic deformation with no crack. Then we proceed with the grid of nano hardness measurements. A matrix 4×4 of nanoindentations whose results are reported in Figure 4:21b, has been carried out on the sample surface. The loads curves do not perfectly overlap, a signature of the sample inhomogeneity, mostly because the tip is touching a soft gold grain and other times a TiO₂ grain. In all cases we notice a plastic behavior, with a large permanent deformation even at loads well below 100 mN, showing a predominance of the very soft gold properties over the ceramic TiO₂ behavior.

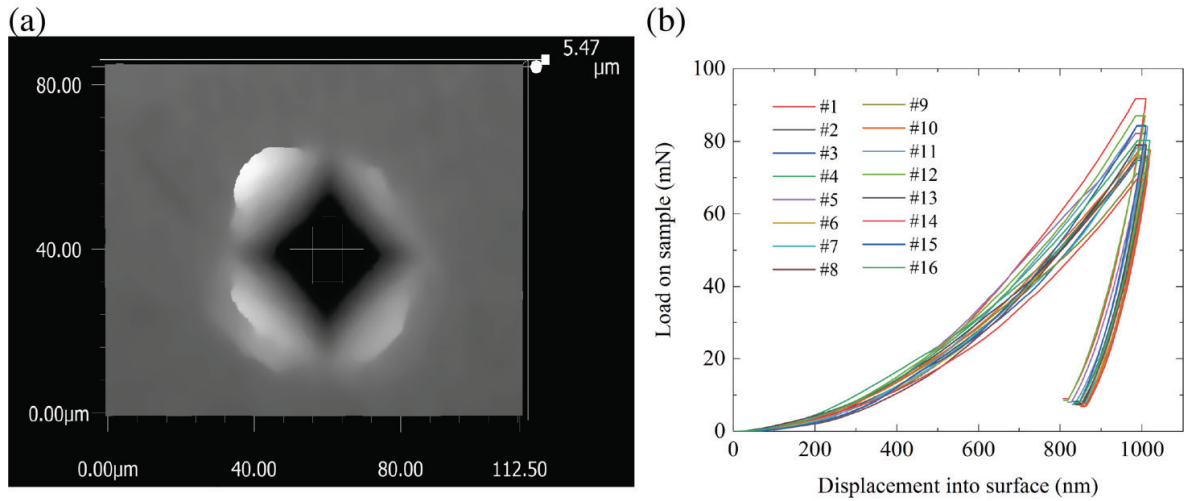


Figure 4:21 a) Optical microscope picture of indentation for Vickers hardness measurements, showing the plastic deformation after the measurement campaign; b) 16 nanoindentation measurement cycles, on different positions in the sample, showing the load force on the sample as a function of the displacement into the surface on different positions.

4.7.3.2 Sample 41

The sample shown in Figure 4:22, has been manufactured with the HIP method at a fairly low temperature of 130 °C. Despite this unusually low sintering temperature, the sample has shown very good mechanical characteristics, beyond our expectations, especially for the hardness. The characteristics of this sample are reported in Table 4:3. Another markable feature of this sample is the predominant purple coloration, a really unconventional gold.

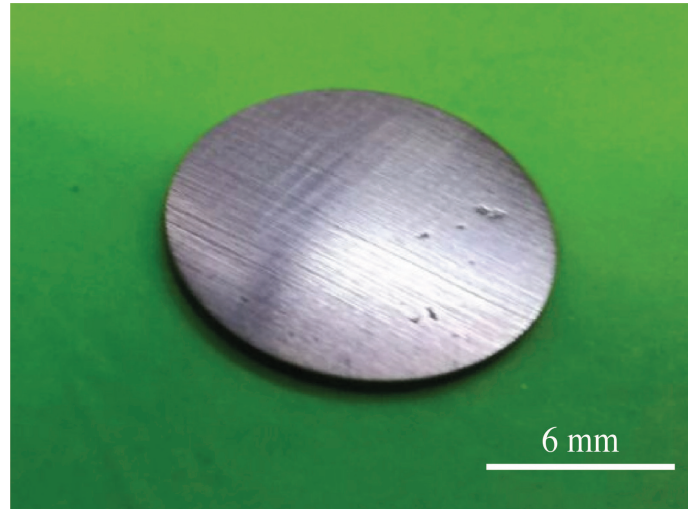


Figure 4:22 Sample 41 sintered at 130 °C.

4.7.4 12-carat

Samples with intermediate gold content, i.e. 50wt% Au which is the minimum usually considered in jewelry, have been produced. In Table 4:4 we report the characteristics of two among the most interesting samples.

We can note that the SPS processed B2133 sample has an unusually large diameter, 40 mm. These types of samples were manufactured to understand the scale-up suitability of our process and having in mind a specific proprietary application. What we can say here is that the microstructure and crystallite sizes of this sample are pretty much the same as a sample produced with the same process and with standard 12 mm diameter. It is particularly interesting the very low porosity and the good hardness value of 350 HV.

Table 4:4 Summary table of 12-carat samples

<i>Sample</i>	<i>Sintering method</i>	<i>T_{sintering}</i> (°C)	<i>Mass</i> (g)	<i>Thickness</i> (mm)	<i>Diameter</i> (mm)	<i>ρ</i> (g cm ³)	<i>Porosity</i> (%)	<i>Micro hardness (HV)³</i>
B2133	SPS	900	15	1.75	40	6.63	0.1	350±10
37 ⁴	HUP	250	0.9	1.5	12	6.61	7.8	320±7

³ Micro hardness Vickers : F= 0.5 kg, t=12 sec.

⁴ TiO₂ NWs has been treated with ball planetary milling before being loaded in the reactor.

Sample 37 has been manufactured with a special pre-process: titanate NWs has been crushed in a ball planetary milling as mentioned at the end of section 4.7.2.1. The scope was to decrease the porosity and increase the sample hardness. Actually, looking at Table 4:4, we see that the porosity is not as good as expected, however, the microhardness measurement gave 320 HV which is a fairly good value for a sample produced with HIP at relatively low sintering temperature. In Figure 4:23a we can observe a TEM image of a 100 nm thick lamella cut out from the pellet using FIB. The crystallite size from XRD has been evaluated $\langle z \rangle_{\text{gold}} = 36.5 \text{ nm}$ and $\langle z \rangle_{\text{anatase}} = 24.6 \text{ nm}$. In this sample, we carried out a mechanical machining test. The same special shape illustrated in Figure 4:23b were obtained by laser cut from sample 37. The mechanical workability has been found very good: various shapes are obtained with good accuracy and no cracks were detected at the edges.

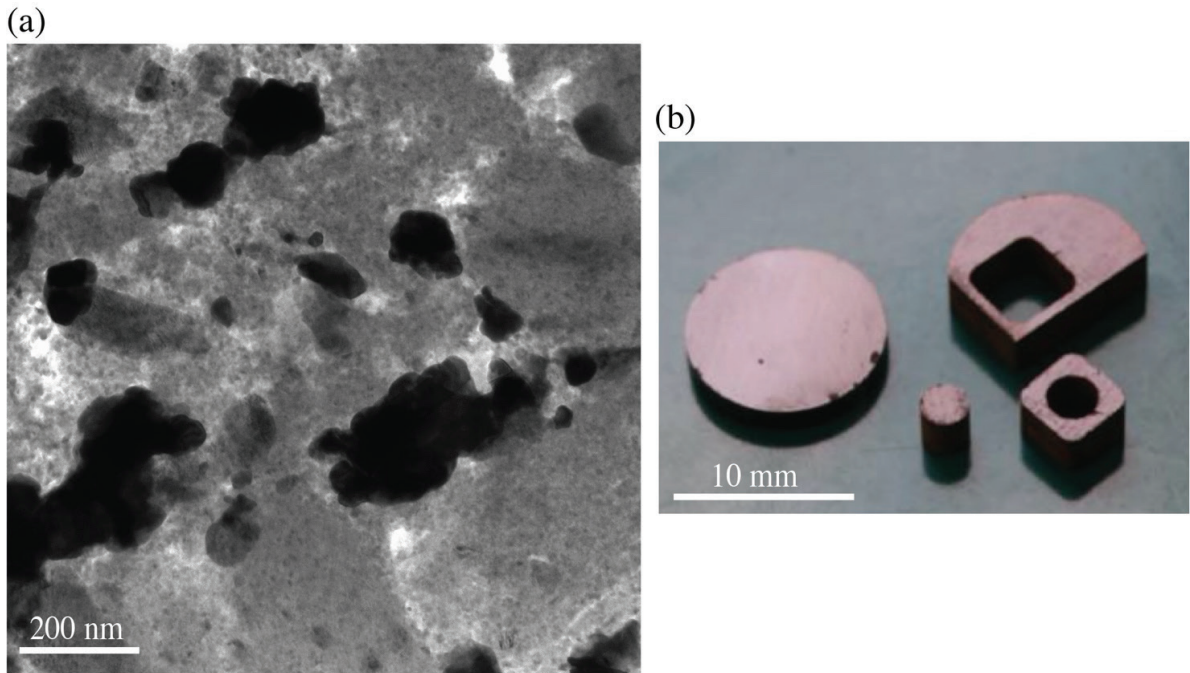


Figure 4:23 Sample 37 sintered at 250 °C. a) TEM image of the microstructure; b) Differents laser cut shapes on the sample.

4.7.5 1-carat

This sample has been produced with SPS method, sintered at 900 °C under 50 MPa. Its characteristics are reported in Table 4:5.

Table 4:5 Summary table of 1-carat sample

<i>Sample</i>	<i>Sintering method</i>	<i>T_{sintering}</i> (°C)	<i>Mass</i> (g)	<i>Thickness</i> (mm)	<i>Diameter</i> (mm)	ρ (g cm ³)	<i>Porosity</i> (%)	<i>Micro hardness (HV)⁵</i>
B2019	SPS	900	2.5	1.5	20	3.9	0.14	820±5

After polishing, the sample shows in an interesting “black-mirror” appearance, see inset in Figure 4:24. The orange square in the inset shows the position where a 100 nm thick lamella has been cut out of the pellet by the FIB technique. An SEM image of the lamella is shown in Figure 4:24a and b and in this last one the sparsed gold NPs are clearly visible in the titania matrix. By means of TEM we have magnified local spots of the lamella, see Figure 4:24c and d, to put in evidence the structure of gold NPs and titania grains. It appears that despite the high sintering temperature, gold NPs remain rather small. From XRD measurements the crystallite sizes have been found : $\langle z \rangle_{gold} = 30.1 \text{ nm}$ and $\langle z \rangle_{rutile} = 60 \text{ nm}$. An interesting observation stemming from Figure 4:24d is that the distance between gold NPs ranges from 100 to 200 nm, which is in fairly good agreement with our theoretical predictions reported in Figure 4:17.

⁵ Micro hardness Vickers : F= 0.5 kg, t=12 sec.

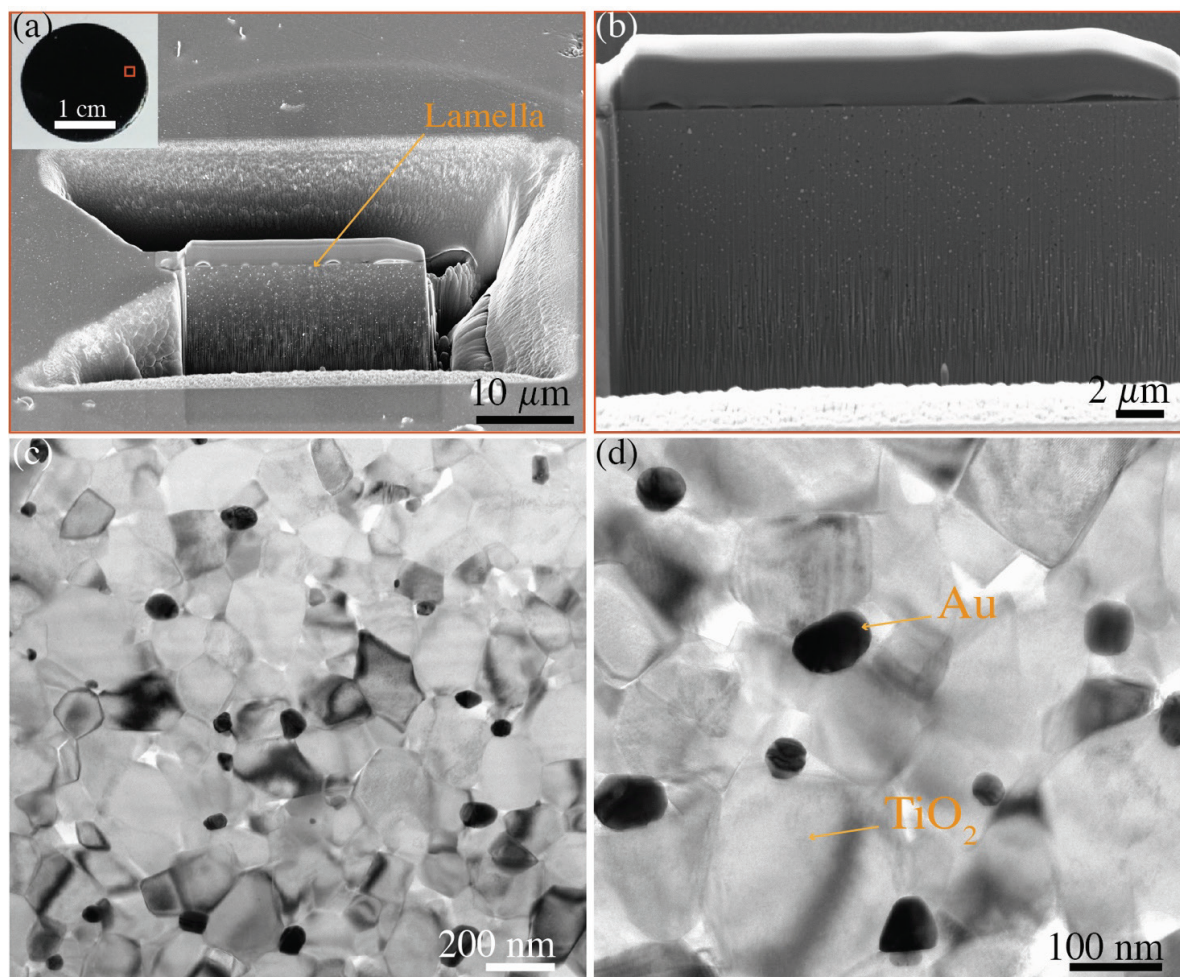


Figure 4:24 Au/TiO₂ composite with 4.2wt% Au. a) SEM image of the lamella cut by FIB. The pellet is shown in the inset, and the lamella position is the orange square in the inset; b) Front view SEM image of the lamella before the transfer on the TEM grid. The bright points corresponds to gold NPs in the dark Ti oxide; c) and d) TEM micrographs of the lamella.

An important observation is related to the mechanical properties, i.e. hardness. Despite the fact that the composite contains 4.2 wt% of very malleable noble metal, it shows a remarkable 800 HV Vickers hardness. This value approaches the typical hardness values of defect-free monocrystalline rutile titania. In Figure 4:25a cracks along the diagonals of the pyramidal Vickers indent put in evidence the ceramic behavior of the pellet. A matrix 4×4 of nanoindentations, whose results are reported in Figure 4:25b, has been carried out on the sample surface. The 16 loads curves perfectly overlap (they look like a single curve in the plot), showing a pretty good surface homogeneity of the pellets.

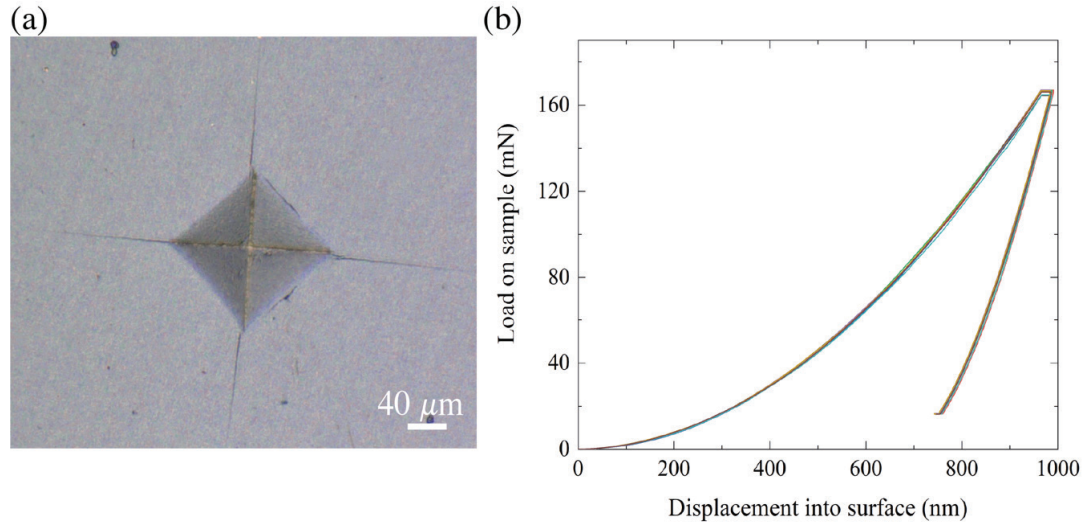


Figure 4:25 a) Optical microscope picture of indentation for Vickers hardness measurements, showing the ceramic fracture behavior of the sample; b) 16 nanoindentation hardness measurement cycles, on different positions in the sample, showing the applied load force as a function of the displacement into the surface.

4.7.6 Electrical resistivity as a function of carats

We measured the electrical resistivity as a function of the temperature of three samples, the two 18-carats of Table 4:3 and the one of 1-carat of Table 4:5. Results are reported in Figure 4:26, with the 18-carat sample behavior in the left plot while the 1-carat sample in the right plot.

The resistivity of all samples shows a monotone increase for temperature above 50 K, which indicates a metallic behavior for electron transport. This is somehow expected for the 18-carat sample, where 55at% are Au, but, remarkably, the metallic behavior is predominant over the semiconductor also for the 1-carat sample which contains less than 2at% Au. However, it is to be noticed the much higher resistivity value of this 1-carat sample, about 500 times the one's 18-carat sample.

The situation is different for temperatures below 50 K. The two 18-carats samples maintain the metallic behavior with a resistivity smoothly reaching a minimum value plateau. Using the typical RRR notation for metals, $RRR = \rho(T = 300\text{ K})/\rho(T = 4\text{ K})$, we see that B2022 sintered at 900 °C has better conduction properties: $RRR = 5$, while sample 41 sample has a $RRR = 2$, besides having a slightly higher resistivity at 300 K. The very low RRR value are typical of heavily alloyed material or strongly impured metal, which is certainly our case.

The 1-carat sample shows a weak, however, well visible, increase in resistivity when lowering the temperature below 50 K. We think this is a sign of the predominance of the semiconductor behavior of TiO₂, see Figure 2:11, over the metallic behavior of the gold, not surprising given the very sparse presence of gold in the TiO₂ matrix.

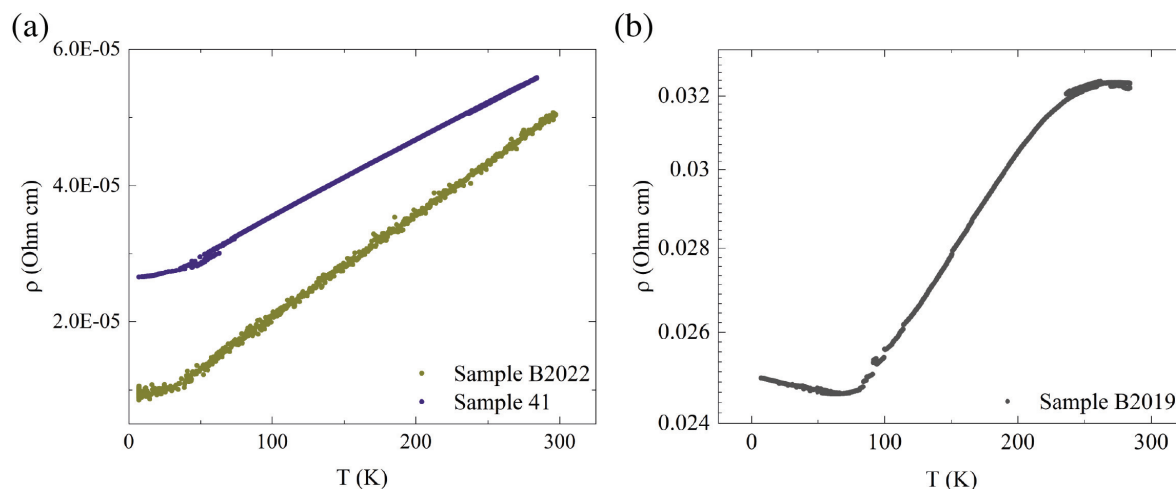


Figure 4:26 Resistivity curves versus temperature. a) 18-carats; b) 1.5-carat.

4.8 Conclusions

Our titania NWs have interesting properties for applications as a catalyst, one of the frontiers of nanomaterials, since they can be used as support for metal NPs. NPs of noble metals and gold, in particular, is very effective as a catalyst, for example, for CO oxidation, if the size of the particles remains small also after the thermal treatment that is usually associated with the manufactured for filters and other devices. We have investigated the behavior of gold NPs deposited on our titania NWs and we found out that size as small as 3-5 nm can be preserved for gold NPs even after 400 °C treatment in air. In a reducing atmosphere (hydrogen) size stabilization remains also at 800 °C. Our preliminary analysis points out to a very effective edge stabilization (Au NPs laying on the side of the NWs and touching the substrate), as well as to Ti³⁺ defects enhanced electronic SMSI effect.

We have investigated also the interaction of gold NPs with our TiO₂ NWs in bulk form and we have found very interesting properties for applications, for example, in the watch industry or jewellery. Composites pellets of various carats have been investigated and we demonstrated the possibility to tune colors and mechanical properties of the gold/titania pellets in a very interesting range.

Chapter 5 Photocatalysis applications

5.1 Photocatalysis

Photocatalysis is defined as the ability of a catalyst to generate electron-hole pairs ($e^- - h^+$) by means of the absorption of photons with energy bigger than the difference between the conduction and valence bands (band gap $E_g \sim 3.2$ eV for anatase). In the case of TiO_2 , when it is illuminated under a UV light ($\lambda \leq 387$ nm), a photo-generated e^- and h^+ pair is formed. A few electrons and holes migrate to the semiconductor surface without recombination and starts redox reactions with oxygen, water and other organic and inorganic species on the surface of the catalyst leading to the destruction or degradation of pollutants, as depicted in Figure 5:1 (178)(179). The electron then becomes a reducer and the hole a powerful oxidizer. To prevent recombination of e^- and h^+ , efficient photocatalysis needs a strong electron acceptor like O_2 or H_2O_2 (180). The highly reactive transitory species that are generated by illuminating TiO_2 and play an important role for the photocatalytic degradation of organic pollutants are: hydroxyl radical (OH^\bullet), superoxide radical ($O_2^{\bullet-}$) and hydrogen peroxide (H_2O_2). These highly reactive oxygen species (ROS), formed during UV activation, enable inactivity of different kind of bacteria like *Escherichia coli* (181), *Salmonella typhimurium*, *Pseudomonas aeruginosa* and *Enterobacter cloacae* (182). But numerous studies shows that OH^\bullet is the main important oxidant specie responsible for bactericidal effect, leading to membrane permeability modification and thus causing the cell death (183)(184).

Compared to the bulk form, nanosized TiO_2 particles are much more reactive because of their increased surface-to-volume ratio.

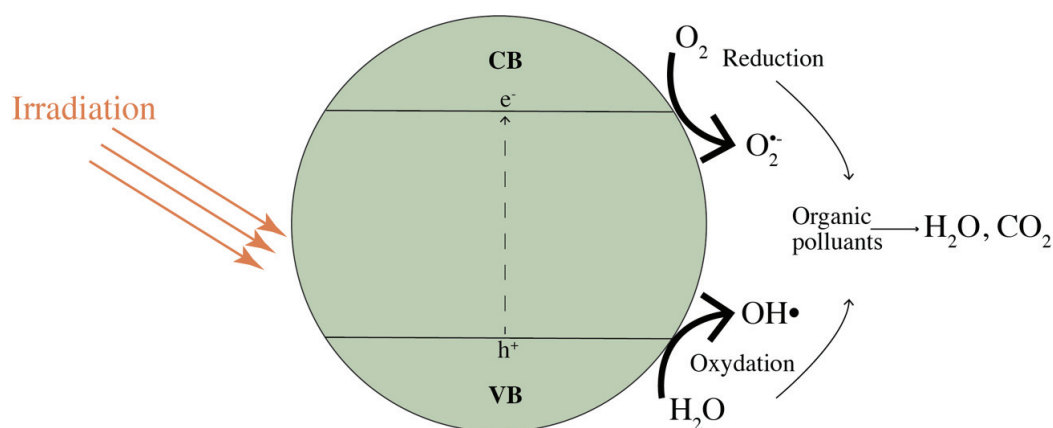


Figure 5:1 Schematic of the photocatalytic process. VB and CB are the valence and conduction band, respectively.

5.2 DNA decomposition

In this section we describe an experiment that has been carried out in order to assess the effectiveness of titania NWs to decompose DNA chains for biological applications.

5.2.1 Experiment preparation for DNA decomposition

We used a commercial DNA pUC19, which after treatment with an enzyme remains open, not supercoiled, with a length of 913 nm. A 10 ml dispersion containing of TiO_2 anatase NWs with a concentration of 0.81 mg/ml was prepared; Figure 5:2 shows a schematic of the consecutive experimental steps. 10 μl of titania NW dispersion was mixed in a test tube with 10 μl solution of DNA with a concentration of 2 ng/ μl . A countercheck control solution was prepared mixing DNA solution with distilled water in another test tube. Both test tubes were centrifuged and shaken and submitted to a 365 nm UV radiation. The lamp power was set to 16 mW/cm² and positioned at a distance of 58 mm above the liquid surface. The radiation treatment was carried out with a following cycle: 30 sec of irradiation session followed by 2 min of shaking and rotation without irradiation. This cycle avoids overheating that may induce unwanted breakage of the DNA chain. To make sure of keeping a constant temperature, avoiding spurious DNA decomposition, the test tube is partially immersed in a water pool acting as a thermal sink.

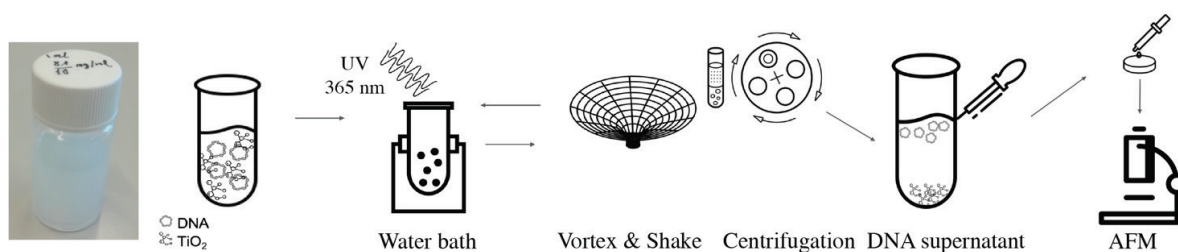


Figure 5:2 Experimental step for DNA visualization under AFM, from left to right: mother solution of 0.81 mg/ml TiO_2 NWs dispersed in water; test tube containing DNA and TiO_2 NWs; exposition of the test tube immersed in a water bath, to UV radiation for 30 second sessions; test tube is shaken for homogenize the solution in between irradiation sessions; centrifugation of the test tube in order to separate DNA from TiO_2 NWs; swab of DNA supernatant; deposition of DNA supernatant on a mica substrate; visualization of the sample via AFM. Figures adapted from Cyprien Mercier (EPFL, LPMC, internal presentation).

The UV irradiation cycles lasted 3, 5, 10 and 15 minutes. However, since TiO_2 NWs and DNA have different size, DNA is one order of magnitude thinner than titania NWs, separation of TiO_2 from DNA was necessary, allowing DNA observation with an AFM. The separation was done by centrifugation at 10,000 rpm for 5 minutes. Then 2 μl of the supernatant containing the DNA (while TiO_2

NWs precipitates), is mixed with 2 μl of MgCl_2 (10 mM) and 4 μl of distilled water. This final solution is deposited on a mica substrate which has an extremely smooth surface, with sub nanometer roughness. The sample was dried with nitrogen and imaged with AFM, where one could observe in a very local area the presence or the absence of DNA.

The AFM system used is a NX10 Park and measurements have been done in tapping mode with a PPP-NCSTR tip with a curvature radius < 10 nm.

An alternative method, global rather than local as in the case of AFM, was employed to measure the presence of DNA chains: the gel electrophoresis. The DNA migrates through the agarose gel, by electrophoresis, according to the applied voltage and to the DNA size and characteristics, according to the following formula:

$$v = \frac{E \cdot z}{f} \quad \text{Equation 5:1}$$

Where v is the speed, E the electric field, z the net charge and f the frictional force.

The position of DNA is evidenced by means of a suitable dye. The method is illustrated in Figure 5:3.

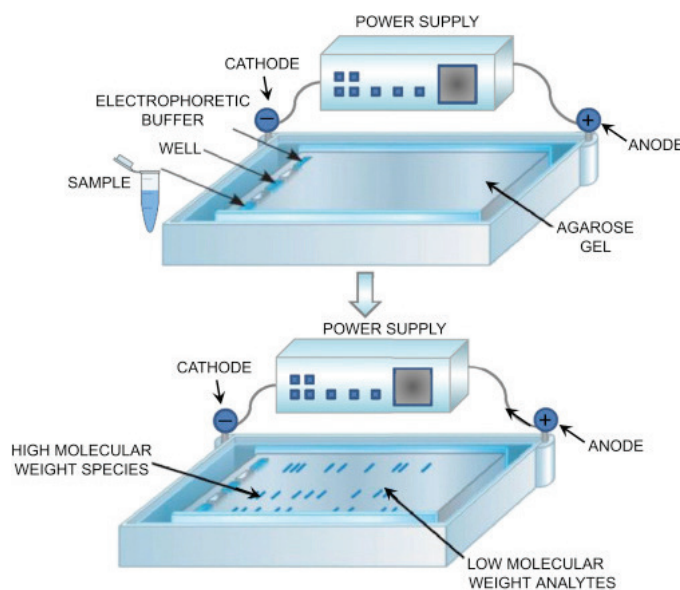


Figure 5:3 Gel electrophoresis process. Fig. taken from Ref. (185).

5.2.2 Results

We made a first campaign with four samples treated at 0, 3, 5 and 10 min of total UV illumination. We submitted to the same treatment also four control samples that underwent the same process without UV irradiation. Results are reported in Figure 5:4, where the AFM images show that after

10 min UV illumination, DNA mixed with TiO₂ NWs has completely disappeared, while it is well visible in the control sample. These results are however not conclusive since it was not always reproducible, in one case out of three presence of DNA was still detected. Various factors may affect the measurements for example DNA strands on mica substrate on random way; impurities may also mask the DNA; human factor during the collection of the DNA supernatant from the test-tube. In addition, it was questionable if DNA was really destroyed or simply disappear from the surface layer of the test tube because it stuck to TiO₂ NWs sediment during centrifugation. Finally, the local visualization of the intrinsic of AFM may mask global effect.

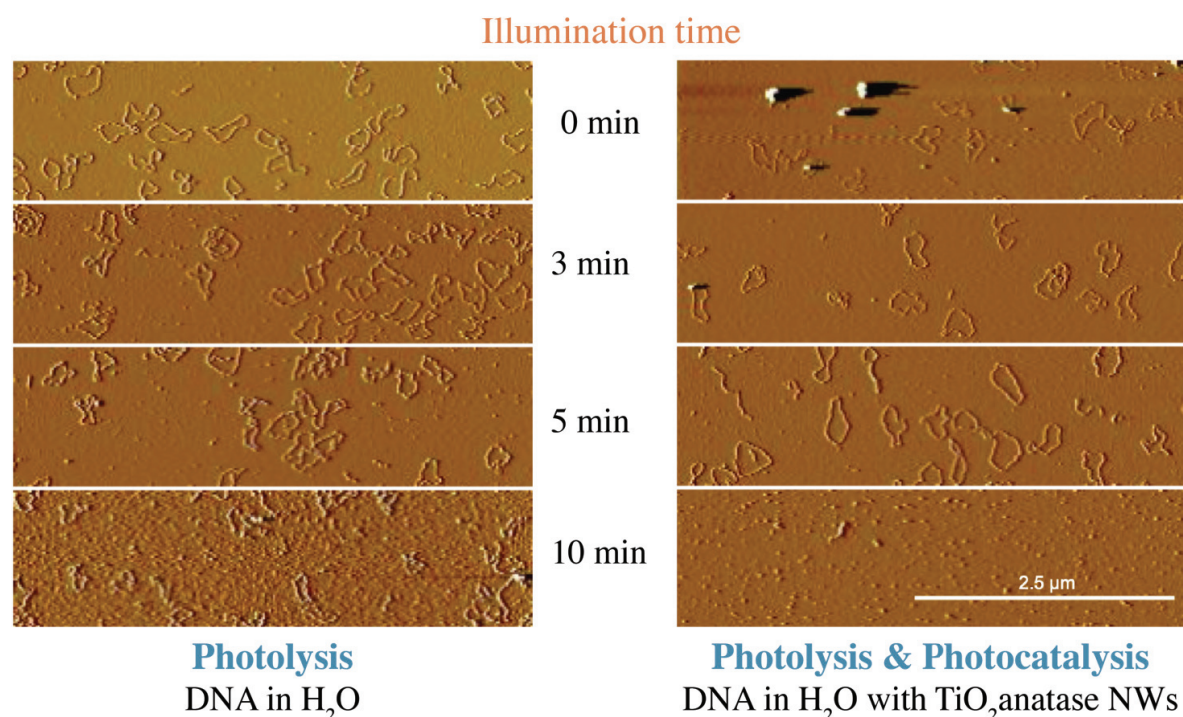


Figure 5:4 AFM images of DNA increasing the UV illumination time for control sample and sample containing TiO₂ NWs. Figures adapted from Cyprien Mercier (EPFL, LPMC, internal presentation).

Therefore, we decided to carry out test with long radiation cycle, up to 15 minutes and observation of DNA presence with gel electrophoresis, which allows a global visualization, as above mentioned. Thanks to this technique we could check that the DNA effectively remains in the supernatant part after centrifugation and is not present in the deposit in the test tube.

The results of various illuminations times are reported in Figure 5:5. One can observe that after 10 minutes UV illumination, TiO₂ photocatalyst has a detectable, although small effect: the quantity of DNA is only partially reduced. This may explain the non-reproducible measurement of AFM which is very local. However, after 15 minutes the DNA is fully decomposed, no trace remains, see right

side of Figure 5:5. The comparison between the test tube solution and the solution with titanium nanowires as photocatalyst is quite striking.

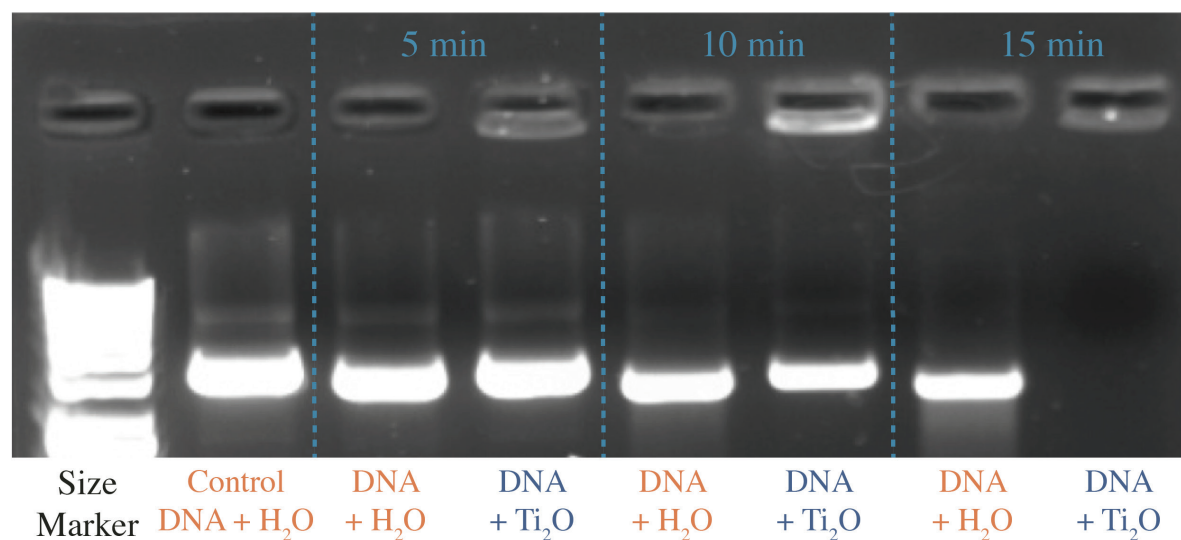


Figure 5:5 Gel electrophoresis markers of solutions exposed at different illuminations times; for each couple we have the control solution of DNA in H₂O and our experiment solution DNA in H₂O with TiO₂ NWs. Figures adapted from Cyprien Mercier (EPFL, LPMC, internal presentation).

5.2.3 Conclusion

We have demonstrated that anatase NWs can be quite effective catalyst in DNA destruction via UV illumination. From our measurements a 15 min illumination is required to fully destroy the DNA strands. However, this is a first step, a proof of principle. More systematic investigations are required in order to optimize the process, making faster and more efficient the DNA decomposition.

5.3 Reusable protective masks

A very special application of our TiO₂ NWs relies on the photocatalytical generation of high level of ROS upon UV illumination and on a high electric constant of the material. This last is extremely important to enhance wettability by water droplets by carrying germs. A TiO₂ based-filter, of high efficiency for protective masks and air conditioning has been recently proposed (186) also to cope with the recent Covid-19 crisis.

As above mentioned, the basic principle is the one exposed in Section 5.1. The titania NWs film can be made in a shape of a filter paper, whose pore size can be suitably tuned, supported by a simple frame obtained via 3D printing. Figure 5:6 shows the TiO₂ filter and report scheme of the UV assist-

ed photochemical process that results in destruction of the organic metals in proximity of the NWs, as illustrated Section 5.1. The presence of water is essential: for this reason, the high dielectric constant of TiO_2 $\epsilon = 70\text{--}80$ is a key feature. A high value is important also to enhance the filter capability of our TiO_2 paper since it facilitated wetting of the filter surface by droplets of water or saliva, which is known to be one of the most important medium carrying Covid-19 germs.

The filter can be easily regenerated by exposing to UV. In this way, one can avoid the tons of waste that can be envisaged with the use of millions of masks per day, with big benefit for the environment and logistics. Such a TiO_2 NWs based lyophilized sterilizable masks might be reused more than 1000 times, indeed.



Figure 5:6 a) The upscale of the synthesis showing titanate NWs production; b) TiO_2 NWs filter paper resulting from the spreading and thermal treatment process (73); c) SEM image of the filter with the sketch of germs to be filter out; d) Schematic of the photocatalytic process on a TiO_2 NWs.

A prototype of the mask based on TiO_2 NWs filter paper and fixed with 3D printer is illustrated in Figure 5:7 with an example of a person wearing the mask. It should be added that such a nanoporous photocatalytic filter can be used for other purposes, like air conditioners and water purification. One of the co-authors (Dr. Endre Horváth) has successfully tested this approach in experimental water-purification plants in Switzerland and South Africa.

The kilogram-scale production of TiO_2 NWs can be improved to ton-scale credibility to its massive application potentials.

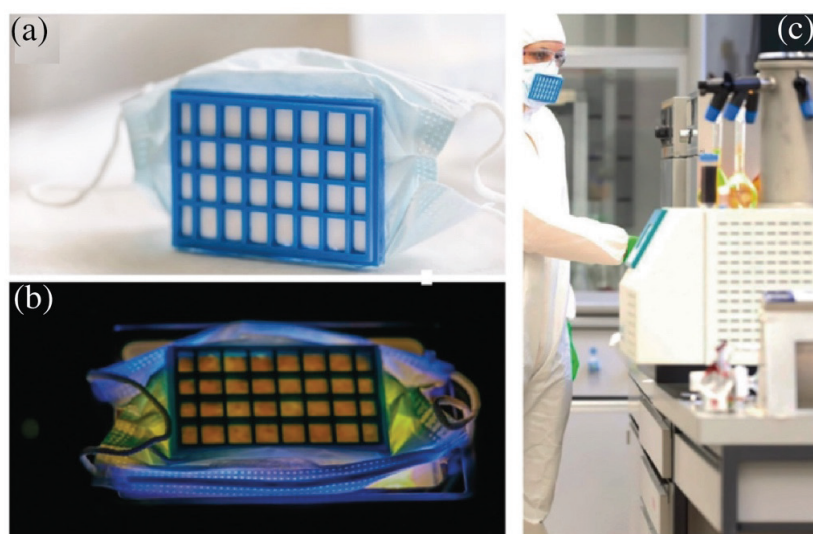


Figure 5:7 a) Photo of a prototype of a mask in which the TiO_2 NW filter paper is fixed to a 3D-printed frame; b) after use under 365 nm UV illumination; c) Photo of the mask in real conditions (courtesy of the pre-launch start-up Swoxid).

5.4 Photocatalytic activity on 3D composites pellets

In this section we present the photocatalytic activity of few nanocomposites gold/titania 3D pellets of different carats.

5.4.1 Experiment preparation

The photocatalytic activity of nanocomposites gold/titania 3D pellets were evaluated by means of discoloration of the methylene orange (MO) dye, under UV light irradiation (wavelength centered at 365 nm, and with an irradiance of $\sim 16 \text{ mW/cm}^2$). Methyl orange is a typical organic molecule to evaluate the photocatalytic efficiency of a given catalyst. Using the absorption at 464 nm as a marker of the MO concentration, we plotted the concentration of MO, proportional to the absorbance of

the solution according to the Lambert-Beer law, as a function of the irradiation time; the concentration value is taken every 10 minutes. Samples of our pellets, listed in Table 5:1, are placed in a small beaker with 7 ml of 10 mg/l MO solution, see Figure 5:8. Because samples are porous and they absorb the liquid, we waited half an hour before starting the UV exposure.

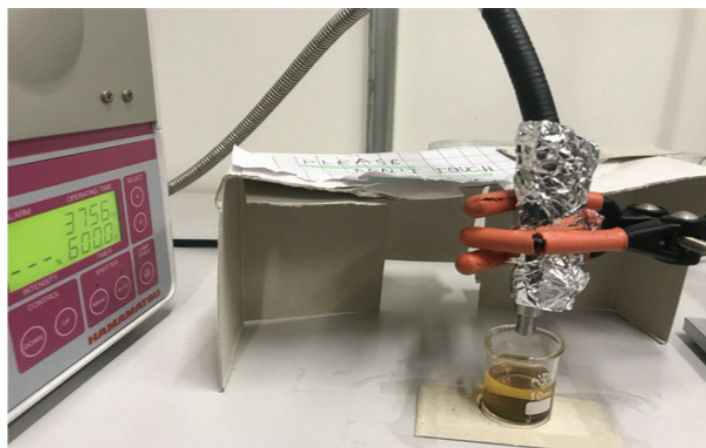


Figure 5:8 Experimental setup showing the UV source on the top of the beaker containing a pellet in the MO dye. Figures adapted from Guillemette Bourdieu and Elisa Vidal-Revel (EPFL, LPMC, internal presentation).

5.4.2 Results

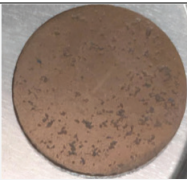
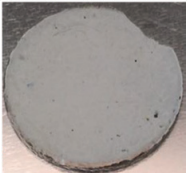
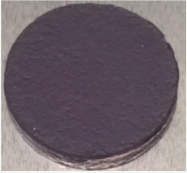
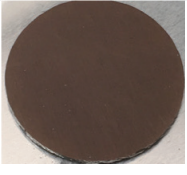
Figure 5:9a shows the photocatalytic activity of the three samples with different noble metal content; for comparison, the decrease of pure MO (i.e. with no pellet) under illumination is reported. Sample B2027 exhibits a considerable photocatalytic activity and after 90 min the initially orange solution became almost colorless under UV light, indicating the significant degradation of MO. Because sample B2027 is the most active, the experiment has been repeated three times and we can observe a decrease of the activity at each irradiation,

Figure 5:9b. To investigate how we can counteract this saturation of the effectiveness of the 18-carat-pellet as photocatalyst with multiple usages, we studied the behavior of B2027 in an acidic methyl-orange solution of pH = 3.5. Actually,

Figure 5:9b shows that when the sample is in a MO acid solution, it behaves like the first time we use it (green curve on the Figure), i.e. regeneration in acid solution is effective. Finally, we have compared sample B2027 with sample B2029,

Figure 5:9c, that have sample metal content. The photocatalytic activity of B2029 is like the one of B2027 at its second use.

Table 5:1 Summary of samples studied for the photocatalytic activity.

<i>Sample⁶ #</i>	<i>Picture</i>	<i>Au wt%</i>	<i>TiO₂ wt%</i>	<i>Porosity %</i>
B2027		75	25	28.6
B2017		0	100	22.6
B2018		4.2	95.8	43.4
B2029		75	25	28.2

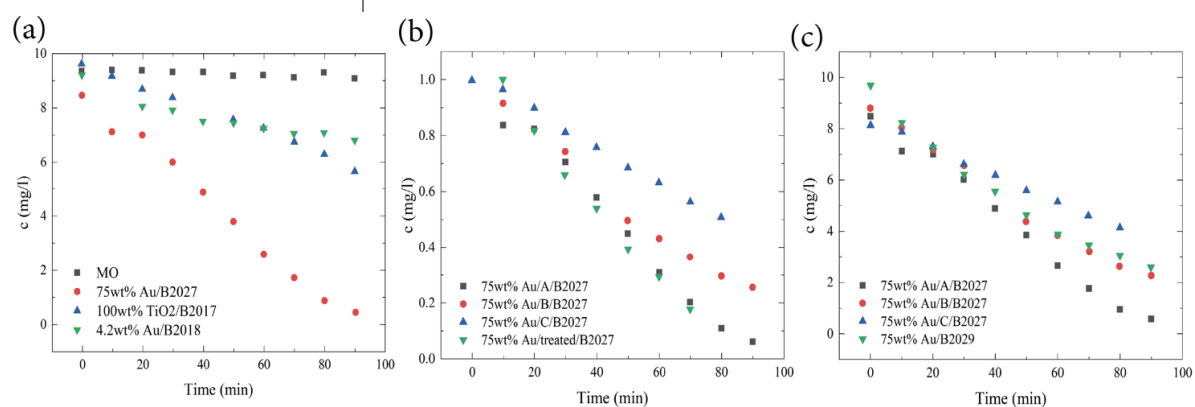


Figure 5:9 Photocatalytic activity of 3D gold/titania pellets compared to the discoloration of pure MO under UV illumination. (lines are to guide the eye). a) Sample B2027, B2017 and B2018; b) Sample B2027 shows a decrease of activity (A, B, and C correspond to first, second and third measurements). The sample is then

⁶ All samples have been sintered via SPS method.

treated in acid; c) Comparison between sample B2027 and B2029. Figures adapted from Guillemette Bourdieu and Elisa Vidal-Revel (EPFL, LPMC, internal presentation).

5.4.3 Conclusion

We have investigated the effectiveness of our TiO_2 pellets, with and without gold NPs, as photocatalyst for degrading methyl orange. We found that the 18-carat pellets (i.e. 75wt% Au) are very effective photocatalysts and by treatment, in acid solution, the pellet can be easily regenerated and its effectiveness preserved for multiple cycles. These experiments depict that these type of photocatalytic cermet composites may serve as new generation of UV sterilizable bioinert alloys for medical application (dentistry, implants and pacemakers) and jewellery and watches.

Conclusions and outlook

TiO₂ is one of the most popular oxides in the field of advanced materials and has a wide range of applications, in particular in its nanoparticle form for photocatalytic applications. With the progress in nanotechnology applications and material synthesis, H₂Ti₃O₇ nanowires are gradually appeared in prototypes and demonstrators, either in titanate or as a precursor of TiO₂ nanowires in the anatase phase. The anisotropic nanofilamentary form of TiO₂, (i.e. nanofibers, nanowires, nanobelt, nanotubes) introduced at the end of the last millennium, increase dramatically the amount of surface atoms able to react with the environment.

TiO₂ nanowires are often used in 2D or 3D architectures and, depending on the application, and during the preparation of these architectures heat treatment is required.

In this thesis, I discovered the crystal phase and morphological evolution of TiO₂ nanowires, processed with specific thermal treatment, as a single filament or as a bulk assembly. The study covered characterizations of TiO₂ nanowires in pristine form or as a support of metal nanoparticles.

I have investigated the coarsening behavior of single-crystalline titanate (H₂Ti₃O₇) nanowires both when alone, suspended over a micron hole of the SiO₂ support and when laying entirely on the support, comparing them to the behavior of 3D assemblies of the same composition. Two temperature-dependent geometrical transformation phase changes have been identified, both for single nanowire on the substrate (2D system) and for nanowire pellets (3D). During the first phase change (titanate to anatase recrystallization, above 200 °C and up to 600 °C) significant shrinking of the height of the nanowire is observed. During the second regime, at sintering temperature of 600-1000 °C an anomalous coarsening manifested as an increased surface area of the individual nanowires deposited on a surface. In addition to the strong surface effects, in the 2D system, we noticed an unexpected and unusual stabilization of the metastable anatase phase and the absence of the rutile phase even above 900 °C. In contrast, for 3D assembly of nanowires, from 600 °C, the classical Ostwald ripening particle coarsening is observed, accompanied by typical, thermodynamically favorable anatase to rutile phase transition at 900 °C.

As far as the mechanical stability of 2D and 3D architectures is concerned, we found that the 3D pellets of sintered anatase nanowires, show considerably higher microhardness values when compared to sintered bodies composed of nearly spherical nanoparticles. After sintering at 600 °C the pellets have a hardness value of 115 HV (44% porosity) while, after 900 °C sintering increases microhardness value up to 941 HV (1.6% porosity), actually very close to the one of TiO₂ single crystal. I performed mechanical measurements on single titanate nanowires (2D architecture), too, by

means of AFM-based bending test. I have evidenced the layered structure of our nanowires, with a relatively low shear modulus value: $G = 1.5 \pm 0.8$ GPa. To the best of our knowledge, it is the first time that the shear modulus has been measured on this type of layered nanowires, whose flexural behavior is dominated by its low shear modulus despite a high elastic modulus, evaluated as: $E = 67 \pm 25$ GPa. Once transformed and recrystallized into anatase NWs, the shear between layers is inhibited and E goes above 100 GPa, not far from the bulk value.

The titania nanowire 2D system, have shown quite peculiar characteristics as support of gold nanoparticles. We have found that size as small as 3-5 nm can be preserved for gold nanoparticles even after 400 °C treatment in air. In a reducing hydrogen atmosphere, the gold nanoparticle size stabilization was observed at temperatures as high as 800 °C. All our preliminary results support an effective edge stabilization phenomenon as the main source of the inhibition of the noble metal particle coalescence. The Ostwald ripening was significantly reduced for Au nanoparticles laying on the side of the NWs and touching the SiN substrate. We evidenced also stabilization due to Ti^{3+} defects enhanced electronic SMSI effect.

I carried out a complementary study about the interaction of gold nanoparticles with TiO_2 nanowires in bulk form. Composites pellets of various carats have been sintered and thoroughly investigated. The possibility to tune colors in a wide range, from violet to green, as well as very good hardness properties, of our gold/titania pellets have been demonstrated.

Finally, I focused my attention on heterogeneous photocatalytic applications, showing that TiO_2 nanowires are an effective catalyst to decompose organic matter during light-induced redox reactions. In particular, we demonstrate that TiO_2 NWs in aqueous solution effectively destroy DNA chains after suitable (10-15min long) exposition to UV irradiation. If one uses TiO_2 NWs in the form of paper filters integrated in face masks and respirators, similar damage may be triggered upon UV illumination to destroy viruses and bacteria. The characteristic of this facial mask would be the easy regeneration with simple UV exposition, such as it can be reused hundreds or thousands of times, cutting down the economical cost and reducing the environmental impact as compared to the currently used disposable plastic microfiber based masks trashed in million quantities per day during the ongoing Covid-19 pandemic. I also investigated the catalytical effectiveness of our TiO_2 in 3D architecture. TiO_2 – gold composite pellets were effectively discolored methyl orange model molecules in photoinduced test reaction. Importantly, we found that the 18-carat pellets (i.e 75wt% Au) are not only efficient, but robust, hence it can be easily regenerated and reused in multiple cycles, a basic requirement toward real-world application.

The results of my thesis work have contributed to the fabrication of novel, mechanically more stable titanium oxide nanowire-based coatings and 3D functional ceramics, which is a prerequisite for safer and durable potential products. The detailed characterization we carried out on the 3D system (pellets) and 2D architectures and the basic building unit, to single fiber, has allowed determining the material's mechanical properties as well as its interaction with various metal nanoparticles. However, a few characterizations are still missing to complete the work. For instance, the toughness values of the titania/gold nanoparticle pellets is unknown today. Mechanical toughness is indeed

very important for applications in jewelry, and this use case served as of the main motivation for this study. Our bulky 3D system is indeed very special being sintered from two nanocomponents, TiO₂ NWs and Au NPs, where both the oxide and the metal retained nanoscale crystallite sizes and the end of the sintering procedure with low porosity. Theoretical works predict interesting toughness phenomena, decent hardness values, while the ability for such a ceramic-metal (cermet) composite to undergo plastic deformation. Such properties are long-sought and it may open new applications if properly pursued.

The 2D NWs system supporting noble metal NPs are ideal potential candidates for catalytical applications like car exhaust pipe and fuel cells. I hope that follow-up works inspired by the basic science data reported here will successfully demonstrate the practical applicability of the observed sinter-resist system. As far as the photocatalytic applications concerned, the most pertinent and promising use case appears to be the reusable antiviral facial mask concept. However, to fully validate our system in a real condition we would need to effectively determine the filtration efficiency according to the present standard, measuring the filtering efficiency versus particle size especially for viruses which are well below the micron size the high efficiency of our system is still to be fully demonstrated. Another point probably less controverted but still very important is to measure the regeneration efficiency under UV cycles and the maximum number of cycles that can be safely applied. More tests under real operating conditions are needed to make sure of the NWs cloth integrity is not changing in time, no cracks appear during wear. In other words, a rigorous procedure for passing from proof-of-principle to a pre-industrialization phase is needed in the near future.

Anyway, despite the fact that significant amount of experimental work that is still ahead to assess the technical and economic sustainability in operative conditions for each of the above-mentioned applications, in my thesis study I laid down the foundation of the innovation potential of these materials, that they may serve as building blocks of future flexible energy devices, environmental decontamination systems, super thermal-insulators, sensors, catalyst supports and fiber-reinforced plastics, metals and ceramics.

The tech transfer potential of one of the breakthrough application, the nanoporous, reusable and antiviral face mask use case is currently planned to be exploited via the activities of a pre-launched EPFL supported start-up. I am glad to be part of the journey and I sincerely hope that my present and future work will contribute in the accomplishment of the mission and vision of the startup to commercialize such an effective, low cost, recyclable, environmentally sustainable filtering masks to battle against the present Covid-19 and any future pandemics.

Appendix A

The appendix aim is to give more details about the technique that were used during the experimental analysis.

Archimede's method

Densities of all 3D pellets samples were measured by the water immersion method. Theoretical densities of:

- TiO_2 anatase : 4 g/cm^3
- TiO_2 rutile : 4.23 g/cm^3
- Au : 19.3 g/cm^3

Are used to evaluate the densification ratio.

Archimede's formula is:

$$\rho_{app} = \frac{m_{air}}{(m_{air} - m_{water})} \rho_{water} \quad \text{Equation 1}$$

Where ρ_{app} is the sample density, m_{air} is the sample mass measured in air, m_{water} is the sample mass measured by immersion in water and ρ_{water} is the density of water at the temperature of the measurement.

For very porous samples this method is not very appropriate because it overestimates the sample density which presents open porosity. During sample immersion in deionized water, the liquid penetrates into the pellet and leads to an increase of the weight.

The open porosity (OP) and corrected density were estimated using the following equations:

$$OP = \frac{m_{air} - m_{wet}}{m_{wet} - m_{water}} \quad \text{Equation 2}$$

And

$$\rho_c = \frac{m_{air}}{m_{air} - m_{wet}} \rho_{water} \quad \text{Equation 3}$$

m_{wet} is the weight of the wet sample.

Acknowledgements

“I clearly can say that we stand on the shoulders of giants that came before us”; this famous sentence perfectly adapts to this work. Almost four years ago I started this fascinating adventure, and I am very grateful for having been offered this thesis project. The results presented in this work would not have been possible without all the people around me that I would like to acknowledge in this section.

I want to start by expressing my sincere and deep gratitude to my two supervisors, Prof. László Forró and Dr. Endre Horváth. Thanks, Prof. László Forró for giving me the opportunity to conduct my thesis in your laboratory, for your encouragement, your scientific support and the very appreciated convivial atmosphere in your group. Your door was always open to discussions and you always ready to sharing your vast knowledge.

A whole heartedly special thanks to you Endre, for having chosen me for this passionate and “colored” project. You have always pushed me further, giving me tools and method to overcome the many obstacles on my way, thanks to your great laboratory experience and scientific knowledge. I am very grateful for your patience, for guiding me along the experiments and for your intuition for providing directions and target to focus my research. I worked on the material you have been developed for 17 years, your scientific legacy: thank you for trusting me.

My acknowledgments also go to the private swatch company that supported this ambitious project: I learned a lot from my first two years of direct collaboration together.

I also want to thank all the members of scientific jury of my final examination, for reading the manuscript and for taking the time to propose all improvements that make its final version: Prof. Paolo Ricci, chair the committee examination, Prof. Dragan Damjanovic, Prof. Vladimir Srdić and Dr. Laurent Boilet.

I wish to give a special mention to Raphaël Foschia because he patiently taught me many things about the atomic force microscope and other instruments. Our collaboration has been essential for this thesis work and I hope we will be able to collaborate again in the near future. Thanks for the enthusiasm and the many conversations and discussions to: Prof. Davor Pavuna, Prof. Karoly Holczer, Dr. Andrzej Sienkiewicz, Dr. Alla Arakcheeva, Dr. Daniele Mari, Dr. Iva Tkalčec, Dr. Ayat Karimi. I would like to mention the helpful meetings with my mentor of the doctoral school, Prof. Vincenzo Savona, that I thanks also for the suggestions about future perspectives.

A special thanks to the CIME (centre interdisciplinaire de microscopie électronique) staff of 2016, when I started my thesis work, and to the present staff, for all the help, support and scientific discussions: In particular I wish to thank Marco, Thomas, Duncan, Barbora, Fabienne and Gregoire.

I would like to acknowledge the Crystal Growth Facility for the help and guiding me during experiments, in particular to Arnaud (also for advices and friendship) and David.

A thank you also to the technical support which helped me to achieve my experiments: the IT team, in particular Baptiste, the electricians, the staff of the mechanical workshop, in particular, Gilles, Olivier, Claude, Luc, Philippe. Of course, a huge thanks to Gerald for his help, support, motivation and discussions on the PH corridor. Thanks also to Antonio and Nicolas for TP assistance and Nicole and Anh for their administrative support, always very efficient and helpful.

I also want to thank the external collaborators. First of all, the people of the Belgian Ceramic Research Center (BCRC): in particular I would like to gratefully acknowledge Laurent, Jean-Pierre and Védi for SPS experiments and learned discussions. I would like to thanks also Martial and Elizaveta from Nanyang Technological University (NTU) in Singapore for in-situ TEM experiments.

I would like to express my gratitude to Péter, my officemate and friend: your dynamism and your pragmatic attitude with which you encouraged me to look for possible ways to problem-solving, have been very helpful. A huge thanks to Andrea for having introduced me to this laboratory. I had the good luck to have met people really passionate about their research.

I sincerely appreciated the help and friendship of LPMC and LQM labmates, in particular Xavier, Gaétan, Edoardo, Márton, Konstantins M., Konstantin S., Pavao, Luka, Trpimir, Maryam, Balint, Péter M., Davor, Iness, Mathieu, Sergiy, Claudio, Dunja, Milica, Anastasiia, Alex, Ellen, Priya, Raffaele, Samy, Virgile, Luc.

I thank the TP IV students who have to spend one or two semesters in our laboratory, their help and motivation helped me with experiments; in particular Valentin, Guillemette, Elisa and Cyprien. I had the happy chance to share few weeks of AFM measurements with Najeres: we were both pregnant and your company during these moments was precious to me.

I had the great fortune to be supported by many friends, nearby and far away... they are really too much and it is impossible to mention all them...

Finally, I would like to warmly thanks my Family. I am grateful to my parents and brother Pietro. This accomplishment would not have been possible without them and their unconditional support. I thank also, my grandmother, uncles and aunt, my family in law, all my cousins for their continuous encouragements.

My profound gratitude to my husband, Geoffroy, a real companion during these ten last years together; your patience, understanding and indefectible support, Geoffroy, have been fundamental to accomplish this work. Thanks to my 15-months-old daughter, Elena, to be such a lovely gift to us.

L.R.

Lausanne, May 2020

Bibliography

1. I. Freestone, N. Meeks, M. Sax, C. Higgitt, The Lycurgus Cup — A Roman nanotechnology. *Gold Bull.* **40**, 270–277 (2007).
2. The Nobel Prize in Physics 1986. *NobelPrize.org*, (available at <https://www.nobelprize.org/prizes/physics/1986/summary/>).
3. G. Binnig, H. Rohrer, Ch. Gerber, E. Weibel, Tunneling through a controllable vacuum gap. *Appl. Phys. Lett.* **APLCLASS2019**, 178–180 (1998).
4. H. K. Wickramasinghe, Scanning probe microscopy: Current status and future trends. *Journal of Vacuum Science & Technology A*. **8**, 363–368 (1990).
5. F. Ohnesorge, G. Binnig, True Atomic Resolution by Atomic Force Microscopy Through Repulsive and Attractive Forces. *Science*. **260**, 1451–1456 (1993).
6. Y. Martin, C. C. Williams, H. K. Wickramasinghe, Atomic force microscope–force mapping and profiling on a sub 100-Å scale. *Journal of Applied Physics*. **61**, 4723–4729 (1987).
7. A. Kis, Mechanical properties of mesoscopic objects. *Infoscience* (2003), , doi:10.5075/epfl-thesis-2876.
8. B. Cappella, G. Dietler, Force-distance curves by atomic force microscopy. *Surface Science Reports*. **34**, 1–104 (1999).
9. RTESPA-300-30 - Bruker AFM Probes, (available at <https://www.brukerafmprobes.com/p-4033-rtespa-300-30.aspx>).
10. D. B. Williams, C. B. Carter, in *Transmission Electron Microscopy: A Textbook for Materials Science*, D. B. Williams, C. B. Carter, Eds. (Springer US, Boston, MA, 2009; https://doi.org/10.1007/978-0-387-76501-3_1), pp. 3–22.
11. ZEISS Sigma - Votre MEB-FEG pour l'imagerie haute qualité et la microscopie analytique avancée, (available at <https://www.zeiss.fr/microscopie/produits/microscopes-electroniques-a-balayage/sigma.html>).
12. J. Goldstein, D. E. Newbury, D. C. Joy, C. E. Lyman, P. Echlin, E. Lifshin, L. Sawyer, J. R. Michael, *Scanning Electron Microscopy and X-Ray Microanalysis: Third Edition* (Springer US, ed. 3, 2003; <https://www.springer.com/gp/book/9780306472923>).
13. W. H. Bragg, W. L. Bragg, The reflection of X-rays by crystals. *Proceedings of the Royal Society of London. Series A, Containing Papers of a Mathematical and Physical Character*. **88**, 428–438 (1913).

14. P. Scherrer, Bestimmung der Größe und der inneren Struktur von Kolloidteilchen mittels Röntgenstrahlen. *Nachrichten von der Gesellschaft der Wissenschaften zu Göttingen, Mathematisch-Physikalische Klasse*. **1918**, 98–100 (1918).
15. S. Malato, P. Fernández-Ibáñez, M. I. Maldonado, J. Blanco, W. Gernjak, Decontamination and disinfection of water by solar photocatalysis: Recent overview and trends. *Catalysis Today*. **147**, 1–59 (2009).
16. A. Fujishima, K. Hashimoto, T. Watanabe, *TiO₂ photocatalysis: fundamentals and applications* (Bkc, Tokyo, 1999).
17. B. O'Regan, M. Grätzel, A low-cost, high-efficiency solar cell based on dye-sensitized colloidal TiO₂ films. *Nature*. **353**, 737–740 (1991).
18. D. B. Strukov, G. S. Snider, D. R. Stewart, R. S. Williams, The missing memristor found. *Nature*. **453**, 80–83 (2008).
19. J. H. A. Martens, R. Prins, H. Zandbergen, D. C. Koningsberger, Structure of rhodium/titania in the normal and the SMSI state as determined by extended x-ray absorption fine structure and high-resolution transmission electron microscopy. *J. Phys. Chem.* **92**, 1903–1916 (1988).
20. L. Forro, O. Chauvet, D. Emin, L. Zuppiroli, H. Berger, F. Lévy, High mobility n-type charge carriers in large single crystals of anatase (TiO₂). *Journal of Applied Physics*. **75**, 633–635 (1994).
21. N. Tétreault, E. Horváth, T. Moehl, J. Brillet, R. Smajda, S. Bungener, N. Cai, P. Wang, S. M. Zakeeruddin, L. Forró, A. Magrez, M. Grätzel, High-efficiency solid-state dye-sensitized solar cells: fast charge extraction through self-assembled 3D fibrous network of crystalline TiO₂ nanowires. *ACS Nano*. **4**, 7644–7650 (2010).
22. J. Jaćimović, E. Horváth, B. Náfrádi, R. Gaál, N. Nikseresht, H. Berger, L. Forró, A. Magrez, From nanotubes to single crystals: Co doped TiO₂. *APL Materials*. **1**, 032111 (2013).
23. H. Mehranpour, M. Askari, M. S. Ghamsari, H. Farzalibeik, Study on the Phase Transformation Kinetics of Sol-Gel Drived Nanoparticles. *Journal of Nanomaterials* (2010), , doi:10.1155/2010/626978.
24. V. K. LaMer, R. H. Dinegar, Theory, Production and Mechanism of Formation of Monodispersed Hydrosols. *J. Am. Chem. Soc.* **72**, 4847–4854 (1950).
25. X. Mettan, J. Jaćimović, O. S. Barišić, A. Pisoni, I. Batistić, E. Horváth, S. Brown, L. Rossi, P. Szirmai, B. Farkas, H. Berger, L. Forró, Tailoring thermal conduction in anatase TiO₂. *Commun Phys*. **2**, 1–7 (2019).

-
26. P. Szirmai, J. Stevens, E. Horváth, L. Ćirić, M. Kollár, L. Forró, B. Náfrádi, Competitive ion-exchange of manganese and gadolinium in titanate nanotubes. *Catalysis Today*. **284**, 146–152 (2017).
27. P. Szirmai, E. Horváth, B. Náfrádi, Z. Micković, R. Smajda, D. M. Djokić, K. Schenk, L. Forró, A. Magrez, Synthesis of Homogeneous Manganese-Doped Titanium Oxide Nanotubes from Titanate Precursors. *J. Phys. Chem. C*. **117**, 697–702 (2013).
28. P. Szirmai, B. Náfrádi, A. Arakcheeva, E. Szilágyi, R. Gaál, N. M. Nemes, X. Berdat, M. Spina, L. Bernard, J. Jaćimović, A. Magrez, L. Forró, E. Horváth, Cyan titania nanowires: Spectroscopic study of the origin of the self-doping enhanced photocatalytic activity. *Catalysis Today*. **284**, 52–58 (2017).
29. B. Náfrádi, G. Náfrádi, C. Martin-Hamka, L. Forró, E. Horváth, Superior Water Sheeting Effect on Photocatalytic Titania Nanowire Coated Glass. *Langmuir*. **33**, 9043–9049 (2017).
30. K. Mantulnikovs, P. Szirmai, M. Kollár, J. Stevens, P. Andričević, A. Glushkova, L. Rossi, P. Bugnon, E. Horváth, A. Sienkiewicz, L. Forró, B. Náfrádi, Light-induced charge transfer at the CH₃NH₃PbI₃/TiO₂ interface—a low-temperature photo-electron paramagnetic resonance assay. *J. Phys. Photonics*. **2**, 014007 (2020).
31. M. T. Byrne, J. E. McCarthy, M. Bent, R. Blake, Y. K. Gun'ko, E. Horvath, Z. Konya, A. Kukovecz, I. Kiricsi, J. N. Coleman, Chemical functionalisation of titania nanotubes and their utilisation for the fabrication of reinforced polystyrene composites. *J. Mater. Chem.* **17**, 2351–2358 (2007).
32. T. Szabó, V. Tóth, E. Horváth, L. Forró, I. Szilágyi, Tuning the Aggregation of Titanate Nanowires in Aqueous Dispersions. *Langmuir*. **31**, 42–49 (2015).
33. M. Pavlovic, M. Adok-Sipiczki, E. Horváth, T. Szabó, L. Forró, I. Szilágyi, Dendrimer-Stabilized Titanate Nanowire Dispersions as Potential Nanocarriers. *J. Phys. Chem. C*. **119**, 24919–24926 (2015).
34. E. Horváth, L. Grebikova, P. Maroni, T. Szabó, A. Magrez, L. Forró, I. Szilágyi, Dispersion Characteristics and Aggregation in Titanate Nanowire Colloids. *ChemPlusChem*, 592–600 (2018).
35. E. Horváth, P. R. Ribič, F. Hashemi, L. Forró, A. Magrez, Dye metachromasy on titanate nanowires: sensing humidity with reversible molecular dimerization. *J. Mater. Chem.* **22**, 8778–8784 (2012).
36. E. Horváth, I. Szilágyi, L. Forró, A. Magrez, Probing titanate nanowire surface acidity through methylene blue adsorption in colloidal suspension and on thin films. *Journal of Colloid and*

Interface Science. **416**, 190–197 (2014).

37. Union des Professeurs de Physique et de Chimie, (available at <https://national.udppc.asso.fr/index.php/component/content/article?id=372:titane-presentation>).
38. M. J. Gázquez, J. P. Bolívar, R. Garcia-Tenorio, F. Vaca, A Review of the Production Cycle of Titanium Dioxide Pigment. *Materials Sciences and Applications*. **5**, 441–458 (2014).
39. B. Jovanović, Critical review of public health regulations of titanium dioxide, a human food additive. *Integrated Environmental Assessment and Management*. **11**, 10–20 (2015).
40. Y. Lan, Y. Lu, Z. Ren, Mini review on photocatalysis of titanium dioxide nanoparticles and their solar applications. *Nano Energy*. **2**, 1031–1045 (2013).
41. Home | Nanotechnology Products Database | NPD, (available at <https://product.statnano.com/>).
42. Titanium Dioxide Products Available in Market | STATNANO, (available at <https://statnano.com//news/48019>).
43. Nanoparticle Titanium Dioxide Market Size, Share, Trends, Forecast, Analysis 2018, (available at <https://www.transparencymarketresearch.com/nanoparticle-titanium-dioxide-tio2-market.html>).
44. C. O. Robichaud, A. E. Uyar, M. R. Darby, L. G. Zucker, M. R. Wiesner, Estimates of Upper Bounds and Trends in Nano-TiO₂ Production As a Basis for Exposure Assessment. *Environ. Sci. Technol.* **43**, 4227–4233 (2009).
45. J. Arbiol, J. Cerdà, G. Dezanneau, A. Cirera, F. Peiró, A. Cornet, J. R. Morante, Effects of Nb doping on the TiO₂ anatase-to-rutile phase transition. *Journal of Applied Physics*. **92**, 853–861 (2002).
46. H. E. Chao, Y. U. Yun, H. U. Xingfang, A. Larbot, Effect of silver doping on the phase transformation and grain growth of sol-gel titania powder. *Journal of the European Ceramic Society*. **23**, 1457–1464 (2003).
47. J. K. Burdett, T. Hughbanks, G. J. Miller, J. W. Richardson, J. V. Smith, Structural-electronic relationships in inorganic solids: powder neutron diffraction studies of the rutile and anatase polymorphs of titanium dioxide at 15 and 295 K. *J. Am. Chem. Soc.* **109**, 3639–3646 (1987).
48. U. Diebold, The surface science of titanium dioxide. *Surface Science Reports*. **48**, 53–229 (2003).
49. H. Tang, F. Lévy, H. Berger, P. E. Schmid, Urbach tail of anatase TiO₂. *Phys. Rev. B*. **52**,

7771–7774 (1995).

50. J. Pascual, J. Camassel, H. Mathieu, Fine structure in the intrinsic absorption edge of TiO₂. *Phys. Rev. B*. **18**, 5606–5614 (1978).

51. A. Amtout, R. Leonelli, Optical properties of rutile near its fundamental band gap. *Phys. Rev. B*. **51**, 6842–6851 (1995).

52. M. V. Dozzi, E. Selli, Specific Facets-Dominated Anatase TiO₂: Fluorine-Mediated Synthesis and Photoactivity. *Catalysts*. **3**, 455–485 (2013).

53. C. Fàbrega, F. Hernández-Ramírez, J. D. Prades, R. Jiménez-Díaz, T. Andreu, J. R. Morante, On the photoconduction properties of low resistivity TiO₂nanotubes. *Nanotechnology*. **21**, 445703 (2010).

54. D. V. Bavykin, F. C. Walsh, Elongated Titanate Nanostructures and Their Applications. *European Journal of Inorganic Chemistry*. **2009**, 977–997 (2009).

55. M. D. Rasmussen, L. M. Molina, B. Hammer, Adsorption, diffusion, and dissociation of molecular oxygen at defected TiO₂(110): A density functional theory study. *J. Chem. Phys.* **120**, 988–997 (2003).

56. M. Tournoux, R. Marchand, L. Brohan, Layered K₂Ti₄O₉ and the open metastable TiO₂(B) structure. *Progress in Solid State Chemistry*. **17**, 33–52 (1986).

57. M. Qamar, C. R. Yoon, H. J. Oh, D. H. Kim, J. H. Jho, K. S. Lee, W. J. Lee, H. G. Lee, S. J. Kim, Effect of post treatments on the structure and thermal stability of titanate nanotubes. *Nanotechnology*. **17**, 5922–5929 (2006).

58. O. Yu. Gorbenko, S. V. Samoilenov, I. E. Graboy, A. R. Kaul, Epitaxial Stabilization of Oxides in Thin Films. *Chem. Mater.* **14**, 4026–4043 (2002).

59. B. A. Apgar, L. W. Martin, Understanding the Competition between Epitaxial Strain and Thermodynamics in TiO₂: Structural, Morphological, and Property Evolution. *Crystal Growth & Design*. **14**, 1981–1988 (2014).

60. J.-N. Nian, H. Teng, Hydrothermal Synthesis of Single-Crystalline Anatase TiO₂ Nanorods with Nanotubes as the Precursor. *J. Phys. Chem. B*. **110**, 4193–4198 (2006).

61. Y. Mao, S. S. Wong, Size- and Shape-Dependent Transformation of Nanosized Titanate into Analogous Anatase Titania Nanostructures. *J. Am. Chem. Soc.* **128**, 8217–8226 (2006).

62. P. Wen, Y. Ishikawa, H. Itoh, Q. Feng, Topotactic Transformation Reaction from Layered Titanate Nanosheets into Anatase Nanocrystals. *J. Phys. Chem. C*. **113**, 20275–20280 (2009).

-
63. R. L. Penn, J. F. Banfield, Formation of rutile nuclei at anatase (112) twin interfaces and the phase transformation mechanism in nanocrystalline titania. *American Mineralogist*. **84**, 871–876 (1999).
64. H. Zhang, J. F. Banfield, Phase transformation of nanocrystalline anatase-to-rutile via combined interface and surface nucleation. *Journal of Materials Research*. **15**, 437–448 (2000).
65. W. Li, C. Ni, H. Lin, C. P. Huang, S. I. Shah, Size dependence of thermal stability of TiO₂ nanoparticles. *Journal of Applied Physics*. **96**, 6663–6668 (2004).
66. J. Li, Y. Ye, L. Shen, J. Chen, H. Zhou, Densification and grain growth during pressureless sintering of TiO₂ nanoceramics. *Materials Science and Engineering: A*. **390**, 265–270 (2005).
67. Y. Zhou, K. A. Fichthorn, Microscopic View of Nucleation in the Anatase-to-Rutile Transformation. *J. Phys. Chem. C*. **116**, 8314–8321 (2012).
68. H. Zhang, J. F. Banfield, New kinetic model for the nanocrystalline anatase-to-rutile transformation revealing rate dependence on number of particles. *American Mineralogist*. **84**, 528–535 (2015).
69. A. A. Gribb, J. F. Banfield, Particle size effects on transformation kinetics and phase stability in nanocrystalline TiO₂. *American Mineralogist*. **82**, 717–728 (2015).
70. P. Galizia, G. Maizza, C. Galassi, Heating rate dependence of anatase to rutile transformation. *Processing and Application of Ceramics*. **10**, 235–241 (2016).
71. R. A. Howie, J.W. Anthony, R.A. Bideaux, K.W. Bladh and M.C. Nicols Handbook of Mineralogy. Volume III: Halides, Hydroxides, Oxides. Tucson (Mineral Data Publishing), 1997. x + 628 pp. Price £67.50 (+ £3.40 postage; available in the UK via Endsleigh Book Co., Norwich NR16 1LH). ISBN 0-9622097-0-8. *Mineralogical Magazine*. **62**, 432–432 (1998).
72. P. Hernández-Hipólito, M. García-Castillejos, E. Martínez-Klimova, N. Juárez-Flores, A. Gómez-Cortés, T. E. Klimova, Biodiesel production with nanotubular sodium titanate as a catalyst. *Catalysis Today*. **220–222**, 4–11 (2014).
73. E. Horváth, L. Forró, A. Magrez, Titanium oxide aerogel composites (2016), (available at <https://patents.google.com/patent/EP2964577A1/en>).
74. Y. Xiao, J. Wu, G. Yue, G. Xie, J. Lin, M. Huang, The preparation of titania nanotubes and its application in flexible dye-sensitized solar cells. *Electrochimica Acta*. **55**, 4573–4578 (2010).
75. D. Zhang, J. A. Downing, F. J. Knorr, J. L. McHale, Room-Temperature Preparation of Nanocrystalline TiO₂ Films and the Influence of Surface Properties on Dye-Sensitized Solar Energy

Conversion. *J. Phys. Chem. B.* **110**, 21890–21898 (2006).

76. X. Li, H. Lin, J. Li, N. Wang, C. Lin, L. Zhang, Chemical sintering of graded TiO₂ film at low-temperature for flexible dye-sensitized solar cells. *Journal of Photochemistry and Photobiology A: Chemistry.* **195**, 247–253 (2008).

77. J. Zhi, C. Yang, T. Lin, H. Cui, Z. Wang, H. Zhang, F. Huang, Flexible all solid state supercapacitor with high energy density employing black titania nanoparticles as a conductive agent. *Nanoscale.* **8**, 4054–4062 (2016).

78. Y. Dkhissi, F. Huang, S. Rubanov, M. Xiao, U. Bach, L. Spiccia, R. A. Caruso, Y.-B. Cheng, Low temperature processing of flexible planar perovskite solar cells with efficiency over 10%. *Journal of Power Sources.* **278**, 325–331 (2015).

79. D. Liu, T. L. Kelly, Perovskite solar cells with a planar heterojunction structure prepared using room-temperature solution processing techniques. *Nature Photonics.* **8**, 133–138 (2014).

80. N.-S. Jang, M. S. Kim, S.-H. Kim, S.-K. Lee, J.-M. Kim, Direct growth of titania nanotubes on plastic substrates and their application to flexible gas sensors. *Sensors and Actuators B: Chemical.* **199**, 361–368 (2014).

81. M. M. J. Treacy, T. W. Ebbesen, J. M. Gibson, Exceptionally high Young's modulus observed for individual carbon nanotubes. *Nature.* **381**, 678–680 (1996).

82. P. Poncharal, Z. L. Wang, D. Ugarte, W. A. de Heer, Electrostatic Deflections and Electro-mechanical Resonances of Carbon Nanotubes. *Science.* **283**, 1513–1516 (1999).

83. E. W. Wong, P. E. Sheehan, C. M. Lieber, Nanobeam Mechanics: Elasticity, Strength, and Toughness of Nanorods and Nanotubes. *Science.* **277**, 1971–1975 (1997).

84. J.-P. Salvetat, J.-M. Bonard, N. H. Thomson, A. J. Kulik, L. Forró, W. Benoit, L. Zuppiroli, Mechanical properties of carbon nanotubes. *Appl Phys A.* **69**, 255–260 (1999).

85. J.-P. Salvetat, A. J. Kulik, J.-M. Bonard, G. A. D. Briggs, T. Stöckli, K. Méténier, S. Bonnamy, F. Béguin, N. A. Burnham, L. Forró, Elastic Modulus of Ordered and Disordered Multiwalled Carbon Nanotubes. *Advanced Materials.* **11**, 161–165 (1999).

86. J.-P. Salvetat, G. A. D. Briggs, J.-M. Bonard, R. R. Bacsa, A. J. Kulik, T. Stöckli, N. A. Burnham, L. Forró, Elastic and Shear Moduli of Single-Walled Carbon Nanotube Ropes. *Phys. Rev. Lett.* **82**, 944–947 (1999).

87. J. M. Gere, S. P. Timoshenko, *Mechanics of Materials* (PWS Publishing Company, Boston, MA, 1990).

-
88. A. Kis, G. Csányi, J.-P. Salvetat, T.-N. Lee, E. Couteau, A. J. Kulik, W. Benoit, J. Brugger, L. Forró, Reinforcement of single-walled carbon nanotube bundles by intertube bridging. *Nature Materials*. **3**, 153–157 (2004).
89. A. Heidelberg, L. T. Ngo, B. Wu, M. A. Phillips, S. Sharma, T. I. Kamins, J. E. Sader, J. J. Boland, A Generalized Description of the Elastic Properties of Nanowires. *Nano Lett.* **6**, 1101–1106 (2006).
90. B. Wu, A. Heidelberg, J. J. Boland, Mechanical properties of ultrahigh-strength gold nanowires. *Nature Mater.* **4**, 525–529 (2005).
91. C. Q. Chen, Y. Shi, Y. S. Zhang, J. Zhu, Y. J. Yan, Size Dependence of Young's Modulus in ZnO Nanowires. *Phys. Rev. Lett.* **96**, 075505 (2006).
92. B. Wen, J. E. Sader, J. J. Boland, Mechanical Properties of ZnO Nanowires. *Phys. Rev. Lett.* **101**, 175502 (2008).
93. Y. Chen, B. L. Dorgan, D. N. McIlroy, D. Eric Aston, On the importance of boundary conditions on nanomechanical bending behavior and elastic modulus determination of silver nanowires. *Journal of Applied Physics*. **100**, 104301 (2006).
94. M. T. McDowell, A. M. Leach, K. Gall, Bending and tensile deformation of metallic nanowires. *Modelling Simul. Mater. Sci. Eng.* **16**, 045003 (2008).
95. S. Cuenot, C. Frétiigny, S. Demoustier-Champagne, B. Nysten, Surface tension effect on the mechanical properties of nanomaterials measured by atomic force microscopy. *Phys. Rev. B*. **69**, 165410 (2004).
96. I. Kaplan-Ashiri, R. Tenne, Mechanical Properties of WS₂ Nanotubes. *J Clust Sci.* **18**, 549–563 (2007).
97. F. C. Cheong, B. Varghese, Y. Zhu, E. P. S. Tan, L. Dai, V. B. C. Tan, C. T. Lim, C. H. Sow, WO₃-x Nanorods Synthesized on a Thermal Hot Plate. *J. Phys. Chem. C*. **111**, 17193–17199 (2007).
98. H. Zhang, J. Tang, L. Zhang, B. An, L.-C. Qin, Atomic force microscopy measurement of the Young's modulus and hardness of single LaB₆ nanowires. *Appl. Phys. Lett.* **92**, 173121 (2008).
99. G. Stan, S. Krylyuk, A. V. Davydov, M. Vaudin, L. A. Bendersky, R. F. Cook, Surface effects on the elastic modulus of Te nanowires. *Appl. Phys. Lett.* **92**, 241908 (2008).
100. H.-J. Butt, B. Cappella, M. Kappl, Force measurements with the atomic force microscope: Technique, interpretation and applications. *Surface Science Reports*. **59**, 1–152 (2005).
101. A. Bo, H. Zhan, J. Bell, H. Zhu, Y. Gu, Mechanical bending properties of sodium titanate

- (Na₂Ti₃O₇) nanowires. *RSC Adv.* **4**, 56970–56976 (2014).
102. A. Bo, K. Chen, E. Pickering, H. Zhan, J. Bell, A. Du, Y. Zhang, X. Wang, H. Zhu, Z. Shan, Y. Gu, Atypical Defect Motions in Brittle Layered Sodium Titanate Nanowires. *J. Phys. Chem. Lett.* **9**, 6052–6059 (2018).
103. M. Humar, D. Arčon, P. Umek, M. Škarabot, I. Muševič, G. Bregar, Mechanical properties of titania-derived nanoribbons. *Nanotechnology.* **17**, 3869–3872 (2006).
104. L. Ciric, “Unpublished.”
105. G. Cheng, C. Miao, Q. Qin, J. Li, F. Xu, H. Haftbaradaran, E. C. Dickey, H. Gao, Y. Zhu, Large anelasticity and associated energy dissipation in single-crystalline nanowires. *Nature Nanotechnology.* **10**, 687–691 (2015).
106. L. Dai, C. H. Sow, C. T. Lim, W. C. D. Cheong, V. B. C. Tan, Numerical Investigations into the Tensile Behavior of TiO₂ Nanowires: Structural Deformation, Mechanical Properties, and Size Effects. *Nano Lett.* **9**, 576–582 (2009).
107. J. Yu, Q. Xiang, M. Zhou, Preparation, characterization and visible-light-driven photocatalytic activity of Fe-doped titania nanorods and first-principles study for electronic structures. *Applied Catalysis B: Environmental.* **90**, 595–602 (2009).
108. R. Doong, S. Chang, C. Tsai, Enhanced photoactivity of Cu-deposited titanate nanotubes for removal of bisphenol A. *Applied Catalysis B: Environmental.* **129**, 48–55 (2013).
109. X. Zhao, Z. Cai, T. Wang, S. E. O'Reilly, W. Liu, D. Zhao, A new type of cobalt-deposited titanate nanotubes for enhanced photocatalytic degradation of phenanthrene. *Applied Catalysis B: Environmental.* **187**, 134–143 (2016).
110. A. Taketoshi, M. Haruta, Size- and Structure-specificity in Catalysis by Gold Clusters. *Chem. Lett.* **43**, 380–387 (2014).
111. N. Mizuno, M. Misono, Heterogeneous Catalysis. *Chem. Rev.* **98**, 199–218 (1998).
112. B. C. Gates, Supported Metal Clusters: Synthesis, Structure, and Catalysis. *Chem. Rev.* **95**, 511–522 (1995).
113. A. T. Bell, The Impact of Nanoscience on Heterogeneous Catalysis. *Science.* **299**, 1688–1691 (2003).
114. Y. Xia, H. Yang, C. T. Campbell, Nanoparticles for Catalysis. *Acc. Chem. Res.* **46**, 1671–1672 (2013).
115. A. Corma, H. Garcia, Supported gold nanoparticles as catalysts for organic reactions. *Chem.*

Soc. Rev. **37**, 2096–2126 (2008).

116. D. I. Enache, J. K. Edwards, P. Landon, B. Solsona-Espriu, A. F. Carley, A. A. Herzing, M. Watanabe, C. J. Kiely, D. W. Knight, G. J. Hutchings, Solvent-Free Oxidation of Primary Alcohols to Aldehydes Using Au-Pd/TiO₂ Catalysts. *Science*. **311**, 362–365 (2006).

117. J. M. Thomas, B. F. G. Johnson, R. Raja, G. Sankar, P. A. Midgley, High-Performance Nanocatalysts for Single-Step Hydrogenations. *Acc. Chem. Res.* **36**, 20–30 (2003).

118. C. Song, An overview of new approaches to deep desulfurization for ultra-clean gasoline, diesel fuel and jet fuel. *Catalysis Today*. **86**, 211–263 (2003).

119. M. Yang, S. Li, Y. Wang, J. A. Herron, Y. Xu, L. F. Allard, S. Lee, J. Huang, M. Mavrikakis, M. Flytzani-Stephanopoulos, Catalytically active Au-O(OH)_x- species stabilized by alkali ions on zeolites and mesoporous oxides. *Science*. **346**, 1498–1501 (2014).

120. Q. Fu, H. Saltsburg, M. Flytzani-Stephanopoulos, Active Nonmetallic Au and Pt Species on Ceria-Based Water-Gas Shift Catalysts. *Science*. **301**, 935–938 (2003).

121. J. Xu, G. F. Froment, Methane steam reforming, methanation and water-gas shift: I. Intrinsic kinetics. *AIChE Journal*. **35**, 88–96 (1989).

122. Y. Nosaka, A. Y. Nosaka, Generation and Detection of Reactive Oxygen Species in Photocatalysis. *Chem. Rev.* **117**, 11302–11336 (2017).

123. L. Liu, X. Chen, Titanium Dioxide Nanomaterials: Self-Structural Modifications. *Chem. Rev.* **114**, 9890–9918 (2014).

124. D. Delimaris, T. Ioannides, VOC oxidation over MnO_x–CeO₂ catalysts prepared by a combustion method. *Applied Catalysis B: Environmental*. **84**, 303–312 (2008).

125. L. F. Liotta, Catalytic oxidation of volatile organic compounds on supported noble metals. *Applied Catalysis B: Environmental*. **100**, 403–412 (2010).

126. M. Haruta, Size- and support-dependency in the catalysis of gold. *Catalysis Today*. **1**, 153–166 (1997).

127. M. S. Chen, D. W. Goodman, The Structure of Catalytically Active Gold on Titania. *Science*. **306**, 252–255 (2004).

128. C. T. Campbell, The Energetics of Supported Metal Nanoparticles: Relationships to Sintering Rates and Catalytic Activity. *Acc. Chem. Res.* **46**, 1712–1719 (2013).

129. T. W. Hansen, A. T. DeLaRiva, S. R. Challa, A. K. Datye, Sintering of Catalytic Nanoparticles: Particle Migration or Ostwald Ripening? *Acc. Chem. Res.* **46**, 1720–1730 (2013).

-
130. C. H. Bartholomew, Mechanisms of catalyst deactivation. *Applied Catalysis A: General*. **212**, 17–60 (2001).
131. C. T. Campbell, Electronic perturbations. *Nature Chemistry*. **4**, 597–598 (2012).
132. M. Haruta, T. Kobayashi, H. Sano, N. Yamada, Novel Gold Catalysts for the Oxidation of Carbon Monoxide at a Temperature far Below 0 °C. *Chem. Lett.* **16**, 405–408 (1987).
133. G. J. Hutchings, Vapor phase hydrochlorination of acetylene: Correlation of catalytic activity of supported metal chloride catalysts. *Journal of Catalysis*. **96**, 292–295 (1985).
134. T. Takei, T. Akita, I. Nakamura, T. Fujitani, M. Okumura, K. Okazaki, J. Huang, T. Ishida, M. Haruta, in *Advances in Catalysis*, B. C. Gates, F. C. Jentoft, Eds. (Academic Press, 2012; <http://www.sciencedirect.com/science/article/pii/B9780123855169000016>), vol. 55, pp. 1–126.
135. G. C. Bond, D. T. Thompson, Catalysis by Gold. *Catalysis Reviews*. **41**, 319–388 (1999).
136. A. Abad, P. Concepción, A. Corma, H. García, A Collaborative Effect between Gold and a Support Induces the Selective Oxidation of Alcohols. *Angewandte Chemie International Edition*. **44**, 4066–4069 (2005).
137. G. Li, R. Jin, Catalysis by gold nanoparticles: carbon-carbon coupling reactions. *Nanotechnology Reviews*. **2**, 529–545 (2013).
138. R. Kubo, Electronic Properties of Metallic Fine Particles. I. *J. Phys. Soc. Jpn.* **17**, 975–986 (1962).
139. X. Y. Liu, A. Wang, T. Zhang, C.-Y. Mou, Catalysis by gold: New insights into the support effect. *Nano Today*. **8**, 403–416 (2013).
140. M. Haruta, Catalysis of Gold Nanoparticles Deposited on Metal Oxides. *CATTECH*. **6**, 102–115 (2002).
141. X. Zhang, H. Shi, B.-Q. Xu, Vital roles of hydroxyl groups and gold oxidation states in Au/ZrO₂ catalysts for 1,3-butadiene hydrogenation. *Journal of Catalysis*. **279**, 75–87 (2011).
142. R. T. K. Baker, The relationship between particle motion on a graphite surface and Tamman temperature. *Journal of Catalysis*. **78**, 473–476 (1982).
143. G. Tammann, Zum Gedächtnis der Entdeckung des Isomorphismus vor 100 Jahren. Die chemischen und galvanischen Eigenschaften von Mischkristallreihen und ihre Atomverteilung. *Zeitschrift für anorganische und allgemeine Chemie*. **107**, 1–239 (1919).
144. G. Prieto, H. Tüysüz, N. Duyckaerts, J. Knossalla, G.-H. Wang, F. Schüth, Hollow Nano- and Microstructures as Catalysts. *Chem. Rev.* **116**, 14056–14119 (2016).

-
145. Ph. Buffat, J.-P. Borel, Size effect on the melting temperature of gold particles. *Phys. Rev. A*. **13**, 2287–2298 (1976).
146. K. K. Nanda, Size-dependent melting of nanoparticles: Hundred years of thermodynamic model. *Pramana - J Phys.* **72**, 617–628 (2009).
147. P. Schlexer, A. B. Andersen, B. Sebok, I. Chorkendorff, J. Schiøtz, T. W. Hansen, Size-Dependence of the Melting Temperature of Individual Au Nanoparticles. *Particle & Particle Systems Characterization*. **36**, 1800480 (2019).
148. A. Safaei, M. A. Shandiz, S. Sanjabi, Z. H. Barber, Modelling the size effect on the melting temperature of nanoparticles, nanowires and nanofilms. *J. Phys.: Condens. Matter*. **19**, 216216 (2007).
149. S. C. Parker, C. T. Campbell, Kinetic model for sintering of supported metal particles with improved size-dependent energetics and applications to Au on TiO₂ (110). *Phys. Rev. B*. **75**, 035430 (2007).
150. C. T. Campbell, S. C. Parker, D. E. Starr, The Effect of Size-Dependent Nanoparticle Energetics on Catalyst Sintering. *Science*. **298**, 811–814 (2002).
151. E. D. Goodman, J. A. Schwalbe, M. Cargnello, Mechanistic Understanding and the Rational Design of Sinter-Resistant Heterogeneous Catalysts. *ACS Catal.* **7**, 7156–7173 (2017).
152. R. A. Bennett, M. A. Newton, R. D. Smith, J. Evans, M. Bowker, Titania surface structures for directed growth of metal nanoparticles via metal vapour deposition and metal organic chemical vapour deposition. *Materials Science and Technology*. **18**, 710–716 (2002).
153. F. Yang, M. S. Chen, D. W. Goodman, Sintering of Au Particles Supported on TiO₂(110) during CO Oxidation. *J. Phys. Chem. C*. **113**, 254–260 (2009).
154. Y. Dai, P. Lu, Z. Cao, C. T. Campbell, Y. Xia, The physical chemistry and materials science behind sinter-resistant catalysts. *Chemical Society Reviews*. **47**, 4314–4331 (2018).
155. W. Yuan, D. Zhang, Y. Ou, K. Fang, B. Zhu, H. Yang, T. W. Hansen, J. B. Wagner, Z. Zhang, Y. Gao, Y. Wang, Direct In Situ TEM Visualization and Insight into the Facet-Dependent Sintering Behaviors of Gold on TiO₂. *Angewandte Chemie International Edition*. **57**, 16827–16831 (2018).
156. K.-J. Hu, S. R. Plant, P. R. Ellis, C. M. Brown, P. T. Bishop, R. E. Palmer, Atomic Resolution Observation of a Size-Dependent Change in the Ripening Modes of Mass-Selected Au Nanoclusters Involved in CO Oxidation. *J. Am. Chem. Soc.* **137**, 15161–15168 (2015).
157. S. L. Hemmingson, C. T. Campbell, Trends in Adhesion Energies of Metal Nanoparticles on

- Oxide Surfaces: Understanding Support Effects in Catalysis and Nanotechnology. *ACS Nano*. **11**, 1196–1203 (2017).
158. C. T. Campbell, Z. Mao, Chemical Potential of Metal Atoms in Supported Nanoparticles: Dependence upon Particle Size and Support. *ACS Catal.* **7**, 8460–8466 (2017).
159. W. Ostwald, Über die vermeintliche Isomerie des roten und gelben Quecksilberoxyds und die Oberflächenspannung fester Körper. *Zeitschrift für Physikalische Chemie*. **34U**, 495–503 (1900).
160. S. R. Challa, A. T. Delariva, T. W. Hansen, S. Helveg, J. Sehested, P. L. Hansen, F. Garzon, A. K. Datye, Relating Rates of Catalyst Sintering to the Disappearance of Individual Nanoparticles during Ostwald Ripening. *J. Am. Chem. Soc.* **133**, 20672–20675 (2011).
161. A. T. DeLaRiva, T. W. Hansen, S. R. Challa, A. K. Datye, In situ Transmission Electron Microscopy of catalyst sintering. *Journal of Catalysis*. **308**, 291–305 (2013).
162. M. T. Bore, H. N. Pham, E. E. Switzer, T. L. Ward, A. Fukuoka, A. K. Datye, The Role of Pore Size and Structure on the Thermal Stability of Gold Nanoparticles within Mesoporous Silica. *J. Phys. Chem. B*. **109**, 2873–2880 (2005).
163. S. Zhang, C. Chen, M. Cargnello, P. Fornasiero, R. J. Gorte, G. W. Graham, X. Pan, Dynamic structural evolution of supported palladium–ceria core–shell catalysts revealed by in situ electron microscopy. *Nature Communications*. **6**, 1–6 (2015).
164. A. D. Benavidez, L. Kovarik, A. Genc, N. Agrawal, E. M. Larsson, T. W. Hansen, A. M. Karim, A. K. Datye, Environmental Transmission Electron Microscopy Study of the Origins of Anomalous Particle Size Distributions in Supported Metal Catalysts. *ACS Catal.* **2**, 2349–2356 (2012).
165. G. Prieto, J. Zečević, H. Friedrich, K. P. de Jong, P. E. de Jongh, Towards stable catalysts by controlling collective properties of supported metal nanoparticles. *Nature Materials*. **12**, 34–39 (2013).
166. C. G. Granqvist, R. A. Buhrman, Statistical model for coalescence of islands in discontinuous films. *Appl. Phys. Lett.* **27**, 693–694 (1975).
167. S. Li, J. Gong, Strategies for improving the performance and stability of Ni-based catalysts for reforming reactions. *Chemical Society Reviews*. **43**, 7245–7256 (2014).
168. L. Wang, L. Wang, X. Meng, F.-S. Xiao, New Strategies for the Preparation of Sinter-Resistant Metal-Nanoparticle-Based Catalysts. *Advanced Materials*. **31**, 1901905 (2019).
169. S. J. Tauster, S. C. Fung, R. L. Garten, Strong metal-support interactions. Group 8 noble metals supported on titanium dioxide. *J. Am. Chem. Soc.* **100**, 170–175 (1978).

-
170. S. J. Tauster, Strong metal-support interactions. *Acc. Chem. Res.* **20**, 389–394 (1987).
171. S. A. C. Carabineiro, Supported Gold Nanoparticles as Catalysts for the Oxidation of Alcohols and Alkanes. *Front Chem.* **7** (2019), doi:10.3389/fchem.2019.00702.
172. Y. Chen, P. Su, X. Liu, H. Liu, B. Zhu, S. Zhang, W. Huang, Titanate Nanotube-Supported Au–Rh Bimetallic Catalysts: Characterization and Their Catalytic Performances in Hydroformylation of Vinyl Acetate. *Catalysts*. **8**, 420 (2018).
173. T. M. F. Marques, R. N. Morais, F. X. Nobre, J. M. Rocha, A. Ghosh, T. A. S. Soares, B. C. Viana, G. Machado, J. C. S. Costa, J. M. E. D. Matos, T. M. F. Marques, R. N. Morais, F. X. Nobre, J. M. Rocha, A. Ghosh, T. A. S. Soares, B. C. Viana, G. Machado, J. C. S. Costa, J. M. E. D. Matos, Hydrogen production from aqueous glycerol using titanate nanotubes decorated with Au nanoparticles as photocatalysts. *Anais da Academia Brasileira de Ciências*. **91** (2019), doi:10.1590/0001-3765201920190082.
174. A. Loiseau, J. Boudon, A. Oudot, M. Moreau, R. Boidot, R. Chassagnon, N. Mohamed Saïd, S. Roux, C. Mirjolet, N. Millot, Titanate Nanotubes Engineered with Gold Nanoparticles and Docetaxel to Enhance Radiotherapy on Xenografted Prostate Tumors. *Cancers*. **11**, 1962 (2019).
175. A. Naldoni, M. Altomare, G. Zoppellaro, N. Liu, Š. Kment, R. Zbořil, P. Schmuki, Photocatalysis with Reduced TiO₂: From Black TiO₂ to Cocatalyst-Free Hydrogen Production. *ACS Catal.* **9**, 345–364 (2019).
176. X. Han, Y. Liu, Y. Yin, Colorimetric Stress Memory Sensor Based on Disassembly of Gold Nanoparticle Chains. *Nano Lett.* **14**, 2466–2470 (2014).
177. L. Zhou, Y. Tan, D. Ji, B. Zhu, P. Zhang, J. Xu, Q. Gan, Z. Yu, J. Zhu, Self-assembly of highly efficient, broadband plasmonic absorbers for solar steam generation. *Science Advances*. **2**, e1501227 (2016).
178. A. Houas, H. Lachheb, M. Ksibi, E. Elaloui, C. Guillard, J.-M. Herrmann, Photocatalytic degradation pathway of methylene blue in water. *Applied Catalysis B: Environmental*. **31**, 145–157 (2001).
179. M. Cantarella, G. Impellizzeri, V. Privitera, Functional nanomaterials for water purification. *La Rivista del Nuovo Cimento*. **40**, 595–632 (2017).
180. Chang. Wei, W. Yuan. Lin, Zulkarnain. Zainal, N. E. Williams, Kai. Zhu, A. P. Kruzic, R. L. Smith, Krishnan. Rajeshwar, Bactericidal Activity of TiO₂ Photocatalyst in Aqueous Media: Toward a Solar-Assisted Water Disinfection System. *Environ. Sci. Technol.* **28**, 934–938 (1994).

181. M. Zimbone, M. A. Buccheri, G. Cacciato, R. Sanz, G. Rappazzo, S. Boninelli, R. Reitano, L. Romano, V. Privitera, M. G. Grimaldi, Photocatalytic and antibacterial activity of TiO₂ nanoparticles obtained by laser ablation in water. *Applied Catalysis B: Environmental*. **165**, 487–494 (2015).
182. J. A. Ibáñez, M. I. Litter, R. A. Pizarro, Photocatalytic bactericidal effect of TiO₂ on Enterobacter cloacae: Comparative study with other Gram (–) bacteria. *Journal of Photochemistry and Photobiology A: Chemistry*. **157**, 81–85 (2003).
183. M. Cho, H. Chung, W. Choi, J. Yoon, Linear correlation between inactivation of E. coli and OH radical concentration in TiO₂ photocatalytic disinfection. *Water Research*. **38**, 1069–1077 (2004).
184. M. Cho, H. Chung, W. Choi, J. Yoon, Different Inactivation Behaviors of MS-2 Phage and Escherichia coli in TiO₂ Photocatalytic Disinfection. *Appl. Environ. Microbiol.* **71**, 270–275 (2005).
185. E. Team, Agarose gel electrophoresis of DNA - Principle, Protocol and Uses. *LaboratoryInfo.com* (2020), (available at <https://laboratoryinfo.com/agarose-gel-electrophoresis/>).
186. E. Horváth, L. Rossi, C. Mercier, A. Sienkiewicz, L. Forró, Photocatalytic nanowires-based air filter: towards reusable protective masks. *Advanced Functional Materials* (2020).

LIDIA ROSSI ROCOFFORT DE VINNIÈRE

Avenue William-Fraisse, 8
CH-1006 Lausanne
+41 79 540 26 87
lidiaa.rossi@gmail.com

14.10.1990
Married
Italian
Swiss Permit B



EDUCATION

- 2016-2020 **PhD in Physics** at the Laboratory of Physics of Complex Matter (Prof. L Forró)
Swiss Federal Institute of Technology (EPFL), Lausanne, CH
- 2012-2014 **MSc in Physics**
Pierre and Marie Curie University, Sorbonne Universités, Paris VI, FR
Co-ability with ENS Paris, Ecole Polytechnique, ESPCI
5-months exchange at National High Magnetic Field Laboratory, USA
- 2008-2012 **BSc in Physics**
University of Milan, IT
3-months exchange at Fermi National Laboratory, USA
- 2005-2008 **Scientific High School**, French Baccalaureat
Lycée International de Ferney-Voltaire, FR

WORK EXPERIENCES

- 2016-present **Doctoral assistant**, EPFL, Lausanne, CH
(4 years) Thesis work on *TiO₂ based-ceramics, from basic science to applications*
- Collaboration with a swatch luxury industry for development of a new nano-material composite and its characterizations (2 years).
- Microscopical and mechanical characterization of single TiO₂ nanowires and their assemblies.
- Responsible for negotiation with companies for purchase of laboratory equipments.
- Public speaking and presentation experience in international conferences.
- 2014-2016 **Scientific collaborator**, University of Geneva, CH
(1.5 years) - Manager of a new system: pulsed laser deposition (PLD) for thin films fabrication.
- 2014 **Master thesis**, National High Magnetic Field Laboratory/Applied Superconductivity Center, Florida State University, Tallahassee, Florida, USA

- (5 months) - Design and testing system for critical current characterization of REBCO conductors for high field magnet use.
- 2013 **Summer internship**, University of Geneva, CH
(3 months) - Study of thermo-physics properties for superconductors applications.
- 2012 **Bachelor internship**, Fermi National Laboratory, Batavia, Illinois, USA
(3 months) - Study of superconducting-to-resistive transition for the US-LARP large high field quadrupoles for the LHC upgrade (CERN).
- MathCad code implementation.

SKILLS

- Material synthesis** Pulsed Laser Deposition (PLD), thermal evaporation, sputtering, sintering processes (Spark Plasma Sintering SPS, hot uniaxial pressing).
- Materials characterisation** Scanning electron microscopy (SEM), transmission electron microscopy (TEM), energy-dispersive X-ray spectroscopy (EDX), atomic force microscopy (AFM), X-ray fluorescence (XRF), X-ray diffraction (XRD), Raman spectroscopy, nanoindentation, Vickers microhardness, three-point bending test, thermal gravimetric analysis (TGA), resistivity measurements.
- Cleanroom processes** Layout preparation, photolithography, dry and wet etching
- Computer skills** Wolfram Mathematica, C/C++

MS Office, Origin, Gwyddion, ImageJ, Adobe Illustrator and InDesign

Electron microscopy-associated softwares such as Tia, Velox, Aztec

LANGUAGES

- Italian Mother language
- French Mother language
- English Fluent (C1)

INTERESTS

- Fashion design and modeling (IPAC Design School)
- Music: piano (conservatory)
- Swimming, tennis, hiking across the Swiss Alps
- Girl scout leader in Geneva

PUBLICATIONS

Journal articles

- E. Horváth, **L. Rossi**, C. Mercier, C. Lehmann, A. Sienkiewicz, L. Forró, *Photocatalytic nanowires-based air filter: towards reusable protective masks*, Advanced Functional Materials (2020).
- **L. Rossi**, R. Foschia, A. Glushkova, L. Forró, E. Horváth, *Mechanical response of layered titanate nanowires*, Ceramics International **46**, 17729-17734 (2020).
- **L. Rossi**, X. Berdat, M. Spina, S. Brown, L. Bernard, S. Katrych, L. Forró, E. Horváth, *Thermal coarsening of individual titanate nanowires and their assemblies: Surface vs. bulk diffusion*, Ceramics International **46**, 16321-16327 (2020).
- K. Mantulnikovs, P. Szirmai, M. Kollár, J. Stevens, P. Andričević, A. Glushkova, **L. Rossi**, P. Bugnon, E. Horváth, A. Sienkiewicz, L. Forró, B. Náfrádi, *Light-induced charge transfer at the $\text{CH}_3\text{NH}_3\text{PbI}_3/\text{TiO}_2$ interface - a low-temperature Photo-EPR assay*, Journal of Physics: Photonics **2**, 014007 (2020).
- P. Andričević, X. Mettan, M. Kollár, B. Náfrádi, A. Sienkiewicz, T. Garma, **L. Rossi**, L. Forró, E. Horváth, *Light-Emitting Electrochemical Cells of Single Crystal Hybrid Halide Perovskite with Vertically Aligned Carbon Nanotubes Contacts*, ACS Photonics **6**, 4, 967-975 (2019).
- E. Martino, M. D. Bachmann, **L. Rossi**, K. A. Modic, I. Zivkovic, H. M. Rønnow, P. J. W. Moll, A. Akrap, L. Forró and S. Katrych, *Persistent antiferromagnetic order in heavily overdoped $\text{Ca}_{1-x}\text{La}_x\text{FeAs}_2$* , Journal of Physics: Condensed Matter **31**, 485705 (2019).
- X. Mettan, J. Jaćimović, O. S. Barišić, A. Pisoni, I. Batistić, E. Horváth, S. Brown, **L. Rossi**, P. Szirmai, B. Farkas, H. Berger & L. Forró, *Tailoring thermal conduction in anatase TiO_2* , Communication Physics **2**, 123 (2019).
- X. Hu, **L. Rossi**, A. Stangl, J. W. Sinclair, F. Kametani, D. Abaimov, A. Polyanskii, J. Y. Coulter, J. Jaroszynski, D. C. Larbalestier, *An Experimental and Analytical Study of Periodic and Aperiodic Fluctuations in the Critical Current of Long Coated Conductors*, IEEE Transactions on Applied Superconductivity **27**, 4 (2017).
- A. Fête, **L. Rossi**, A. Augieri, C. Senatore, *Ionic liquid gating of ultra-thin $\text{YBa}_2\text{Cu}_3\text{O}_{7-x}$ films*, Applied Physics Letter **109**, 192601 (2016).

- **L. Rossi**, X. Hu, F. Kametani, D. Abraimov, A. Polyanskii, J. Jaroszynski and D. C. Larbalestier, *Sample and length-dependent variability of 77 and 4.2 K properties in nominally identical RE123 coated conductors*, Supercond. Sci. Technol. **29**, 054006 (2016).

Pending papers

- E. Horváth, M. Kollár, P. Andričević, **L. Rossi**, X. Mettan, L. Forró, *Fighting health hazards in lead halide perovskite solar cell with transparent phosphate salts*, submitted to Energy and Environmental Science.
- L. Cirić, **L. Rossi**, V. Naussbaumer, L. Forró, E. Horváth *Superelastic behavior of $\text{CH}_3\text{NH}_3\text{PbI}_3$ nanowires*, in preparation.

ORAL PRESENTATIONS

ECerS 2019, 16th Conference & Exhibition of the European Ceramic Society, Torino, Italy, June 16-20, 2019.

AMBER-EPFL joint workshop on novel electronic and nanoscale materials, Trinity College, Dublin, Ireland, April 26, 2018.

12th Conference for Young Scientists in Ceramics - CYSC 2017, Novi Sad, Serbia, October 18-21, 2017.

ECerS 2017, 15th Conference & Exhibition of the European Ceramic Society, Budapest, Hungary, July 9-13, 2017.

